2014

Simulation of crystal, electronic and magnetic structures, and gas adsorption of two dimensional materials

Liya Feng
University of Wollongong

Institute for Superconducting and Electronic Materials

Simulation of crystal, electronic and magnetic structures, and gas adsorption of two dimensional materials

Liya Feng

"This thesis is presented as part of the requirements for the award of the Degree of the University of Wollongong"

March, 2014

ABSTRACT

In this thesis, functionalization of monolayer honeycomb lattices and their allotropes is investigated, including graphene, silicene, germanene, and MoS_2, with theoretical calculations based on density functional theory (DFT) implemented by the Vienna *Ab-initio* Simulation Package (VASP) code.

The atomic structure of graphene is that of an sp^2 bonded planar lattice. The band structure indicates that graphene is a semimetal with a Dirac cone at the K-point. Silicene and germanene have mixed sp^2-sp^3 buckled hexagonal structures and display similar electronic properties to those of graphene. Single-layer MoS_2 features a hexagonal packed layer composed of Mo atoms sandwiched between two layers of S atoms and appears to be a nonmagnetic semiconductor.

In order to alter the metallic properties, various adatoms are introduced on the graphene surface. A single H atom on top of a carbon atom in graphene pulls the bonded C atom out of the plane and creates a magnetic moment of 1 μ_B for graphene. Single F and O adatoms on graphene are adsorbed at the top site and bridge site, respectively, without any contribution of magnetic moment. The adsorption of a single F atom on graphene was found to be metallic. Single H and O adatoms on graphene transform the system into a semiconductor.

Under the inspiration of the graphene allotropes, new types of silicene allotropes, octasilicene, silicyne, and silicdiyne, are constituted and found to be buckled metallic materials. To fill unsatisfied valence shells and replace the dangling bonds with valence bonds in silicene allotropes, hydrogen atoms were introduced on silicene allotropes. Consequently, all the hydrogenated silicene allotropes appear to be semiconductors. The type of adsorption in which the dangling bonds are completely replaced by valence bonds is proved to be more stable, suggesting that the Si atom

favors sp^3 hybridization.

Fluorinated germanene keeps the chair configuration characteristic of pure germanene, which is the most stable configuration, but there is also a metallic structure for both types of fluorinated germanene.

The O atom was used to study the functionalization of single-layer MoS_2. The top of an S atom site is the most energetically favorable position, and the oxygen atom at this site results in a direct gap.

The electronic structures of a series of isostructural compounds, M_2SiO_4 (M = Mn, Co, and Ni), belonging to the olivine family, are studied by first principles calculations. The results show that the ground states of all the compounds are antiferromagnetic, which is consistent with the experimental results. The effects of the various M site ions on the crystal structure, spin states, orbitals, and electronic states, for ferromagnetic and antiferromagnetic magnetic states are investigated.

Two- and three-dimensional Ising–like models for a triangular spin-chain lattice are proposed to study the magnetic properties of a newly discovered triangular compound, $Sr_3Co_2O_6$, using Monte Carlo simulation. Simulations based on both of the two models show a multistep curve at low T, magnetization plateaus at M = 1/3 M_O, where M_O is the saturated magnetization, at intermediate T and paramagnetic behaviour at high T. The width of the plateau becomes larger as interactions increase.

ACKNOWLEDGEMENTS

I wish to express my sincere gratitude to my supervisors Prof. Xiao-Lin Wang, A/Prof. Zhen-Xiang Cheng, and Prof. Shi-Xue Dou, for their motivation, support and guidance during my three years of Ph.D. study in the Institute for Superconducting and Electronic Materials at the University of Wollongong. This thesis is a result of their consistent encouragement and the fruitful discussions I had with them.

I would like to express my appreciation to Prof. Francois Peeters for giving me the opportunity to work in the Condensed Matter Theory group (CMT) of the University of Antwerp and the chance to learn from their expertise in the field. I would like to thank Dr. Hasan Sahin for his guidance during the last year of my Ph.D. study. His willingness to answer all the questions I have had and his ability to recognize interesting research topics at an early stage have been indispensable for the results presented in this thesis.

I would like to acknowledge the University of Wollongong and the Chinese Scholarship Council for providing me scholarship during my three years of Ph.D. study.

Finally, I would like to take this opportunity to thank my husband, parents, family members and many friends for supporting and encouraging me throughout my study.

TABLE OF CONTENTS

LIST OF FIGURES

LIST OF TABLES

CHAPTER 1. LITERATURE REVIEW

1.1 Graphene

1.1.1 The Graphene Structure and Carbon Allotropes

Carbon is the major element for life and the basis of all organic chemistry. Because of the flexibility of its bonding, carbon-based systems, such as graphite, diamond, carbon nanotubes, and fullerenes, show an infinite number of structures with a large variety of physical properties, due to the dimensionality of these structures. Among the systems with only carbon atoms, graphene—a two-dimensional (2D) allotrope of carbon—plays a significant role, as it is the basis for understanding the properties of the other allotropes. Graphene was discovered in late 2004 at the Center for Mesoscopic and Nanotechnology at the University of Manchester in the United Kingdom, directed by A.K. Geim [1] and K.S. Novoselov. [2] Graphene was obtained by the cleavage of a single atomic layer from a sample of graphite by a piece of sticky tape.[3] Graphene is a one-atom-thick sheet of carbon atoms arranged in a honeycomb lattice. Carbon atoms are bonded trigonally to three other carbon atoms in a plane with sp^2 type hybridization. The nearest-neighbor distance between carbon atoms is 1.42 Å. The sp^2 hybridization between one *s*-orbital and two *p* orbitals (p_x, p_y) results in a trigonal planar structure, forming a σ bond between the carbon atoms. The σ band is responsible for the robustness of the lattice structure in all allotropes. These bands have a filled shell and constitute a deep valence band because of the Pauli

principle. The unaffected p_z orbital is perpendicular to the planar structure and can bind covalently with neighboring carbon atoms, forming a π band. Since each p_z orbital has one extra electron, the π band is half filled. As an allotrope of carbon, graphene is black in color and is a very soft material due to the fact that it has out of plane vibrational modes.

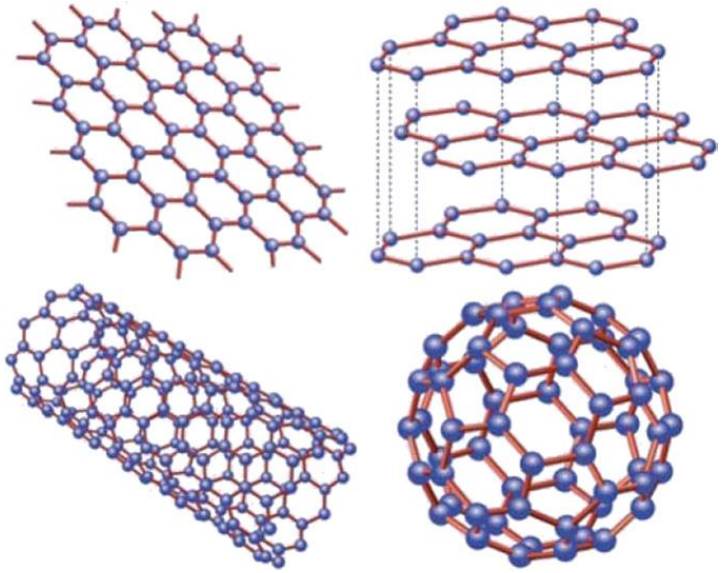

Figure 1.1 Graphene (top left) is a honeycomb lattice of carbon atoms. Graphite (top right) can be viewed as a stack of graphene layers. Carbon nanotubes are rolled-up cylinders of graphene (bottom left). Fullerenes (C_{60}) are molecules consisting of graphene sheets that are wrapped by the introduction of pentagons on the hexagonal lattice.[4]

Graphene is the building block of all the other allotropes. Fullerenes,[5,6] which are molecules where the carbon atoms are arranged spherically, are zero-dimensional (0D) objects with discrete energy states. Fullerenes can be made from graphene by the introduction of pentagons, and thus, fullerenes can be viewed as wrapped-up graphene. Carbon nanotubes[7] are obtained by rolling graphene along a given direction and

reconnecting the carbon bonds. Therefore, carbon nanotubes can be treated as one-dimensional (1D) objects with only hexagons. Graphite,[8] a three dimensional (3D) allotrope of carbon, is made out of stacks of graphene layers that only weakly interact by van der Waals forces. This force is responsible for the softness of graphite and leads to interactions between the covalently bonded layers. The delocalization of one of the outer electrons of each atom results in a π cloud, making graphite an electrical conductor, but each layer in the plane is covalently bonded. The interlayer distance is 3.34 Å with the stacking sequence of ABAB. [9]

1.1.2 Physical Properties

1.1.2.1 The Electronic Properties of Graphene

The structural flexibility of graphene is reflected in its electronic properties. One of the most important properties of graphene is the massless, chiral nature of the Dirac fermions and their low-energy excitations [3] (see Figure 1.2). The interference between electronic waves as they propagate through the graphene crystal contributes to this unusual electronic behavior. Thus, crystal symmetry 'protects' the 'diracness' of the electrons in graphene. At low energies and long wavelengths, the electrons in graphene are not characterized by their speed of propagation, the so-called Fermi–Dirac velocity, which is of the order of 10^6 m s^{-1} (that is, approximately 300 times smaller than the speed of light). The electrons in graphene obey a relativistic wave equation in two dimensions, and the chemical potential exactly crosses the Dirac point. This property has aroused great interest in the theoretical community. From the point of view of solid-state physics, however, graphene is also interesting because its electronic density of states vanishes linearly with energy at the Dirac point. Hence,

neutral graphene is a strange material, which is a combination between a metal and an insulator, a so-called semimetal. Graphene is not a metal since it has a vanishing density of states. Graphene is also not a semiconductor (or insulator) since it does not have a gap in its energy spectrum. Therefore, unlike a semiconductor, it does not have a threshold for electronic excitations.

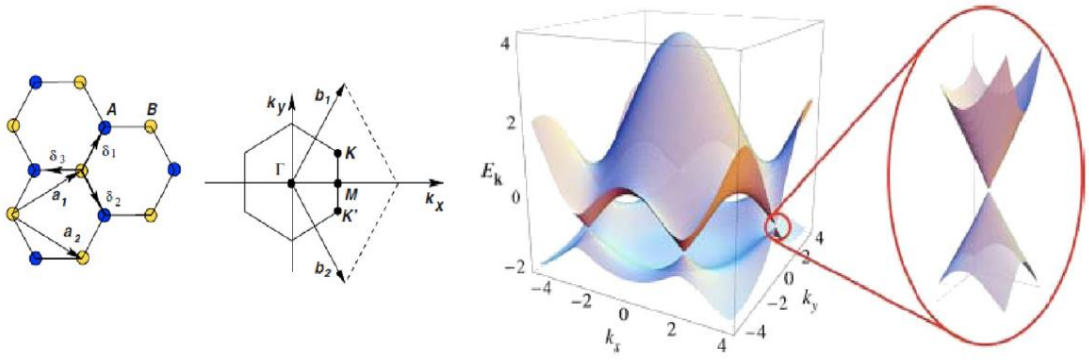

Figure 1.2 Left: lattice structure of graphene with sublattices A and B; Middle: graphene's Brillouin zone. Right: band structure of graphene with the Dirac cones located at the K and K′ points in the Brillouin zone.[10]

1.1.2.2 Anomalous Quantum Hall Effect

This peculiar dispersion that is characteristic of graphene simulates the physics of quantum electrodynamics (QED). Therefore, many of the abnormal properties of QED can berevealed in graphene at much smaller speeds.[4,11] Dirac fermions behave in irregular ways when compared to ordinary electrons if subjected to magnetic fields, resulting in new physical phenomena,[12,13] such as the anomalous integer quantum Hall effect (IQHE) measured experimentally.[14,15] The IQHE in graphene can be obtained at room temperature due to the large cyclotron energies for "relativistic" electrons[16]. As a matter of fact, the anomalous IQHE is the trademark of Dirac fermion behavior.

1.1.2.3 Electron Transport

Experimental results from transport measurements demonstrate that graphene has a significantly high electron mobility at room temperature, with reported values in excess of 15,000 $cm^2 \cdot V^{-1} s^{-1}$. In addition, the symmetry of the experimentally measured conductance reveals that electron and hole mobilities should be nearly the same.[17] The mobility is almost independent of temperature between 10 K and 100 K,[14] which indicates that defect scattering is the dominant scattering mechanism. Scattering of electrons by the acoustic phonons of graphene intrinsically restricts room temperature mobility to 200,000 $cm^2 \cdot V^{-1} s^{-1}$ at a carrier density of 10^{12} cm^{-2}. The corresponding resistivity of the graphene sheet would be 10^{-6} $\Omega \cdot cm$.

Graphene shows a minimum conductivity on the order of $4e^2/h$, despite zero carrier density near the Dirac points. Owing to graphene's two dimensions, charge fractionalization is considered to occur. Therefore, it may be a suitable material for constructing quantum computers[18] .

1.1.2.4 Mechanical Properties

Graphene appeared to be one of the strongest materials known, with a breaking strength over 100 times greater than that of a hypothetical steel film of the same (thin) thickness, with a Young's modulus of 1.100 GPa and a fracture strength of 125 GPa.[19] The Nobel announcement for Geim and Novoselov illustrated this by the statement that a 1 square meter graphene hammock would support a 4 kg cat but would weigh only as much as one of the cat's whiskers, at 0.77 mg (about 0.001% of the weight of a 1 m^2 sheet of paper). In particular, graphene's mechanical strength and flexibility are advantageous compared to indium tin oxide, which is brittle. Due to this

property, graphene can be used as a support membrane for transmission electronic microscopy (TEM). In addition, graphene can be used to hold macro and microscopic objects (DNA, nanoparticles) to make them visible through an electron microscope.

1.1.2.5 Thermal Conductivity

Graphene has a thermal conductivity of 5000 $Wm^{-1}K^{-1}$. [20] The thermal conductivity depends on the lateral dimensions of the graphene flakes. The surface area was found to be 2.630 m^2g^{-1}.[21] This property was measured at room temperature (300 K) and makes graphene suitable for use in nanotechnology applications. Graphene's high electrical conductivity makes it a candidate for transparent conducting electrodes, required for such applications as touchscreens, liquid crystal displays, organic photovoltaic cells, and organic light-emitting diodes (OLEDs).[22]

1.1.2.6 Spin Transport

Graphene is asserted to be an ideal material for spintronics, owing to its small spin-orbit interaction and the near absence of nuclear magnetic moments in carbon (as well as a weak hyperfine interaction). Electrical spin current detection and injection has been demonstrated up to room temperature. A spin coherence length above 1 micrometre was observed at room temperature, [23] and control of the spin current polarity with an electrical gate at low temperature was observed. [24]

1.1.3 Graphene Sample Preparation

Since the 2D nature of graphene exposes it to the environment, each carbon atom of the graphene crystal is able to interact with the surroundings. Most graphene samples are deposited or grown on a substrate with which they interact, while the other side of the graphene sheet is exposed to a vacuum or atmosphere. Variations in the atmosphere or nature of the substrate result in varying electronic properties of the graphene sample. For instance, the type of charge carriers in graphene, holes or electrons, relies greatly on the environment.

Therefore, it is significant to know the various preparation methods and experimental circumstances for graphene. Nevertheless, the preparation methods are being developed at an increasingly high pace, and these experimental circumstances are still under debate. In this section, an overview is given of the most common preparation methods so far. The possible environmental influences are handled later when essential.

Two major types of preparation techniques can be discriminated; those that start from graphite and in a variety of ways try to isolate few layer graphene (FLG) and finally monolayers (top-down approach), and those in which the graphene is really synthesized out of some non-related materials that include carbon atoms (bottom-up). Techniques of the first type will be defined as exfoliation methods, whereas techniques of the second type will be called synthesis methods.

1.1.3.1 Exfoliation Methods

As there is strong (covalent) bonding between the carbon atoms in a plane and weak van der Waals-bonding between the different planes, the layered structure of

graphite demonstrates a simple route to fabricate graphene, by destroying the inferior interlayer bonding and dividing the various planes. Nevertheless, some problems with this procedure might be presumed: how the layers can be kept apart after separation and how can this separation be done in a controllable way so that different samples include the same number of layers? The importance of these problems relies greatly on the real technique which is employed to fabricate the FLG.

1.1.3.1.1 Mechanical exfoliation

The very first preparation method to isolate a graphene sample was mechanical exfoliation[1]. In addition to its historical importance, mechanical exfoliation is still highly valuable. It is a widely employed technique particularly in academic research since the resulting sample quality is still unmatched by any of the more recent techniques. The notional briefness of this technique makes it extraordinary that it took so long to produce monolayer graphene samples. Virtually the whole preparation process comprises the repeated peeling of multilayered graphitic material from a very highly ordered pyrolytic graphite (HOPG) crystal with a cellophane tape and, subsequently, pressing the tape on a Si/SiO_2 substrate to deposit the graphene samples. The SiO_2 of the substrate must have a rigidly controlled thickness ($\sim$300 nm) to improve the optical contrast of a single layer of graphene by the interference effect. With an optical microscope, it is possible to differentiate between monolayer graphene and the many multilayered graphitic materials which are left behind on the substrate after removal of the tape. The size of the samples generated this way is on the order of several μm^2, however, placing a polymer coating on the substrate can enhance the adhesion of the graphene sheets, thus allowing the production of larger

(mm^2) pieces.

The graphene samples generated by mechanical cleavage possess perfect electronic quality and are free of defects, but there are some severe problems that are hard to conquer. This method seems impossible to utilize for mass production, as there is no control over the number of layers. The monolayers of graphene are generated among a myriad of FLG's, and they have to be hunted for with an optical microscope, so that exfoliation is hardly a high-throughput method for industrial applications. Hence, other techniques are required for these purposes.

1.1.3.1.2 Chemical exfoliation

A more recent technology for graphene production is to use a solution-based process to segregate the specific sheets in graphite.[25] This method uses an intermediate step to chemically modify graphite to make it water dispersible. One way is to oxidize graphite to form graphite oxide (GO) which can be injected with water to divide the layers.[26] Nevertheless, what is wanted is graphene, so that it is essential to deoxygenate the GO back to graphene. This can be done by chemical reduction in solution or thermal annealing. The puzzle with chemical reduction in solution is that the various layers rapidly aggregate after deoxidization because they are no longer soluble. Another method is thermal deoxidization by spraying the GO solution as a coating on a heated substrate such as SiO_2. The major good point of chemical exfoliation is its low cost and massive scalability. The quality of the samples is quite inferior, however, as many defects are introduced in the deoxidization process.

1.1.3.2 Synthesis Methods

Another strategy to yield graphene is from the bottom up by ‘gluing together’ precursor organic molecules or carbon atoms. This can be done in many ways and the different methods are being developed quite rapidly. It is possible to differentiate between three general approaches, however: organic synthesis in solution, thermal decomposition of a silicon carbide substrate, and chemical vapor deposition (CVD) on a metal substrate.

1.1.3.2.1 Organic synthesis

The synthesis of planar benzene-based macromolecules from polycyclic aromatic hydrocarbons (PAH) is a research field that originates from long before the discovery of graphene. The field is currently drawing great interest, however, as a likely path to graphene. The macromolecules are synthesized in solution, which limits their size, as the increasing weight of a macromolecule reduces the solubility and increases the formation of more 3D-like structures. This approach might turn into an attractive way to make graphene for electronic applications, with further development expected in the future.

1.1.3.2.2 Epitaxial graphene on silicon carbide

Another approach, which is probably one of the most promising techniques for large-scale graphene production, is to abstract graphene layer by layer from a silicon carbide (SiC) crystal surface by controlled heating in a suitable oxygen-containing atmosphere or vacuum. Much experimental and theoretical work has been carried out to identify the procedures behind the graphene formation on the SiC surface and this

has led to a legitimate comprehension of the considerable factors involved.[27] The most critical factor for the properties of the generated graphene multilayers is the surface from which they are abstracted.

The most applied crystal styles for the SiC are 4H-SiC and 6H-SiC. These are hexagonal lattices which contain two polar faces along the *c*-axis. When taking a limited slab of these crystals, this leads to two unequal surfaces, (0001) and $(000\bar{1})$, corresponding to Si-terminated and C-terminated surfaces, respectively. The development of graphene on these exterior surfaces takes place when the Si atoms are evaporated from the surface. The Si atoms tie up to oxygen to construct SiO molecules and desorb from the surface. The C atoms left behind are reconstructed to constitute graphene layers. The graphene layer closest to the SiC is named the buffer layer, which is chemically bonded to the C or Si atoms of the substrate so that the π-bands disappear in the electronic spectrum of this layer. The later layers show the Dirac spectrum typical of free-standing graphene.

1.1.3.2.3 Chemical Vapor Deposition

Perhaps the most promising future technique is chemical vapor deposition. This technique can be viewed as the growth of graphene on a heated metallic substrate in a well-chosen atmosphere including organic molecules. Various substrates (Ni, Cu, Ru, etc.) and atmospheres (CH_4/H_2, CH_4/H_2/Ar, etc.) have been tested, however, there is still much space for development. There are many merits of this approach by comparison with the other ones: it is possible to transfer the graphene samples to any other substrate after etching away the original substrate, and there is no restriction on the size of the samples because they cover the whole substrate; another significant result of this is the possibility of utilizing pre-patterned substrates to grow graphene

samples with a well-determined shape.[28]

1.1.4 Applications

It is apparent that the brilliant properties of graphene can result in significant new applications. These applications are the subject of much speculation, although some of these speculations are not being implemented so far.

1.1.4.1 High-speed Electronics

With the basic restrictions of silicon-based electronics in view, it is time to seek other materials to carry on the progress in electronic applications. Graphene might be a perfect candidate, since it apparently has many properties that make it useful in electronics: it possesses high mobility charge carriers at high carrier density and displays ballistic transport on a sub-micrometer scale at room temperature. Nevertheless, the real utilization of graphene in practical electronics is still quite restricted.

1.1.4.2 Transparent Electrodes

Indium tin oxide (ITO) is the most utilized material nowadays for the synthesis of conducting coatings for liquid crystal displays (LCD), solar cells and so on, although limited resources, high cost, and brittle nature of ITO significantly limit its application. The superior mechanical and chemical stability of graphene associated with its atomic layer thickness, high conductivity, and virtually infinite supply, make it a perfect candidate to replace ITO and become the dominant material for transparent

conducting electrode applications. In addition, graphene is much more flexible than ITO and hence, a perfect material to employ in touch screens, etc. The suitability of graphene for this kind of application has already been demonstrated.[28]

1.1.4.3 Sensors

Graphene is quite sensitive to external influences because of its low dimensionality, which is an advantageous feature for sensor applications and permits the conversion of graphene samples into nanosensors.

1.1.4.3.1 Mass sensors

Graphene can be transformed into a free-hanging, suspended membrane by etching away the SiO_2 substrate or deposition on a similar substrate with holes in it. As such, it can be manufactured as a high-frequency resonator, in which the frequency is extremely dependent on the particular adsorbed species. The subtlest mass divergences can be discovered in this way, owing to the low mass density of graphene.

1.1.4.3.2 Gas sensors

A novel generation of gas sensors has currently appeared with the arrival of semiconductor nanowires and carbon nanotubes. Due to the low dimensions of these materials, the charge carrier concentrations that are attributed to adsorbed gas molecules can result in detectable signals. The normal way to do this is by making use of these nanomaterials in a field effect transistor (FET) device, in which the adsorbing

molecules play the part of the gate voltage. The prompted resistivity changes can be surveyed, and a superior sensitivity is obtained in this way, permitting the detection of toxicant gases in concentrations on the order of one part per billion.

Graphene can be viewed as the most recent member of this new generation of gas sensors, and it possesses some beneficial properties which enhance the sensitivity even more.

- Graphene is a 2D material and has, as a result, its whole volume exposed to the possible adsorbate.
- Graphene is extremely conductive and thus has low Johnson noise[3] even without charge carriers.
- In its neutral state, there are no charge carriers in graphene, so that a few charge carriers can lead to distinguishable changes in the carrier concentration and thus the conductivity.
- Graphene crystals are nearly defect-free, which assures reduced noise owing to the thermal motion of defects.

The combination of all these properties permits the final discovery of individual molecular adsorption events with graphene sensors.[29]

1.2 Silicene and Germanene

1.2.1 Structural and Electronic Properties of Silicene and Germanene

The structural and electronic properties of the group-IV elements in graphene-like 2D sheets, such as those constructed from Si and Ge, have aroused great interest, both for their basic physical and chemical features and for their present and future technological appliances. 2D Si and Ge sheets are anticipated to provide a simply realized alternative for the improvement of the capability and scalability of the current silicon-based electronics. Silicene and germanene have 2D hexagonal lattices. On the basis of the minimization of the total energy, first-principles local-density functional methods suggest a buckled honeycomb structure for Si and Ge in these forms in contrast to the planar honeycomb lattice of graphene.[30]

Based on the first-principles methods of structural optimization, finite temperature molecular dynamics, and phonon modes, it was found that although the planar and highly buckled structures of Si and Ge are not stable (Figure 1.3), low-buckled (LB) honeycomb structures can be stable, with an equilibrium buckling of ΔLB of 0.044 nm.[31] The band structures in the LB constructions of Si and Ge are ambipolar, and their charge carriers can include a massless Dirac fermion at the K point due to the π and π^* bands, which linearly cross at the Fermi level. It also was predicted that the magnetic and electronic properties of silicene and germanene nanoribbons would show geometry and size dependence. The Fermi velocities in the vicinity of the Dirac point were calculated to be 6.3×10^5 m/s, 5.1×10^5 m/s and 3.8×10^5 m/s for graphene, silicene, and germanene, respectively.[32] Most of the other known properties

of silicene and germanene are similar to those of graphene. The distinct properties of silicene, however, have the capability to offer a fresh future for the Si-based electronics industry.

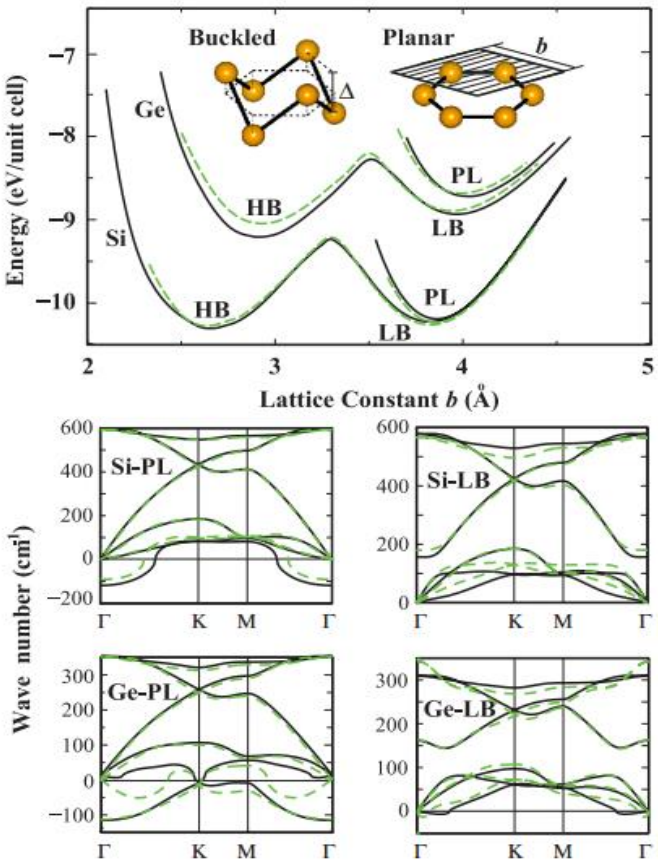

Figure 1.3 Energy versus hexagonal lattice constant of 2D Si and Ge are calculated for various honeycomb structures (top). Black (dark) and dashed green (dashed light) curves of energy are calculated by the local density approximation (LDA) using projector augmented wave (PAW) method potentials and ultrasoft pseudopotentials, respectively. Planar and buckled geometries, together with buckling distance Δ and the lattice constant of the hexagonal primitive unit cell, *b*, are shown in the insets. Lower panels: Phonon dispersion curves obtained by force-constant and linear response theory are presented with black (dark) and dashed green (dashed light) curves, respectively.[31]

The sp^3 hybridization shown in silicon, which gives rise to the general covalent Si-Si bonds, is the most preferred construction compared with the sp^2 or the various sp^2-sp^3 orbitals. Guzman-Verri et al.[33] devised a tight binding (TB) Hamiltonian of buckled silicene from the structure of a monatomic sheet of Si (111) and predicted that the silicene is a zero-band-gap semiconductor with electrons that appear as massless Dirac fermions around the K point, on the basis of a second-nearest-neighbor sp^3 orthogonal tight-binding model. Wang[34] carried out a comparative density functional theory (DFT) study on the orbital hybridization behaviors of the 2D phases of carbon, silicon, and germanium. The progression in lattice configuration and chemical bonding from 3D to 2D structures was probed by spreading the spacing between the basal layers. During the spreading process, there was an interim change from sp^3 to sp^2 hybridization in carbon. A relevant transition was not found in the silicon and germanium phases, however. Further study of the electronic energy band spectra and the atomic angular-momentum projected density of states (DOS) of the three materials confirmed that the chemical bonds are sp^3-like in silicene and germanene. The consequence is the existence of various lattice structures in comparison with the single one of graphene. For the LB geometry of silicene (germanene), the lattice constant (a) and the distance between the nearest neighbor atoms (d) are 3.86 Å (4.02 Å) and 2.28 Å (2.42 Å), respectively.[35]

The above analysis implies that the most stable configuration of a 2D silicon and germanium sheet is low-buckled because of the undermining of the π–π overlaps by the larger separation of atoms. Therefore, in the light of quantum chemistry, the production of siliceous sp^2-like analogs is not possible. In spite of this, flat germanene[36, 37] and silicene[38] configurations with sp^2 hybridization were also investigated by the use of DFT calculations, within the local density approximation

(LDA). It was demonstrated that, unlike the gapless semiconductor silicene, planar silicene with sp^2 hybridized atomic orbitals is a very reactive surface. Planar germanene is electropositive, with a low density of states at the Fermi level. The reactivity derives from the lesser overlap between the $3p_z$ orbitals of the neighboring Si atoms. The inferior π bonds can be simply broken on exposure to external species such as hydrogen and oxygen, and afterwards, they continue to form chemical bonds with them. This causes an sp^2 to sp^3-like hybridization, as found in bulk Si.[38] De Padova et al. predicted sp^2-like hybridization of silicon valence orbitals in silicene nanoribbons synthesized on an Ag(110) substrate.[39] The results indicate that the valence silicon orbitals exhibit sp^2-like hybridization analogous to that of the carbon atomic bonds of graphene. Such abnormal sp^2-like hybridization, however, rather than the more common sp^3-like hybridization of free-standing sheets, is most likely to be due to the Ag(110) substrate. On the other hand, the theoretically studied reactivity of sp^2-hybridized silicene with external chemicals[38] contrasts greatly with the outstanding stability obtained for pristine silicene nanoribbons grown on Ag(110). The latter demonstrate a powerful resistance to oxidation.[39] The oxidation started at quite high oxygen exposure levels. Defects in the silicene sheets turned out to increase oxygen uptake.

1.2.2 Synthesis of Silicene Nanosheets

In spite of the intense theoretical studies of the structural and electronic features of silicene and germanene, there are just a few experimental investigations on silicene sheets, but there has been no experimental study on germanene so far. This is attributed to the difficulty in synthesizing samples. The possibility of epitaxial growth

of silicon on silver contributed to the construction of Si nanowires on Ag(110) with heights of about 0.2 nm and homologous widths of about 1.6 nm, but different lengths. The Si nanowires were made up by direct-current flashing on a piece of Si wafer in an ultra-high vacuum (UHV) chamber. As inspected by a scanning tunneling microscope (STM), the nanowires were all aligned along the $[\bar{1}10]$ orientation of the Ag substrate.[40] These Si nanowires were reinvestigated, and the results indicated that there were four silicon hexagons in a honeycomb array inside the nanowires. Such an intricate configuration of the asymmetric nanowires was illustrated by the use of *ab initio* DFT calculations. After full geometry optimization, the Si honeycomb configuration exhibited a striking buckling, as viewed in the STM image. This is due to the asymmetric structure in the charge density profile. Consequently, the silicon nanowires synthesized on Ag(110) were viewed as silicene nanoribbons in the form of an arc with a height of roughly 0.2 nm. This is the proof that silicene was probably synthesized on Ag(110) or even of the physical presence of silicene.

The electronic features of the silicene nanoribbons synthesized on Ag(110) were studied by various techniques.[41] Angle-resolved photoelectron spectroscopy (ARPES) measurements demonstrated that the spectrum of the silicene nanoribbons exhibited outstanding electronic states in the proximity of the Fermi level at roughly 0.92, 1.45, 2.37, and 3.12 eV (Figure 1.4), in comparison the surface state of pristine Ag(110). These states along the Ag[001] direction were derived from lateral confinement within the 1.6 nm nanoribbons since they were not distributed as in the regular emission as functions of the photon energy. Analogous to graphene on various surfaces, the obvious downwards shift of the bands was due to the charge transfer from the Ag(110) substrate to the silicene nanoribbons. Furthermore, the opening up of the band gap was attributed to the vaulted honeycomb structure of the nanoribbons

on the substrate. This investigation implies that the silicene nanoribbons exhibited quantum restricted electronic states due to their 1D property, being mediated by the silver surface.

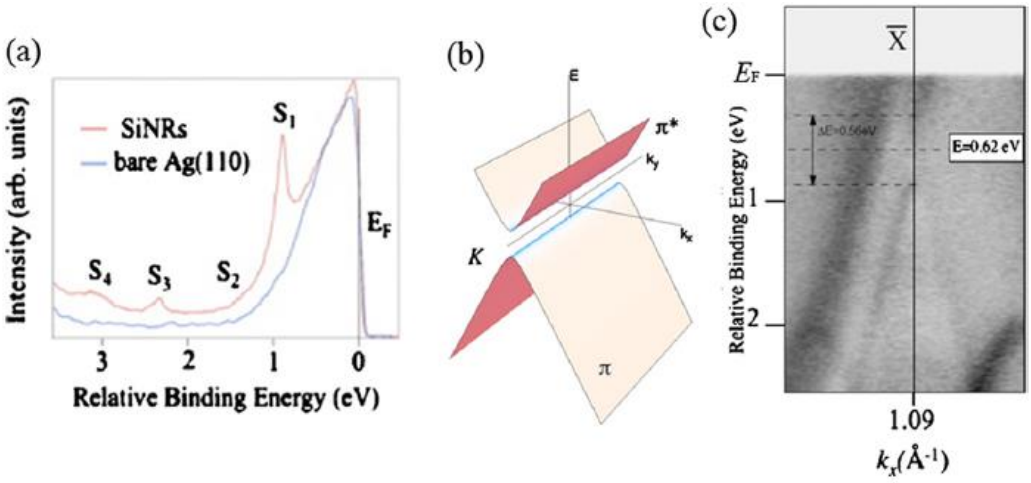

Figure 1.4 (a) Electron energy distribution curves for bare Ag(110) and for the array of Si nanoribbons. (b) 1D projection of the π and π* cones around the Dirac points. (c) Horizontal slice I (E, k_x) along the [$\bar{1}$10] Ag direction, integrated on k_y from 0.55 to 0.7 $Å^{-1}$ for the dense array of Si nanoribbons on Ag(110).[41]

Based on STM observations, a successful monolayer silicene sheet was later reported to have been favorably synthesized on an Ag(111) surface.[42] Under UHV conditions, the Ag(111) substrate was purged in some sputtered circles, which was followed by annealing at 400 ℃ until a penetrating (1 × 1) pattern of the Ag surface was acquired. The silicene sheet was fabricated by depositing Si from a piece of Si wafer onto the Ag(111) substrate, which was heated at roughly 250 ℃. The experimental conditions for generating the silicene sheet turned out to be very severe, because the substrate temperature must be kept between 220 ℃ and 250 ℃. The deposition rate of Si has to be lower than 0.1 monolayer/min. The STM image presented a honeycomb structure made up of two silicon sublattices located at

positions with various heights. The divergence of approximately 0.02 nm might possibly demonstrate sp^2-sp^3 hybridization. The Si-Si nearest-neighbor distance of 0.19 ± 0.01 nm, was about 17% shorter than that for bulk Si, implying that the Ag substrate may play a catalytic role in the stabilization and formation of the silicene sheet, or there might be intense interaction between the silicene and the Ag(111) substrate. It was proposed, however, that a weak electronic interaction between the silicene sheet and the Ag(111) substrate was most probable, since the epitaxial $(2\sqrt{3} \times 2\sqrt{3})R30°$ low-energy electron diffraction (LEED) mode was not found in the STM images. It was reported that these results were also extremely dependent on the deposition rate of Si atoms onto the substrate and the substrate temperature.[43] It should also be noted that the Si-Si nearest-neighbor distance ranges between 0.228 and 0.25 nm, and the apparent Si-Si distance can be as low as 0.189 nm, owing to the buckling in a silicene sheet, according to theoretical research.[44]

So as to offer significant evidence for the existence of silicene, Vogt et al. carried out systematic research on Si superstructures deposited on Ag(111), utilizing a set of techniques involving STM, ARPES, and LEED, combined with DFT calculations.[45] Si atoms were deposited on an Ag(111) substrate, which was maintained at 220-260 ℃. Vogt et al. observed that the Si/Ag ratio was enhanced linearly with the deposition of Si from measuring the Ag 4*d* band emission and the Si 2*p* core level. The LEED results corresponded to a (4 × 4) symmetry with respect to the bare Ag(111)-(1 × 1) surface, which is consistent with the structure implied by the STM results (Figure 1.5). From these results, the proposed structure is a (4 × 4) Si adlayer, namely, 2D silicene, on the Ag(111) surface. The ARPES data indicates that the vertex of the Si cone on Ag(111) is roughly 0.3 eV beneath the Fermi level, which is the result of the interplay with the Ag(111). They also defined the bond angles of the

Si atoms in order to offer information on the hybridization states. The bond angle is nearly 110 ° for the six top Si atoms of the (4 × 4) unit cell. This is close to that of an sp^3 hybridized Si atom at 109.5 °. Among the 12 lower Si atoms that are left over, six are merely sp^2 hybridized with a bond angle of approximately 120 °, whereas the other six have bond angles between approximately 112 ° and 118 °. This demonstrates mixed sp^2-sp^3 hybridization. These various bond angles of the Si atoms are attributed to the substitution of the Si atoms along the *z* direction.

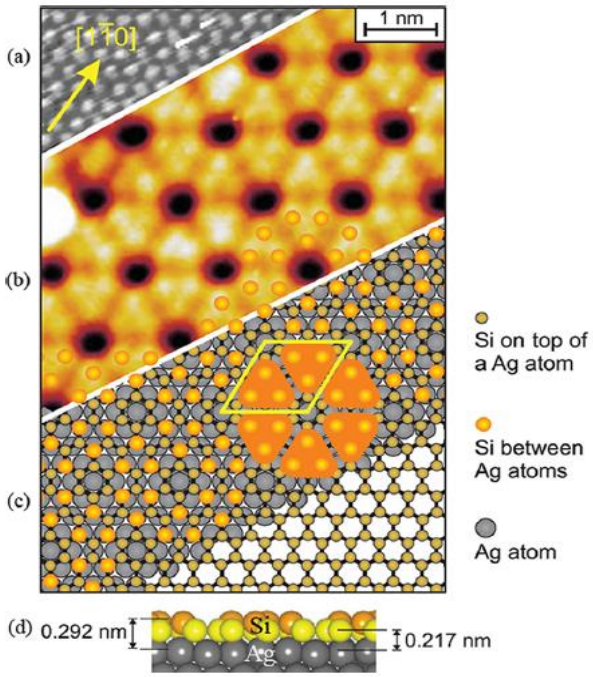

Figure 1.5 Construction of the atomic structure model for the 2D Si adlayer. (a) Filled-states in an STM image of the initial clean Ag(111)-(1 × 1) surface. (b) Filled-states in an STM images of the (4 × 4) silicene sheet on Ag(111). (c) Model of silicene on Ag(111). Si atoms sitting on top of Ag atoms are highlighted as larger orange balls, resembling the measured STM image. In the bottom right corner, the ball-and-stick model for the freestanding silicene layer is shown with a Si-Si distance of 0.22 nm. (d) Side view of DFT results for silicene on Ag(111).[45]

Feng et al.[46] found Si superstructures with a periodicity of 1.18 nm using STM, which is almost nearly three times that of silicene, 0.38 nm, or four times that of the lattice constant of the Ag(111)-(1 × 1) surface, 0.29 nm, when Si is deposited on an Ag(111) surface. They established that the observed structures were in the shape of a (3 × 3) reconstruction regarding the (1 × 1) silicene lattice. They found that disordered protrusions and a honeycomb structure can coexist at a substrate temperature of 143 ℃. Furthermore, a dense honeycomb structure, silicene, was constructed at 227 ℃. No silicon structure was observed above 327 ℃, however. With growth in the coverage of silicon, stacked multilayer silicon structures could also be constructed. The resemblance of the local density of states between the bilayer silicene and monolayer silicene may demonstrate inferior couplings between the monolayer silicene and the Ag(111) substrate. Based on these investigations, a Fermi velocity as large as 106 m/s and a linear energy momentum dispersion relation were derived. These consequences confirm that the quasi-particles in silicene manifest as massless Dirac fermions. The derived properties are analogous to those observed for graphene. Nevertheless, the essence of the substrate contribution to the observed characteristics or the electron interaction of the Ag substrate is still unclear.

Besides these reported superstructures of Si atoms grown on Ag substrate, there is currently also a report of Si superstructures grown on a ZrB_2 surface.[47] The reconstructed Si sheet on the ZrB_2 was constructed by a surface isolation method from the Si substrate, onto which the ZrB_2 was deposited. A direct π- electron band gap at the Γ point was observed because of buckling of the silicene, which was caused by the epitaxial strain from the ZrB_2 surface. Based on the STM results it was also found that the electronic behavior of the reconstructed Si sheets relied on the local Si phases.[48] In spite of these reports, there is no proof that a free-standing silicene sheet has been

generated so far.

2D Si-based sheets can also be created by a solution based method.[49] In order to fabricate silicon sheets by the use of hexagonal layered calcium disilicide ($CaSi_2$), Nakamo et al.[50] first adulterated the $CaSi_2$ with Mg so that the charge on the negatively charged silicon layers could be decreased. The $CaSi_{0.85}Mg_{0.15}$ was then exfoliated in a solution of propylamine hydrochloride (PA·HCl). Consequently, the authors gained a product with the ratio of Si: Mg: O = 7.0: 1.3: 7.5, which was determined by X-ray photoelectron spectroscopy. The products were Mg doped monolayer sheets with a predominant ⟨110⟩ direction and involved oxidized Si. Okamoto et al.[51] exfoliated a layered polysilane (Si_6H_6) through a reaction with *n*-decylamine to fabricate oxygen-free silicon nanosheets. This reaction resulted in nanosheets with the Si (111) planes bound covalently to amines. The thickness of the "free-standing" sheets was measured to be less than 2 nm. The nanosheets displayed photolumiscence (PL) emission at 435 nm, indicating that the nanosheets are direct-band-gap materials. Furthermore, monolayer organosilicon nanosheets, $Si_6H_xPh_{6-x}$, were also fabricated by the reaction of Si_6H_6 with phenyl magnesium bromide.[52] These results indicated that silicon-based nanosheets can be acquired through the chemical modification of Si_6H_6, in which the interlayer coupling is weaker than that of $CaSi_2$. Nevertheless, these efforts also suggest that the fabrication of pure 2D silicon nanosheets through solution-based approaches is harder than the relevant fabrication of other stratified materials.

1.3 Layered Transition Metal Dichalcogenides (TMDs)

1.3.1 Electronic and Magnetic Properties of Pristine TMDs

Three-dimensional MX_2 compounds, where M is a metal, form one of the most fascinating types of materials, exhibiting a wide range of significant features such as superconductivity,[53] half-metallic magnetism,[54] semiconductivity, and charge density waves,[55] as well as having applications in different areas comprising catalysis,[56] lubrication,[57] supercapacitors,[58] photovoltaics,[59] and rechargeable battery systems.[60] Layered TMD crystals feature two-dimensional hexagonal lattices consisting of MX_2 sandwiches, based on the coordination of the transition metal atom by the chalcogens.[61] Layered TMDs can be metallic (e.g., M = Nb, Re) or semiconducting (e.g., M = Mo, W), depending on the oxidation state and the coordination of the metal atoms. MoS_2 is one such prototypical TMD materials. Contrary to *h*-BN and graphite, the layers of MoS_2 are composed of hexagons with the Mo and S_2 atoms situated at alternating corners (Figure 1.6). MoS_2 has been considered for dry lubrication, as a hydrodesulfurization catalyst which is utilized to eliminate sulfur compounds from oil[62], and for hydrogen evolution.[63] Bulk MoS_2 has also drawn great interest for its use in photocatalytic[64] and photovoltaic[65] materials, due to its vigorous absorption in the solar spectral region. The quantum confinement effect on the optical properties and electronic structures was demonstrated in MoS_2 nanotubes[66] and nanoplates[67]. The most noticeable property of MoS_2, in contrast to insulating *h*-BN and zero-band-gap graphene, is that bulk MoS_2 is a semiconductor with an indirect band gap of 1.29 eV.[68]

Several investigations[69,70] have proved that there is a transition from an indirect band gap to a direct band gap for MoS_2 compound as the thickness of the MoS_2 is reduced to a monolayer. This explains the more than 10^4-fold increase in the photoluminescence (PL) quantum yield detected from monolayer MoS_2. The abnormal electronic structure of monolayer and few-layer MoS_2 and the resulting distinct optical features derive from properties of the *d*-electron orbitals that are involved in the valence and conduction bands of MoS_2.[71] Structural variation in the chemically exfoliated MoS_2 thin films (< 5 nm) that is caused by Li intercalation during chemical exfoliation induced the PL to vanish, however. The observed thermal effect is beyond the range of the classical temperature-dependent PL feature of semiconductors.

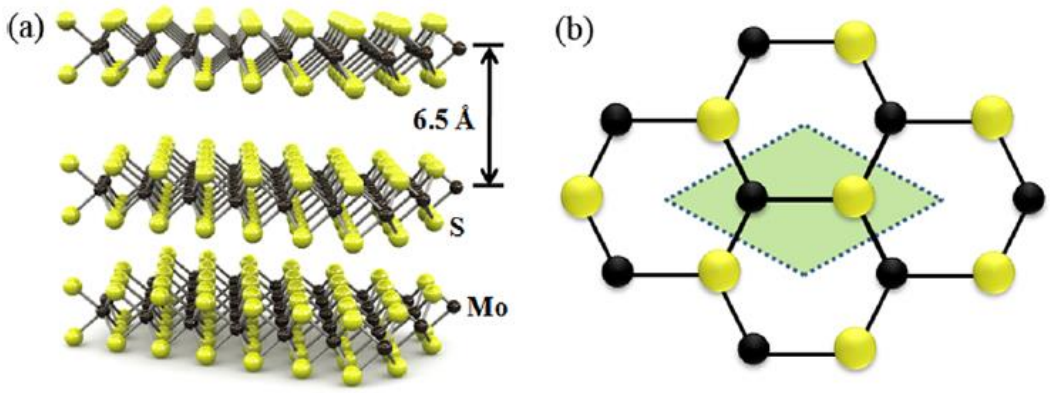

Figure 1.6 (a) Atomic structure of layered MoS_2. Different sheets of MoS_2 are composed of three atomic layers, S-Mo-S, where Mo and S are covalently bonded. (b) Top view of the honeycomb lattice, emphasizing the inversion symmetry breaking.[77]

Kuc et al. carried out a further investigation of the effects of quantum confinement on the electronic structures of monolayer and few-layer MS_2 (M = W, Nb, Re) by first-principles calculations.[72] They observed that WS_2 is similar to MoS_2 and

undergoes an indirect (bulk) to direct (monolayer) band-gap transition (Figure 1.7). Quantum confinement-prompted indirect to direct band gap crossovers are also present in $MoTe_2$ and $MoSe_2$ monolayer sheets with a direct band gap of 1.07 and 1.44 eV, respectively.[73] On the other hand, NbS_2 and ReS_2 remained metallic, independent of the number of layers. These calculations were performed by spin-polarized DFT calculations.

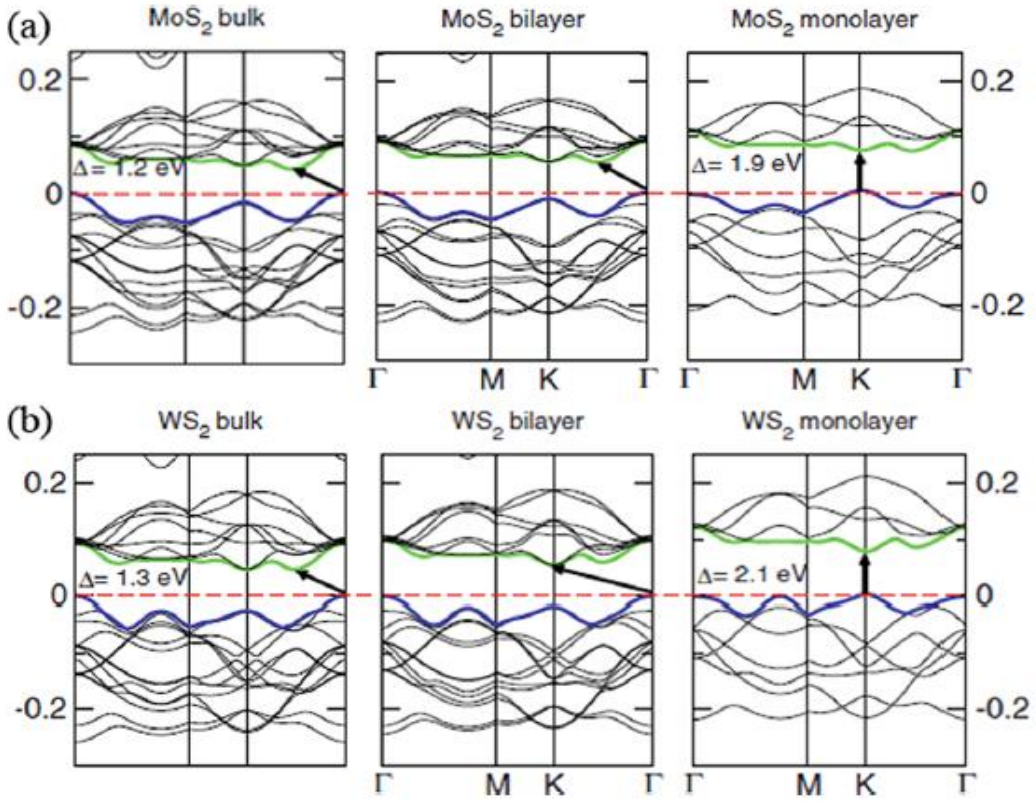

Figure 1.7 Band structures of (a) bulk MoS_2, its monolayer, and bilayer; (b) bulk WS_2, its monolayer, and bilayer, calculated at the DFT/Perdew-Burke-Ernzerhof (PBE) level. The horizontal dashed lines indicate the Fermi level. The arrows indicate the fundamental band gap (direct or indirect) for a given system. The top of the valence band (blue/dark gray) and bottom of the conduction band (green/light gray) are highlighted.[72]

In the case of bilayer WS_2, MoS_2, $MoSe_2$, and $MoTe_2$, DFT calculations demonstrate that their basic indirect band gaps[74,75]can be continuously altered to zero by introducing external electric fields which are perpendicular to the layers. The results show that the scope of gap tunability is much wider than in bilayer graphene. As a common tendency for MoX_2, the critical electric field for the semiconductor to metal transition is reduced in the sequence S to Se to Te (Figure 1.8). This regularity is due to the increasingly diffuse nature of the valence p_z orbitals in transitioning from S to Te, facilitating more charge transfer from the chalcogen to Mo under the same electric field. The effects of changing the transition metal from Mo to W, however, while keeping the chalcogen (S), do not appear great.[76]

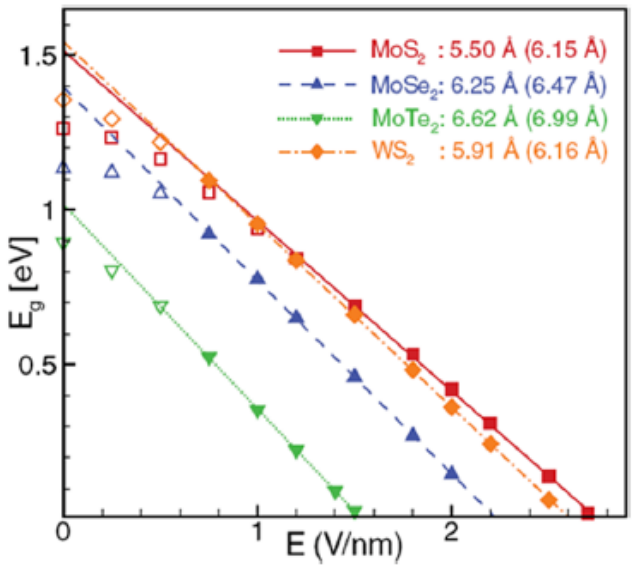

Figure 1.8 Band gap E_g versus applied electric field E for MoS_2, $MoSe_2$, $MoTe_2$, and WS_2. The lines are fits to the linear portion of the curve indicated by the solid symbols. The hollow symbols are within the region of nonlinear response and are excluded from the fits. The GSE coefficients (magnitudes of the slopes of the linear fits) are indicated; interlayer spacings are in parentheses.[76]

1.3.2 Synthesis of TMD Sheets

Mechanical exfoliation is still the best approach for dividing layered TMD crystals for the purpose of studying their intrinsic physical properties. The representative features of PL from FETs of MoS_2 layers that have been revealed to date primarily originate from mechanically exfoliated MoS_2 sheets.[69,77] Solution-based exfoliation can be utilized to easily generate bulk admixtures of single-layer and multilayered TMD materials. Such a procedure can include organic solvents,[78,79] lithium ion intercalation,[80,81] or surfactants.[80] Coleman et al.[78] reported that few-layer TMD materials, including MoS_2 and WS_2, can be produced by a surfactant-free liquid-exfoliation method. Furthermore, Zhou et al.[79] discovered that suspensions consisting of few-layer WS_2 and MoS_2 sheets can be efficiently created by the use of low-boiling-point solvent mixtures containing water and ethanol. The solvents can simply be cleared away due to their low boiling points. When exfoliation was performed in aqueous surfactant solutions, the result was the creation of large-scale few-layer TMD sheets. One of the disadvantages of liquid exfoliation is the trouble in preparing monolayer TMD sheets in both organic solvents and aqueous surfactant solutions. The monolayer semiconducting TMD sheets have unique optical and electronic characteristics, which are distinct from those of bilayer, few-layer, and bulk TMDs, as discussed above. Therefore, an approach which can prepare monolayer sheets is extremely desirable. Ion intercalation is an approach that can prepare monolayer sheets effectively. For instance, high-yield production of monolayer TMDs, which includes MoS_2, WS_2, TiS_2, and ZrS_2, could be obtained through a relatively complex lithiation process.[82] Ion intercalation is environmentally sensitive and time-consuming, however. The greatest disadvantage of the intercalation process is the structural deformation of the original TMD materials caused by the ion intercalation.[80]

For example, exfoliation of MoS_2 does not result in monolayer MoS_2 but monolayer Li_xMoS_2. The structural deformation can significantly influence the optical and electronic properties of the single-layer TMD sheets.[83] Besides exfoliation methods, there are an increasing number of other methods to produce monolayer or few-layer TMD sheets. In the past, techniques such as chemical reactions, CVD, sputtering,[84] pulsed laser deposition (PLD)[85] and thermal evaporation[86] have all been utilized to prepare single- and few-layer TMDs sheets. It has been reported that MoS_2 monolayer islands with lateral sizes of tens of nanometers were formed using electron beam deposition of molybdenum on a Cu (111) surface pre-coated with thiophenol.[87]

Zhan et al. introduced the vapor-phase growth of single and few-layer MoS_2 sheets by direct elemental chemical reaction.[88] The reason for the weak electrical properties of the synthesized MoS_2 was not explained by the authors, but one possibility is that it is due to the weak structural impurities and inhomogeneity in the MoS_2 films. This was proposed based on Raman spectroscopy of the comparatively large peak width, yet small peak intensity of the E^1_{2g} Raman mode.

Lee et al. synthesized monolayer or few-layer MoS_2 sheets on chemically produced graphene oxide, perylene-3,4,9,10-tetracarboxylic dianhydride modified SiO_2 substrate, or perylene-3,4,9,10-tetracarboxylic acid tetrapotassium salt by use of the reactants MoO_3 and sulfur at 650 ℃ in flowing N_2.[89] It was observed that the surface treatment induced growth of the MoS_2 sheets, and increased their mobility in bottom-gated transistors on a SiO_2/Si platform to around 0.02 $cm^2/(V\ s)$.

Liu et al. produced integrated high-quality, large-area, mostly trilayer, MoS_2 thin layers, by the thermolysis of ammonium thiomolybdates $(NH_4)_2MoS_4$ in Ar/H_2 atmosphere and further annealing in sulfur vapor.[90] In contradiction to conventional CVD methods, a substrate such as SiO_2/Si or sapphire was bathed in the $(NH_4)_2MoS_4$

solution, with dimethyl formamide (DFM) as the solvent to create a thin $(NH_4)_2MoS_4$ membrane on the substrate. The prime cause for the improved crystallinity of the trilayer MoS_2 films synthesized with sulfur vapor was due to the eradication of oxygen species, which is in line with TEM-based energy dispersive spectroscopic analysis (EDS). The PL and Raman spectra of trilayer MoS_2 films demonstrated that the quality of the MoS_2 layers synthesized on sapphire is better than for those synthesized on SiO_2/Si. The annealing with sulfur greatly improved the electrical properties of the MoS_2 devices with SiO_2 as the dielectric layer. The electron mobility and on/off current ratio of trilayer MoS_2 devices, grown on sapphire with sulfur and Ar as the annealing atmosphere, was greater compared with those grown without sulfur during annealing.

Monolayer MoS_2 nanoclusters were grown at 727 ℃, while multilayer (2-5 layers) nanoclusters were grown at 927 ℃, in the case of graphite substrate. [91] The former had higher cluster coverage than the latter because of the stacking that was generated, while the total amount of Mo remained the same. It was also observed that a lower annealing temperature did not result in a comparatively good crystalline order of the MoS_2 nanoclusters. The MoS_2 nanoclusters grown on HOPG show a hexagonally truncated shape terminated by both S-edges and Mo-edges, in contrast to the triangular shape of the MoS_2 nanoclusters on Au(111) that were terminated only with Mo-edges. This was due to the stable influence of hydrogen on the S-edge and the reduced chemical potential of sulfur at higher temperature. A varied rotation angle of the MoS_2 relative to the HOPG from cluster to cluster was observed due to lattice mismatch and rotation between the HOPG and the single-layer MoS_2 nanoclusters, which illustrates that the interaction between the HOPG and the MoS_2 basal plane and lattice is quite inferior due to van der Waals interactions.[92] This also confirms that the

defects induced by ion bombardment play a significant role in bonding the MoS_2 nanoclusters. The favorable three-dimensional synthesis of stacked MoS_2 nanoclusters at 927 ℃ reveals tangibly that the adherence of the topmost layers of the MoS_2 nanoclusters to the lower layers was stronger than that on defects on the substrates or on the HOPG (0001). Due to the existence of electronic edge states lying at the two outermost atomic rows rather than the general interlayer van der Waals bonding, the stacking of the multilayer MoS_2 nanoclusters was most probably achieved by interlayer bonding at sites near the cluster perimeter. The two styles of low-index MoS_2 edges were determined for multilayer MoS_2, which are the completely sulfide S-edge and the Mo-edge completely saturated with sulfur. These results demonstrate how to obtain high-quality large-area single- or few-layer MoS_2 sheets by manipulating experimental elements such as the growth time, temperature, annealing atmosphere, precursors, and substrate surface.

There have also been some achievements in fabricating other kinds of TMDs. Two dimensional WS_2 nanosheets down to 2-3 layers were synthesized by the chemical reaction of carbon disulfide (CS_2) with tungsten oxide ($W_{18}O_{49}$) nanorods in a hot hexadecylamine solution.[93] In a particular process, hexadecylamine (1.45 g, 6 mmol) and tungsten oxide nanorods (40 mg) were added to a 50-mL three-neck round-bottom flask under Ar. The reaction blend was first heated to 100 ℃ to remove water and then heated to 250 ℃. After infusing CS_2 (0.12 mL, 2 mmol), the resulting solution was further heated to 330 ℃. The initially blue solution gradually changed into the final dark brown one during the reaction.

1.3.3 Analysis of the Existence of Monolayer TMD Sheets

Even though single- and few-layer examples of MoS_2, WS_2, TiS_2, and ZrS_2 have been synthesized, not all of the possible 88 various combinations of MX_2 compounds can be stabilized in free-standing, monolayer honeycomb-like structures, as estimated by first-principles geometry optimization and phonon calculations on the basis of DFT.[94] The results of electronic properties and stability analysis of 44 stable single-layer MX_2 sheets are summarized in Figure 1.9. The stable monolayer MX_2 sheets can be ferromagnetic, nonmagnetic metals, or semiconductors. Semiconducting single-layer 2H-MX_2 sheets show various band structures. The semiconducting transition metal oxides (M = Sc, Cr, Mo, W; X = O) vary from the other group (M = Cr, Mo, W; X = S, Se, Te) by their comparatively lower band-edge state densities and smaller band gaps. All MO_2 honeycomb structures turn out to be indirect-band-gap semiconductors, whereas the other group is composed of direct semiconductors. For all monolayer MX_2 semiconductors, the band gap rises as M goes from Sc to W. In the case of MX_2 (X = O, S, Se, Te), analogous band structures were also obtained as M goes from V to W. Virtually, they are either semiconductors or metals according to the number of *s* and *d* valence states of the free M atoms. Some other instances are worth mentioning: In the case of ScX_2 (X = O, S, Se), the magnetic moment is located at the site of the chalcogen atoms, since a great amount of charge, deriving from the relatively lower electronegativity of Sc, is transferred from Sc to X. 2H− FeX_2 or VX_2 (X = O, S, Se, Te) are found to be ferromagnetic metals, and their magnetic moments depend on the *d* orbital of the transition metal atoms. The mechanical properties of the monolayer MX_2 sheets were assessed by in-plane stiffness rather than Young's modulus. The calculated in-plane stiffness values of the monolayer MX_2 are evaluated in the range of 9 to 250 N/m, which is smaller than the corresponding value for

graphene (357 N/m) and BN (267 N/m) sheets.

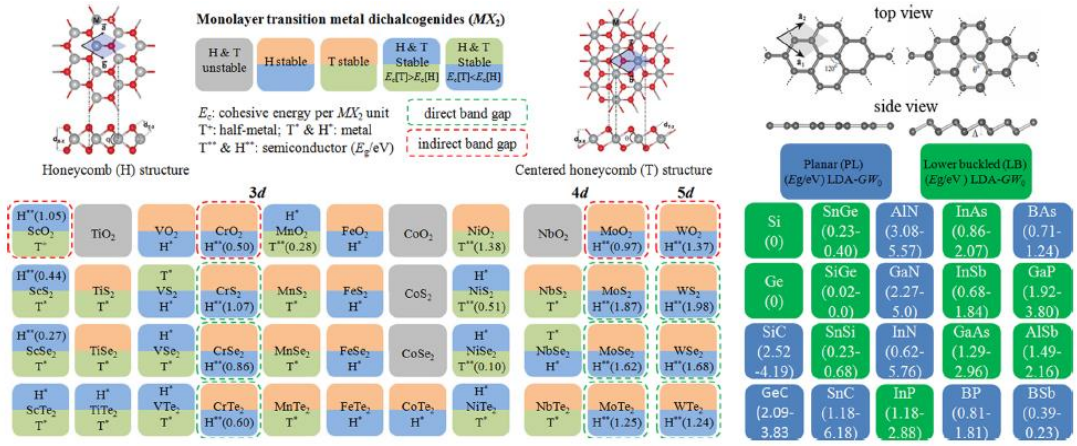

Figure 1.9 Summary of stability analysis and semiconducting properties of 44 different MX_2 compounds and binary compounds of group-IV elements and group III−V compounds. Transition metal atoms indicated by M are divided into 3d, 4d, and 5d groups. MX_2 compounds (shaded light gray) form neither stable H (2H-MX_2) nor T (1T-MX_2) structures. In each box, the lower-lying structure, honeycomb or centered honeycomb (H or T) structure, is the ground state. The resulting structures (T or H) can be half-metallic (+), metallic (*), or semiconducting (**) with direct or indirect band gaps. [95]

In contrast to the intensive research efforts devoted to graphene, the electronic and other related properties of layered TMD materials, especially compounds other than MoS_2, have still not been investigated to any great extent. An appropriate approach for large-scale composites of sustained high-quality single or few-layer MoS_2 or other relevant semiconductors is yet to be exploited. It is necessary to fabricate suitable optoelectronic devices that explore properties deriving from non-zero band-gap semiconductors. It should be stressed that the conventionally utilized quartz-tube-based furnaces are not appropriate for massive and continuous production of large-

scale, high-quality, and homogeneous graphene sheets, because of the non-equal arrangement of gaseous carbon precursors, the trapping of reaction by-products in the copper foils, as well as the thermal field between the curled copper foils.[96] A roll-to-roll procedure was reported to synthesize graphene on flexible Cu foils by atmospheric CVD.[97] In addition, the treatment of substrates and the preparation of metal catalysts on the substrates cannot be completed by these systems. There are production systems for continuous and scalable growth of 2D materials, which use wheel arrays to controllably convey substrates along the production line, from the growth of substrates, the treating of substrates, the depositing of catalysts on the substrates, to the formation of 2D films.

1.4 Goal of this thesis

As the 2D layered materials display exotic properties and these properties could be controlled by attracting other atoms and molecules, by which new two-dimensional crystals can be created with designed electronic and other properties, this thesis is mainly focused on computational research on functionalization of typical monolayer honeycomb lattices, such as graphene, silicene, germanene, and MoS_2, and also some of their allotropes, by employing density functional theory (DFT) as implemented in the VASP package.

The thesis is organized as follows. Chapter 2 contains a brief discussion of DFT and ways to solve the Kohn-Sham equations. In Chapter 3, graphene is used as an example to introduce the computational procedures. The effects of the adsorption of a single H, F, or O atom on the electronic and magnetic properties of graphene are discussed. Three graphene allotropes, octagraphene, graphyne, and graphdiyne are

analyzed by first-principles calculations. Their calculated properties are consistent with previous studies, which confirms the correctness of our calculation method. Under the inspiration of the graphene allotropes, new types of silicene allotropes, octasilicene, silicyne, and silicdiyne, are developed in Chapter 4. The structural and electronic properties of these silicene allotropes are investigated. Various types of adsorption of H atoms are applied to the three silicene allotropes, in order to alter their electronic properties. From the optimized structure and formation energy, it can be concluded that the Si atom favors sp^3 hybridization. Chapter 5 contains a systematic study of fluorinated germanene. Three configurations, chair-like, boat-like, and zigzag-like structures, are considered for partially and fully fluorinated germanene, which display different structural and electronic properties. Chapter 6 shows the general effects of the adsorption of a single oxygen atom on the electronic and magnetic properties of perfect single layer-MoS_2.

Besides the two-dimensional layered structures, this study also shows that some other types of materials are also of great interest. Chapter 7 is devoted to a theoretical study of the olivine-type silicates with the general formula M_2SiO_4 (M = Mn, Co, and Ni). By employing the CASTEP module of Material Studio 6.0, the magnetic and electronic states of Mn_2SiO_4, Co_2SiO_4, and Ni_2SiO_4 are presented, based on the first-principles calculation method in the framework of density functional theory. Furthermore, motivated by the experimental observations of step-like magnetization in the compound $Sr_3Co_2O_6$, the magnetic properties of two- and three-dimensional (2D and 3D) Ising models for a triangular spin-chain lattice in a magnetic field are explored systematically by Monte Carlo simulation in Chapter 8. Our calculated results can be fitted to experimental observations in a consistent manner.

CHAPTER 2. METHODOLOGY

Since the development of quantum mechanics in the early 20th century, materials have been known to consist of atomic electrons and nuclei whose behavior can be described by the quantum mechanical Schrödinger equation. To solve the Schrödinger equation by using a many-particle wave function is a formidable task, however, because the dimensions of the wave function are proportional to the number of particles in the system, and the number usually is very large. On the other hand, some chemical phenomena were explained successfully with the concept of electron density, which induced physicist to find a relation between the electron density and the state of the particular system, such as the energy. The dimensions of the electron density are always three, which is independent of the number of electrons, so that it is possible to perform the calculation. Using electron density rather than the wave function was initially proposed by Thomas and Fermi in 1927.[98, 99] This was seen as an approximation to the Schrödinger equation, however. The status of the electron density approach was greatly improved by Hohenberg and Kohn[100] in 1964. They showed that this approach was as theoretically able to find exact energies as the ones obtained from the Schrödinger equation. The theoretical framework that they devised for this task is called *Density Functional Theory* (DFT), which can be regarded as a method equivalent to solving the Schrödinger equation for the energy, but avoiding many of the difficulties related with many-body wave functions.

2.1 The Electronic Structure Problems

2.1.1 Background

Our primary interest in the electronic structure problem is finding the energy of many electron systems in different external potentials, such as the potential of an atomic nucleus. It is necessary to solve the non-relativistic time-independent Schrödinger equation:

$$H\Psi(\mathbf{r_1},\mathbf{r}_2,\cdots,\mathbf{R_1},\mathbf{R}_2,\cdots)=E\Psi(\mathbf{r_1},\mathbf{r}_2,\cdots,\mathbf{R_1},\mathbf{R}_2,\cdots) \tag{10.1}$$

where Ψ is the wave function of the system, $\mathbf{r}_i$ and $\mathbf{R}_i$ are the positions of the electrons and nuclei respectively and H is the Hamiltonian for the system:

$$H=-\sum_i\frac{\hbar^2\nabla_i^2}{2m_e}-\sum_{i,I}\frac{1}{4\pi\varepsilon_0}\frac{Z_Ie^2}{|r_i-R_I|}+\frac{1}{2}\sum_{i\neq j}\frac{1}{4\pi\varepsilon_0}\frac{e^2}{|r_i-r_j|}-\sum_I\frac{\hbar^2\nabla_I^2}{2M_I}+\frac{1}{2}\sum_{I\neq J}\frac{1}{4\pi\varepsilon_0}\frac{Z_IZ_Je^2}{|R_I-R_J|} \tag{10.2}$$

where m_e is the electron mass, and Z_I and M_I are the nucleus charge and mass respectively. The Hamiltonian can be decomposed into five items:

$$H=T_N+T_e+V_{int}+V_N+V_{ext} \tag{10.3}$$

where T_N and T_e are the kinetic energy operators of the nuclei and electrons, respectively; V_{int} expresses the Coulomb interaction between the electrons, while V_N represents the Coulomb interaction between nuclei; V_{ext} is the potential energy of the electrons in the field of nuclei. Since only the types of atoms and the positions of all the particles (electrons and nuclei) determine the properties of a macroscopic material, knowing them is, in principle, adequate to calculate the energy and the wave function of the system. These calculations are known as *ab initio* calculations or first-principles calculations, as they are based only on the values of Nature's constants or the laws of physics, such as the electron charge e and Planck's constant $\hbar$. For

simplicity, atomic units will be used in the following ($\hbar = m_e = e = 4\pi\varepsilon_0 = 1$).

In practice, however, it is just possible to solve the Schrödinger equation exactly for tiny simple systems such as the hydrogen atom. For larger systems such as solids and molecules, additional approximations have to be considered.

2.1.2 Born-Oppenheimer Approximation

The *Born-Oppenheimer approximation* separates the motions of electrons from those of nuclei. This is due to the fact that the masses of nuclei are much heavier than that of electrons, so that the nuclei move much more slowly than electrons. Under the *Born-Oppenheimer approximation*, nuclei are fixed, so that the kinetic energy of nuclei, T_N, is neglected and the Coulomb interaction between nuclei, V_N, is treated as a constant. The wave function can be expressed as a product of the nuclear wave function and the electron wave function.

$$\psi(\boldsymbol{r}_1, \boldsymbol{r}_2, \cdots, \boldsymbol{R}_1, \boldsymbol{R}_2, \cdots) = \psi_{elec}(\boldsymbol{r}_1, \boldsymbol{r}_2, \cdots; \boldsymbol{R}_1, \boldsymbol{R}_2, \cdots) \cdot \chi_{nuc}(\boldsymbol{R}_1, \boldsymbol{R}_2, \cdots) \tag{10.4}$$

Note that the ionic positions after the semicolon in the electron wave function are parameters (which are different from variables). The Schrödinger equation of the electrons for a given frozen ionic configuration is described as follows:

$$H_{elec}\psi_{elec} = E_{elec}\psi_{elec} \tag{10.5}$$

where

$$H_{elec} = T_e + V_{int} + V_{ext} \tag{10.6}$$

The total energy E_{tot} is the sum of E_{elec} and the constant repulsion energy for nuclei, E_N

$$E_{tot} = E_{elec} + E_N \tag{10.7}$$

In the following, we only describe the electron part and the subscript "*elec*" will be dropped.

2.1.3 The Hartree-Fock Approximation

Now we have to deal with the electronic part of the Hamiltonian. Among the approximate methods to solve such a many-electron equation, the Hartree-Fock (HF) method has an important status because it is often the starting point to obtain more accurate calculations of the quantum mechanism. The idea is to reduce Eq. (10.5) to a one-particle equation for an electron which moves in an average potential from all the electrons.

It starts from using the single Slater determinant as an approximation to the wave function of the ground state of the N-electron system:

$$\psi(\boldsymbol{r}_1,\boldsymbol{r}_2,\cdots,\boldsymbol{r}_n)=\frac{1}{\sqrt{n!}}\begin{vmatrix} \phi_1(\boldsymbol{r}_1) & \phi_2(\boldsymbol{r}_1)\cdots\phi_n(\boldsymbol{r}_1) \\ \phi_1(\boldsymbol{r}_2) & \phi_2(\boldsymbol{r}_2)\cdots\phi_n(\boldsymbol{r}_2) \\ \cdot & \cdot & \cdot \\ \cdot & \cdot & \cdot \\ \cdot & \cdot & \cdot \\ \phi_1(\boldsymbol{r}_n) & \phi_2(\boldsymbol{r}_n)\cdots\phi_n(\boldsymbol{r}_n) \end{vmatrix} \tag{10.8}$$

The reason is that electrons are fermions which obey the Pauli exclusion principle, which requires the antisymmetric wave function. Then, the "best" approximate wave function can be determined by the variational principle. In quantum mechanics, it is declared that if E_0 is the ground state energy solution of the Schrödinger equation, for any wave function φ,

$$\frac{\langle\varphi|H|\varphi\rangle}{\langle\varphi|\varphi\rangle}\geq E_0 \tag{10.9}$$

Invoking the variational principle with the Slater determinant, the "best" solution can be found by the Hartree-Fock equation:

$$\begin{aligned}[-\sum_i \frac{\nabla_i^2}{2} - \sum_I \frac{Z_I}{|r_i - R_I|} + \sum_j \int \phi_j^*(\mathbf{r}_j) \frac{1}{|r_i - r_j|} \phi_j(\mathbf{r}_j)] \phi_i(\mathbf{r}_i) \\ -\sum_j \int \phi_j^*(\mathbf{r}_j) \frac{1}{|r_i - r_j|} \phi_i(\mathbf{r}_j)] \phi_j(\mathbf{r}_i) = \varepsilon_i \phi_i^*(\mathbf{r}_i)\end{aligned} \tag{10.10}$$

The first three items indicate that electron *i* is treated independently but in an effective potential determined by the other electrons. The last item is the exchange potential which comes from the antisymmetric nature of the Slater determinant.

The Hartree-Fock approach changes the many-body problem into an independent one electron problem. The electronic correlation is neglected, however, because of the single Slater determinant approximation, so that there is a difference between the exact energy and the Hartree-Fock energy. Many approaches exist to adopt this correlation energy such as the Møller-Plesset (MP) perturbation theory[101] and the Coupled Cluster method.[102] Due to the computational expense, however, the calculation can currently be performed only on the smallest systems.

Density Functional Theory (DFT), on the other hand, provides a good compromise between the computational effort required to generate the results and a qualitative description of the electronic structure. Thus, DFT is one of the most successful and popular quantum mechanical methods used to describe matter, to calculate the electronic band structures of solids in physics, and to estimate the binding energy of molecules in chemistry. Since we use DFT to solve the electronic Hamiltonian in this thesis, we will briefly explain the fundamental concepts and the theoretical framework of DFT in the following section. More details can be found from books.[103,104]

2.2 Density Functional Theory

2.2.1 The Thomas-Fermi Model

The most famous early work on using the electron density rather than the wave function was introduced by Thomas and Fermi.[98,99] The electron density n is expressed as

$$n(\boldsymbol{r}) = N\iint\cdots\int |\Psi(\boldsymbol{r_1},\boldsymbol{r_2},\cdots,\boldsymbol{r_N})|^2 d\boldsymbol{r_2}d\boldsymbol{r_3}\cdots d\boldsymbol{r_N} \qquad (10.11)$$

where N is the total number of electrons in the system and satisfies the particle conservation law $\int n(\boldsymbol{r})d\boldsymbol{r} = N$. In this model, they derived the kinetic energy of electrons from the quantum statistical theory based on a uniform electron gas and treated the electron-electron (-nucleus) interaction classically. Then, the total energy in terms of electron density is

$$E[n] = C_F\int n^{5/3}(\boldsymbol{r})d\boldsymbol{r} - \int\frac{Zn(\boldsymbol{r})}{r}d\boldsymbol{r} + \frac{1}{2}\iint\frac{n(\boldsymbol{r_1})n(\boldsymbol{r_2})}{|\boldsymbol{r_1}-\boldsymbol{r_2}|}d\boldsymbol{r_1}d\boldsymbol{r_2} \qquad (10.12)$$

where C_F is a constant. The first term in the equation is the kinetic energy of the electrons. The second and third terms are the electron-nucleus and electron-electron interactions, respectively. The bracket parentheses [ ] denote the functional dependence.

The importance of the Thomas-Fermi model is that it shows that the energy can be determined from only the electron density. The modern theory of DFT is based on the Hohenberg-Kohn (HK) theorems, however.

2.2.2 The Hohenberg-Kohn Theorems

Modern density functional theory was born in 1964 with a paper of Hohenberg and Kohn (HK). They proved two well-known theorems (which are known as the HK theorems).[100]

Theorem I: *For any system of interacting particles in an external potential* $V_{ext}(\boldsymbol{r})$, *the potential* $V_{ext}(\boldsymbol{r})$ *is determined uniquely, except for a constant, by the ground state density* $n_0(\boldsymbol{r})$.

Theorem II: *A universal functional for the energy* $E[n]$ *in terms of the density* $n(\boldsymbol{r})$ *can be defined, valid for any external potential* $V_{ext}(\boldsymbol{r})$. *The exact ground state energy of the system is the global minimum of this functional, and the density that minimizes the functional is the exact ground state density* $n_0(\boldsymbol{r})$.

The first theorem implies that 1) if we know the ground state electron density, $n(\boldsymbol{r})$ we could obtain all the other properties of the system; 2) the ground state energy can be defined explicitly as a function of the electron density:

$$E_{HK}[n] = T[n] + E_{int}[n] + \int V_{ext}(\mathbf{r}) n(\mathbf{r}) d\mathbf{r} \tag{10.13}$$

where $E_{HK}[n]$ is the total energy functional, $T[n]$ is the kinetic energy and $E_{int}[n]$ is the energy due to the electronic interactions. The second theorem demonstrates that the ground state energy can be obtained by the variational principle, which can be expressed as:

$$E_0[n_0] \leq E_V[n] \tag{10.14}$$

where $E_V[n]$ is the energy functional of Eq. (10.13) with the external potential V_{ext}. Note that using the HK formulation of DFT implies that we are working at $T = 0$ K.

2.2.3 The Kohn-Sham Equations

Although the HK theorems demonstrate that the electron density can stringently become the fundamental quantity of the many-body problem, they do not say anything on how to find the accurate electron density. In 1965, Kohn and Sham[105] (KS) proposed a method to solve the problem of Eq. (10.13). The idea was to change the many interacting electrons to non-interacting electrons moving in an effective potential.

By introducing the kinetic energy of non-interacting electrons, T_S , and the Coulomb interaction, J (the third term of Eq. (10.12)), the energy functional can be written as

$$\begin{aligned} E[n] &= T[n] + V_{int}[n] + V_{ext}[n] \\ &= T_s[n] + J[n] + V_{ext}[n] + E_{xc}[n] \end{aligned} \tag{10.15}$$

where $E_{xc}[n]$ is the *exchange correlation energy*

$$E_{xc}[n] = T[n] - T_s[n] + V_{int}[n] - J[n] \tag{10.16}$$

By taking variational principle, one electron Schrödinger-like equations can be obtained

$$H_{KS}\phi_i = \left[-\frac{1}{2}\nabla^2 + V_{eff} \right]\phi_i = \varepsilon_i \phi_i \tag{10.17}$$

where ϕ_i and ε_i are the KS-orbitals and the corresponding orbital energies, respectively. The V_{eff} is called the *KS-effective potential*

$$V_{eff}\left(\mathbf{r}\right) = J + V_{ext} + V_{XC} = \int \frac{n(\mathbf{r}')}{|\mathbf{r} - \mathbf{r}'|} d\mathbf{r}' + V_{ext}\left(\mathbf{r}\right) + V_{XC} \tag{10.18}$$

where V_{XC} is *the exchange correlation potential*

$$V_{XC} = \frac{\delta E_{XC}[n(\mathbf{r})]}{\delta[n(\mathbf{r})]} \tag{10.19}$$

and the electron density n is

$$n(\mathbf{r}) = \sum_{i=1}^{N} |\phi_i|^2 \tag{10.20}$$

Eqs. (10.17)-(10.20) are the well-known Kohn-Sham equations. The new term, the exchange correlation potential, V_{XC}, includes all the many-body effects that are not shown in the Hartree-Fock approach, so that the equations provide the exact result of the electronic problem.

It should be noticed that the *effective potential* V_{eff} is related to the electron density $n(\mathbf{r})$. So, the Kohn-Sham equations have to be solved self-consistently. The procedure to solve the KS equations is usually to start with an initial guess of the electron density, build the V_{eff}, and solve Eq. (10.17) to obtain the KS orbitals ϕ_i. The new electron density, which is determined by the orbitals, is used to repeat the process until convergence is achieved. The exact form of the exchange correlation functional $E_{xc}[n]$ is unknown, however, so some approximations have to be taken.

2.2.4 The Exchange-Correlation Approximations

2.2.4.1 The Local Density Approximation (LDA)

LDA is the simplest approximation of the exchange-correlation energy. It is based on two assumptions: 1) the local exchange-correlation energy per particle is only based on the local density; 2) the exchange-correlation energy is taken to be that of a homogeneous electron gas. Then, the exchange-correlation energy E_{xc} is defined by the sum of the contributions of each point in space, and the contribution of one point is independent of the other points. So, it can be written as

$$E_{xc}^{LDA}[n] = \int n(\mathbf{r})\varepsilon_{xc}(n(\mathbf{r}))d\mathbf{r} \tag{10.21}$$

where ε_{xc} represents the exchange-correlation energy per particle of the uniform electron gas of density $n(\mathbf{r})$. The ε_{xc} can be further divided into correlation and exchange parts,

$$\varepsilon_{xc}(n(\mathbf{r})) = \varepsilon_x(n(\mathbf{r})) + \varepsilon_c(n(\mathbf{r})) \tag{10.22}$$

The exchange part, $\varepsilon_x = -\frac{3}{4}\sqrt[3]{3n(\mathbf{r})/\pi}$, is the exchange energy of an electron in a uniform electron gas. The correlation part, ε_c, is fitted by using the quantum Monte-Carlo simulations of the homogeneous electron gas of Ceperly and Alder.[106]

Although the LDA is more accurate for systems with slowly changing densities, it has been proven to be a good approximation in practice. It describes the correct picture of binding trends across the periodic table and properly describes the bond lengths, structures, phonon spectra, and other properties for many systems. The binding energies of solids and molecules are usually overestimated, however.

2.2.4.2 The Generalized Gradient Approximation (GGA)

While the LDA only take the local electron density into account, the GGA also takes account of the contribution from the gradient of the density $\nabla n(\mathbf{r})$ at each coordinate. This can be expressed as:

$$E_{xc}^{GGA}[n] = \int n(\mathbf{r})\varepsilon_{xc}(n(\mathbf{r}), \nabla n(\mathbf{r}))d\mathbf{r} \tag{10.23}$$

In practice, the GGA improves some results over those of the LDA, gives reliable results for all the main types of chemical bonds, and achieves very good results in some fields, such as with molecular geometries and ground-state energies. The GGA has a great many versions. In surface physics, the most widely used version is

PW91 [107] and its relative PBE, which was proposed by Perdew-Burke- Ernzerhof (PBE). [108] Since two-dimensional materials are the main focus in this thesis, calculations in this thesis are based on PBE.

2.2.5 Bloch's Theorem

Real materials contain huge number of ions and electrons (usually ~10^{24}/cm^3). In principle, all of these should be considered to build the Kohn-Sham Hamiltonian. However, it is impossible to accomplish this by any numerical method. In order to solve the problem, the periodic structure of the materials has to be considered in order to simplify the problem. Then, the KS effective potential, V_{eff}, in the Kohn-Sham equation is periodic for the crystal lattice vectors $\boldsymbol{R}$, i.e. $V_{eff}(\boldsymbol{r}+\boldsymbol{R}) = V_{eff}(\boldsymbol{r})$.

Bloch's theorem states that the eigenstates ϕ of a one-electron Hamiltonian can be written as

$$\phi_{n\boldsymbol{k}}(\mathbf{r}) = e^{i\mathbf{k}\cdot\mathbf{r}} u_{n\boldsymbol{k}}(\mathbf{r}) \tag{10.24}$$

where $u_{n\boldsymbol{k}}$ is a function with the periodicity of the lattice such that $u_{n\boldsymbol{k}}(\boldsymbol{r}) = u_{n\boldsymbol{k}}(\boldsymbol{r}+\boldsymbol{R})$. The subscript n is the band index and $\boldsymbol{k}$ is the crystal wave vector. $\boldsymbol{k}$-values lie in the first Brillouin zone of the reciprocal lattice because, for any reciprocal lattice vector $\boldsymbol{G}$, $\phi_{n\boldsymbol{k}} = \phi_{n,(\boldsymbol{k}+\boldsymbol{G})}$. Also, energy eigenvalues are periodic in reciprocal space, i.e. $E_n(\boldsymbol{k}) = E_n(\boldsymbol{k}+\boldsymbol{G})$.

Bloch's theorem has transformed an infinite many-electron problem into a problem of infinite k-points inside the first Brillouin zone. Since the total energy needs to be calculated by the integral over the first Brillouin zone, an approximation has to be taken by using only a discrete number of k-points. The most widely used

approach was proposed by Monkhorst-Pack.[109] They approximate the integral with an equidistant grid of $\boldsymbol{k}$-vectors with identical weight:

$$\boldsymbol{k}_{m_1,m_2,m_3} = \sum_{i=1}^{3} \frac{2m_i - q_i - 1}{2q_i} \boldsymbol{b}_i \qquad \text{with} \qquad m_i = 1, 2, ..., q_i \tag{10.25}$$

where q_i is the discretization number in the direction of the reciprocal lattice vector $\boldsymbol{b}_i$. Thus, the total number of k-points is $q_1 \times q_2 \times q_3$. The number can be decreased by considering the symmetry of the system, which can effectively speed up the calculation.

It is worth noting that the number of k-points which is required to give a good estimate of the system depends on all aspects of the system such as size and structure. Thus, it is necessary to check if the k-point grid can give converged results. One also has to be careful when the energies of the unit cell are compared in different sizes, unless either equivalent k-points are used or the total energy is found to be conserved. In this thesis, the Monkhorst-Pack k-point scheme is used.

2.2.6 Plane Wave Basis Set

In Eq. (10.24), the periodic functions $u_{n\boldsymbol{k}}(\boldsymbol{r})$ are still unknown. The common method to treat them is to do the expansion by plane waves. The reasons are that 1) $u_{n\boldsymbol{k}}(\boldsymbol{r})$ are periodic functions; 2) it is easy to transform between real space and reciprocal space by fast Fourier transformations (FFT); 3) the plane waves are independent of atomic positions. Thus, $u_{n\boldsymbol{k}}(\boldsymbol{r})$ can be expanded as

$$u_{n\boldsymbol{k}}(\boldsymbol{r}) = \sum_{\boldsymbol{G}} c_{n\boldsymbol{k},\boldsymbol{G}} e^{i\boldsymbol{G}\cdot\boldsymbol{r}} \tag{10.26}$$

where the summation is over all the reciprocal lattice vectors $\boldsymbol{G}$ of the system. The

greater the number of plane waves that are used to describe the Bloch wave function, the more accurately the results can be obtained. This cannot be done, however, without truncating to a finite set. The parameter we are using to do the truncation is the so called cut-off energy, E_{cut}. Then, only the plane waves whose kinetic energies are below E_{cut} are considered in the computation, which is

$$\frac{|k+G|^2}{2} < E_{cut} \tag{10.27}$$

2.2.7 Pseudopotentials

Pseudopotential approximations are used to reduce the calculation further. They are based on the fact that most physically interesting properties of solid mainly depend on the valence electrons. The deeply bound core electrons, however, which are less important, require a large number of plane wave basis functions for their description because of their fast oscillations in the core region. Thus, the pseudopotential approximations are used to remove the core electrons and replace the strong ionic potential by weaker pseudopotential V_{pseudo}. A schematic representation is displayed in Figure 2.1. From the figure, we can see that the V_{pseudo} is much weaker than the real potential and that the pseudo wave function has no radial node in the core region. At the same time, both of the potentials and both of the wave functions are exactly the same (norm-conservation) beyond a chosen radius r_c, which is known as the cut-off radius.

Pseudopotentials are softer with a larger cut-off radius, which is more rapidly convergent in terms of the basis set, but the applications are limited because this

approach is less accurate for reproducing realistic features in different environments. There are several types of norm-conservation pseudopotentials from different authors such as Troullier and Martins,[110] Kerker,[111] Hamann, Schlüter, and Chiang,[112] and Vanderbilt.[113]

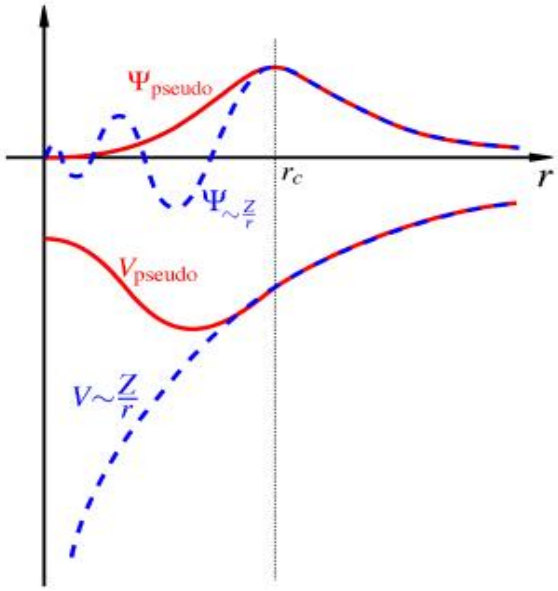

Figure 2.1 Schematic representation of the real potential (dashed line) and pseudo potential (solid line) and their corresponding wave functions. The vertical line indicates the cut-off radius r_c.

2.2.7.1 Ultrasoft Pseudopotentials

The advantage of norm conservation is that it makes the norm of the pseudo wave functions the same as for real all-electrons wave functions within the cut-off radius. The disadvantage is that the pseudopotentials cannot be smoother than the real potentials for elements with strongly localized orbitals, such as O *2p*- or Ni *3d*-orbitals. The consequence is that they still require a large plane-wave basis set.

To overcome the problem, Vanderbilt[114] made a modification to relax the norm-

conserving constraint. The pseudo wave functions are not normalized inside the cut-off radius, but keep the same density as the real ones. This kind of pseudopotential is called an ultrasoft pseudopotential. It enables much lower plane-wave cut-offs to be used in the calculations.

2.2.7.2 Projector Augmented Wave Method

The ultrasoft approximation used in this thesis is the projector augmented wave (PAW) method, which was introduced by Blöchl[115] in 1994. The method is based on the linear transformation of the pseudo wave function $\tilde{\psi}_n$ to the real all-electron wave function ψ_n. The transformation is expressed as:

$$|\psi_n\rangle = |\tilde{\psi}_n\rangle + \sum_i (|\phi_i\rangle - |\tilde{\phi}_i\rangle)\langle p_i|\tilde{\psi}_n\rangle \tag{10.28}$$

where *n* and *i* are the band and atom index, respectively. The $\tilde{\phi}_i$ are the pesudo-partial waves, which are nodeless and identical to the real partial waves ϕ_i outside the core radius. The projector functions p_i have to be determined by:

$$\langle p_i|\tilde{\psi}_j\rangle = \delta_{ij} \tag{10.29}$$

As can be seen from Eq. (10.28), the real all-electron wave function is expressed by three items. The first item is the pseudo wave function, $\tilde{\psi}_n$, which is identical to the true state outside the core region. The second item is the real all-electron core partial wave function, ϕ_i, which is identical to the all-electron core state ψ_n. The last item is the pseudo core partial wave, $\tilde{\phi}_i$, which is identical to the pseudo core states. Figure 2.2 schematically shows the basic concept of the PAW method.

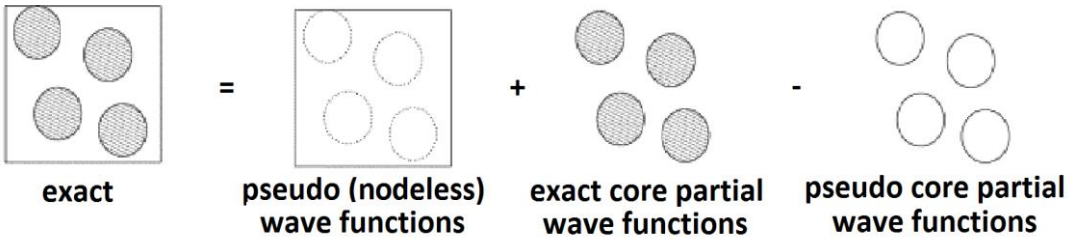

Figure 2.2 Schematic representation of the basic concept of the PAW method.

Thus, The PAW method, implemented in the Vienna *Ab-initio* Simulation Package (VASP), works directly with the all-electron valence wave functions and all-electron valence potentials, which is important for the calculation of properties such as nuclear magnetic resonance (NMR)[116] because it strongly depends on the wave function near the nucleus. Finally, the combination of DFT, the plane-wave basis set, and pseudopotentials, which has become a well-established methodology, is used to conduct the calculation on the electronic structure of condensed matter in this thesis.

CHAPTER 3. SINGLE ATOMS ADSORPTION ON GRAPHENE AND GRAPHENE ALLOTROPES

3.1 Test Models and Preliminary Surveys

In this chapter, the computational details of the performed calculations are presented, which are important for the results of the following chapters. Since graphene is the principal material with a two dimensional hexagonal structure, it is used as an example to obtain a detailed understanding of computational procedures and allow a comparison with previous theoretical studies to check the correctness of our calculation method.

3.1.1 Convergence Test for the Graphene Structure

Before any calculations, such as geometry optimization, electronic properties, etc., can start, it is recommended to check the convergence of the system by calculating the total energy versus both cut-off energy and the number of the momentum k-points for the plane wave expansion of the wave function. Various cut-off energies have been tested, and 600 eV has been found to be appropriate. The cut-off energies that are higher than 600 eV offer minimum energies lower than that given by 600 eV, however, the energy differences are less than 5 meV and do not influence the

precision of the results. In order to reduce the computational cost, we chose 600 eV as the cut-off energy for calculations.

The k-points are a set based on the Monkhorst Pack Scheme.[117] A $16 \times 16 \times 1$ mesh was employed, since it offers good convergence at a reasonable computational cost. Periodic density functional theory (DFT) as implemented in the Vienna *ab initio* simulation package (VASP)[118] has been used in all the calculations. The exchange correlation potential in this work is the generalized gradient approximation (GGA) with projected augmented wave (PAW) pseudopotentials.[108] All the atomic positions were fully relaxed until the atomic forces dropped below 1 kbar, while convergence of the electronic structures has been ensured by forcing the energy difference in the self-consistent cycle to be below 10^{-5} eV. In order to compute energy barriers, partial occupancy of one-particle states has been allowed with a 0.01 eV wide Gaussian smearing. To ensure no reciprocal interaction between periodic images, a 20 Å vacuum has been adopted along the *c* axis.

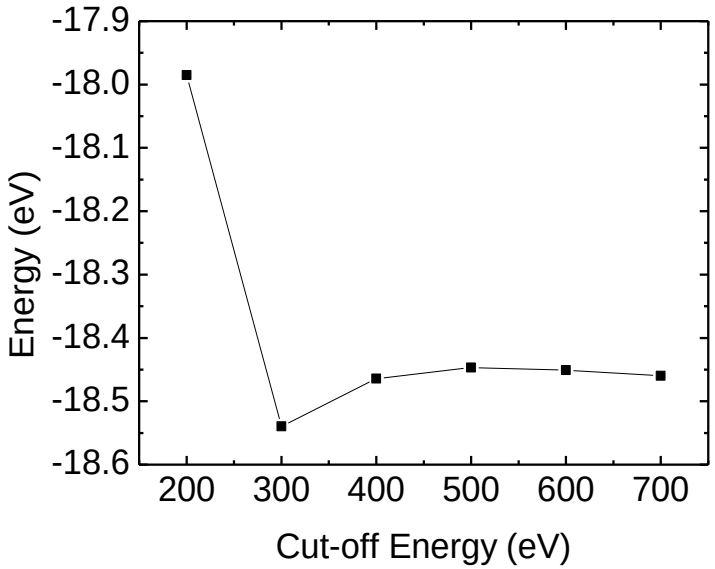

Figure 3.1 Convergence of the total energy of graphene as a function of the cut-off energy.

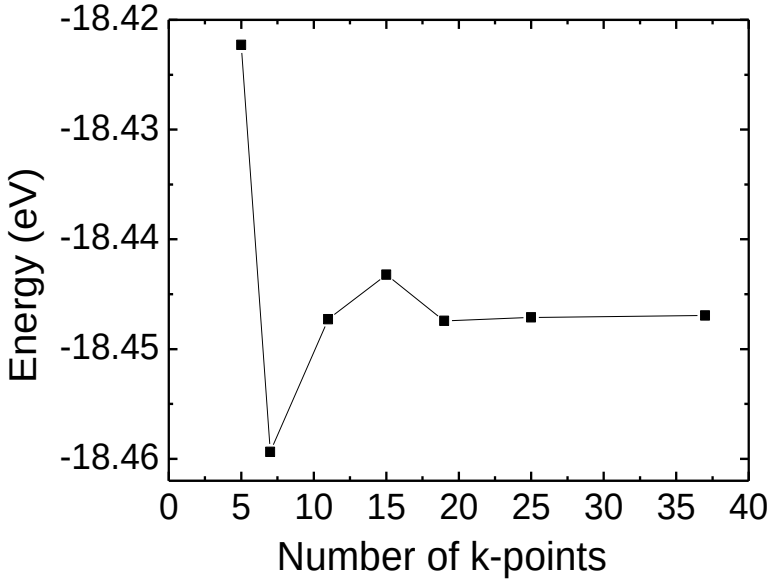

Figure 3.2 Convergence of the total energy of graphene as a function of the number of k-points.

3.1.2 Structural Properties of Graphene

When calculating the properties of materials, it is crucial to guarantee that the system is in equilibrium. One way to find the equilibrium state is to minimize the energy and calculate the equilibrium parameters of the system corresponding to the minimum energy. We regulate the lattice constant according to the direction of the atomic pressure. If the pressure is positive, the system is required to be expanded, while if the pressure is negative, the system has to be shrunken. When the absolute value of the pressure is reduced below 1kbar, the system can be considered as in an equilibrium state and chosen for further studies. In Figure 3.3, the absolute pressure under 1 kbar is 0.55 kbar, corresponding to the lattice constant of 2.47 Å. The minimum energy point in Figure 3.4, which indicates the equilibrium state, also corresponds to the same lattice constant.

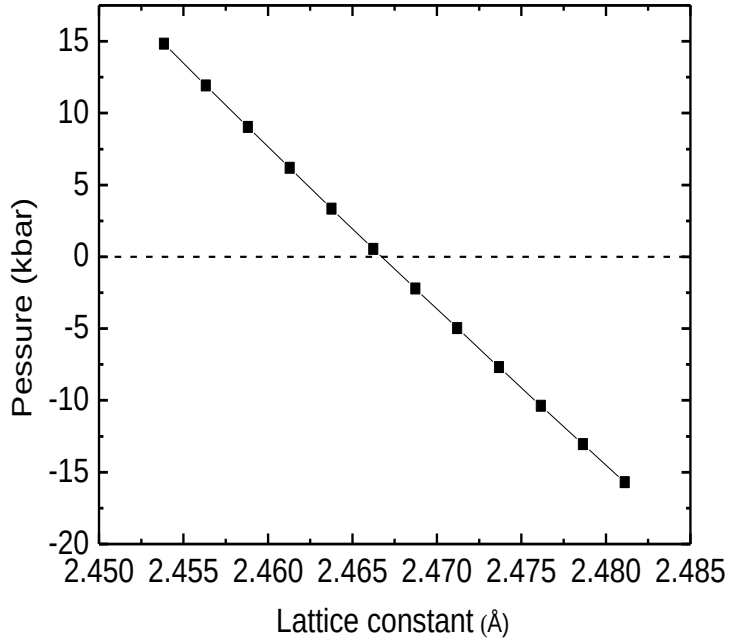

Figure 3.3 Atomic pressure versus lattice constant of graphene.

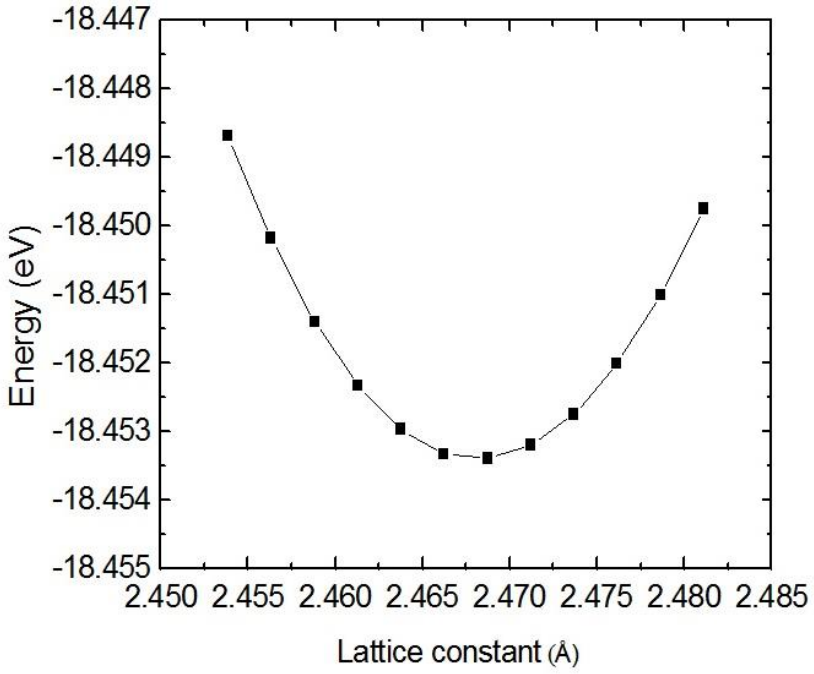

Figure 3.4 The total energy versus lattice constant of graphene.

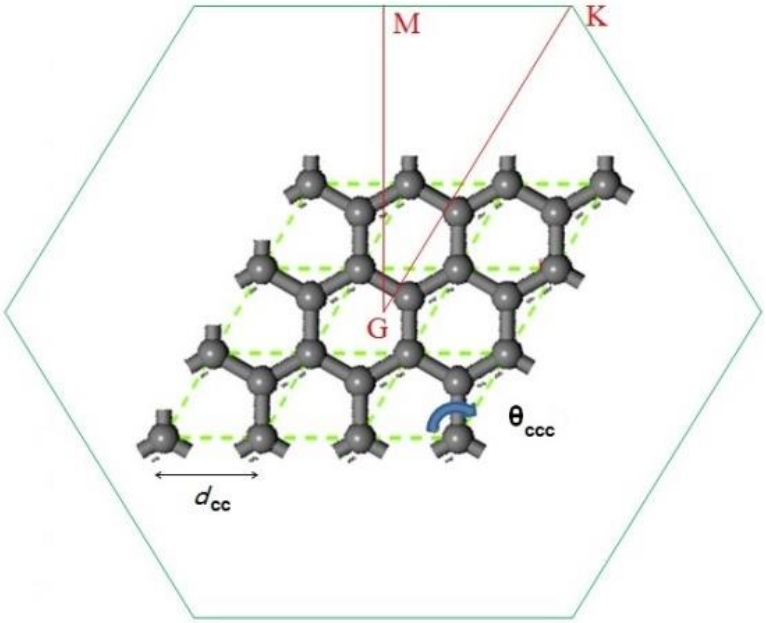

Figure 3.5 (3 × 3) unit cells of two-dimensional graphene structure in the Brillouin zone. G, M, and K are high symmetry points for band-structure calculations in the hexagonal configuration.

Table 3.1 Calculated parameters for graphene, including the lattice constant $|a|$, C-C bond distance (d_{CC}), bond angle (θ_{CCC}), and cohesive energy per unit cell (E_{coh}).

Graphene	$\|a\|$ (Å)	d_{CC} (Å)	ϑ_{CCC} (°)	E_{coh} (eV)
1 × 1	2.47	1.42	120	-15.93
2 × 2	4.94	1.42	120	-63.72
3 × 3	7.41	1.42	120	-143.99

We investigated the structural and electronic properties of 1×1, 2×2, and 3×3 unit cells after fully relaxing the system. It was found that the results were in agreement with previous calculations.[3] As shown in Figure 3.5, graphene is characterized as a one atom-thick honeycomb sheet. The lattice constant of 1×1 graphene is 2.47 Å, and

the lattice constant of 2×2 and 3×3 graphene doubles and triples that value, respectively. The cohesive energy is expressed as $E_{coh} = E_{graphene} - \sum_a^N E_C$, by taking the energy difference between the equilibrium energy of the graphene structure and the energy of the independent carbon atoms. Upon the formation of the sp^2 bonded planar lattice, the covalent C-C bond length is 1.42 Å, and the bond angle between the C atoms is 120˚. Such an atomic structure is composed of two types of C–C bonds (σ, π) constructed from the four valence orbitals ($2s$, $2p_x$, $2p_y$, $2p_z$), where the z-direction is perpendicular to the sheet. Three σ-bonds attach a C atom to its three nearest neighbours. They are so strong that the optical-phonon frequencies are much higher than those observed in diamond.[17] Furthermore, the C–C bonding is enhanced by a fourth bond associated with the overlap of p_z (or π) orbitals.

3.1.3 Electronic Properties of Graphene

The electronic bands and states of graphene in 1×1, 2×2, and 3×3 unit cells along the high-symmetry G–M–K-G directions are shown in

Figure **3.6**. It can be observed that the band structure has no band gap, but also no overlap between the conduction and valence bands. The bottom of the conduction band and top of the valence band touch each other at the Fermi level at the K-point of the Brillouin zone, forming the Dirac cone. Consequently, graphene is a special semimetal or zero-gap semiconductor. It should be noted that the Dirac cone in the band structure of the 3×3 graphene is shifted to the G point. This is attributed to the folding of the graphene Brillouin zone (BZ) into the superlattice.[119] The folding of the graphene band structure occurs in different ways, according to whether the superlattice constant n belongs to the sequence $n = 3m\cdot a$ or $n = (3m + 1)\cdot a$ or $(3m +$

2)·a (where m is an integer and a is lattice constant of 1×1 graphene). For n = (3m + 1)·a or (3m + 2)·a, K folds into K_n, whereas for n = 3m·a, it folds to the BZ center G_n.

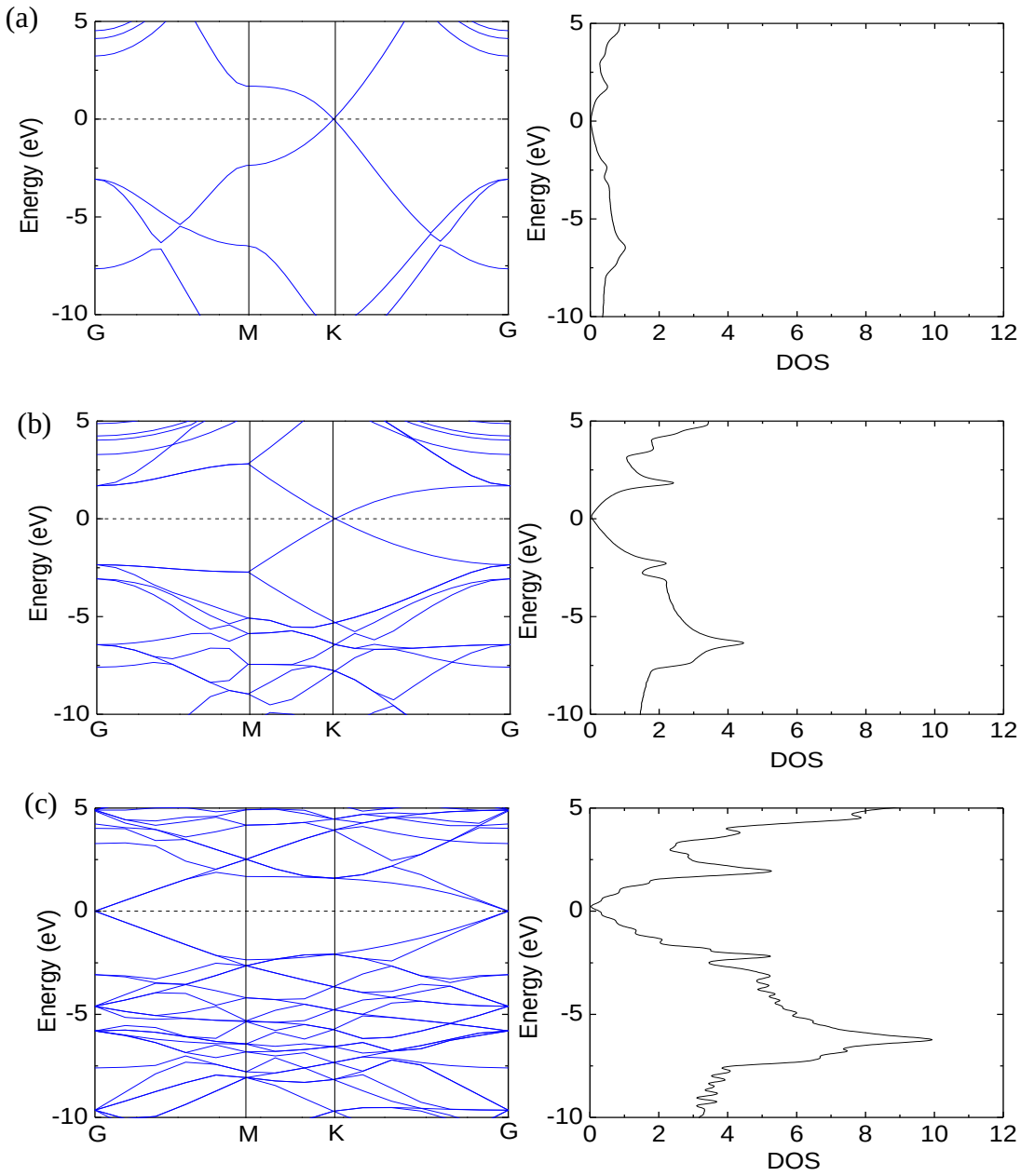

Figure 3.6 Band structures and electronic states of graphene in (a) 1×1, (b) 2×2, and (c) 3×3 unit cells.

According to cohesive energy given in Table 3.1, we can see that the cohesive energies of 2×2 and 3×3 graphene are four and nine times that of 1×1 graphene, respectively. This rule can also be applied to the density of states (DOS), as shown in Figure **3.6**. 2×2 graphene has a density of states which is four times that of the 1×1 graphene DOS, while for 3×3 graphene, the DOS is as nine times as great as that of 1×1 graphene.

3.2 Adsorption of Single Atoms on Graphene

The discovery of graphene[1] and its unusual electronic properties[14,15] has attracted great attention in the condensed matter physics community. The origin of the novel phenomena lies in the special band structure of graphene. From the theoretical analysis of graphene, it was demonstrated that the conduction and valence bands touch only at the two inequivalent corners of the hexagonal Brillouin zone (BZ), which are known as the Dirac points. The energy surfaces are in the shape of Dirac cones, and the energy dispersion in the neighbourhood of these points is linear. The meaning of this is that the charge carriers would behave like two-dimensional (2D) massless chiral Dirac fermions[3] and possess a variety of physical properties. Device engineers have also expressed interest in graphene, due to its high-carrier mobility and exceptional two-dimensional character.[120] The zero-gap spectrum makes graphene a semimetal, however, leading to a limitation for applications in logic circuits.

The electronic properties of graphene could be altered by the adsorption of some other atoms. It was reported that hydrogen functionalization may promote a metal–insulator transition in graphene[121] and open up a band gap in its electronic

spectrum.[122] Another significant feature, with respect to potential applications in spintronics, is the appearance of magnetism in graphene materials because of the interaction with hydrogen.[123] In the following section, we will discuss the effects of the adsorption of a single H, F, or O atom on the electronic and magnetic properties of graphene. To reduce the strain induced by the adatoms, the lattice parameters were optimized properly.

3.2.1 A Single Hydrogen Atom adsorbed on Graphene

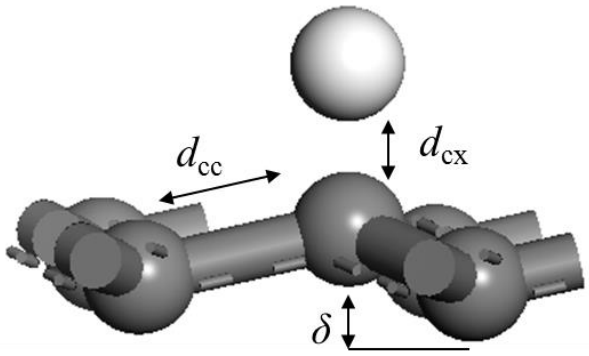

Figure 3.7 Optimized structure of the adsorption of a single H atom on graphene. The white ball stands for the hydrogen atom, and the black balls represent the carbon atoms.

For the study of a single H atom adsorbed on graphene, the system consists of periodically repeated super-cells containing one hydrogen adatom and an integral number of graphene unit cells. Generally, various properties depend on the scale of the super-cell. Therefore, four scales of graphene, including 1×1, 2×2, 3×3, and 4×4 unit cells, are considered in our study. The GGA-Perdew-Burke-Ernzerhof (PBE) exchange-correlation functional is applied to obtain a good description of the bond

lengths. Spin-polarized simulations are employed since the adatom contains unpaired electrons.

Table 3.2 Calculated parameters for graphene, including lattice constant (a), C-C bond distance (d_{CC}), C-H bond distance (d_{CH}), bond angle (θ_{CCC}), buckling (δ), band gap (E_{gap}), and total magnetic moment (M_{tot}).

	$\|a\|$ (Å)	d_{CC} (Å)	d_{CH} (Å)	ϑ_{CCC} (°)	δ (Å)	E_{gap} (eV)	M_{tot} (μ_B)
(1×1)	2.53	1.50	1.16	115.5	0.32	0.71	1
(2×2)	4.97	1.50	1.13	115.4	0.33	0.56	1
(3×3)	7.41	1.50	1.13	114.9	0.34	0.36	1
(4×4)	9.88	1.50	1.13	114.8	0.35	0.30	1

Since it has been proved that the favorable position for hydrogen adsorbed on graphene is on top of a carbon atom[124-127], we simply used this position in our calculations. The optimized structure is shown in Figure 3.7, and the calculated parameters are listed in Table 3.2. We found that hydrogen on top of a C atom causes the C atom to move out of plane and form an H-C bond to accommodate the re-hybridized bond. This structural transformation changes the lattice constants, bond lengths, and angles. For all cell sizes, the bond lengths between the bonding carbon and its first neighbours are elongated to 1.50 Å, in comparison with the bond length in graphene (1.42 Å). For small cells, the lattice constant is a little larger than that of graphene in the same size unit cell, which arises from the elongated C-C bond lengths close to the adatom site. As the size of the unit cell increases, however, this difference

could be neglected. Meanwhile, the H–C bond is fixed at 1.13 Å, and the buckling is enlarged from 0.31 to 0.35 Å, demonstrating the change towards sp^3 hybridization. The bond angles θ_{CCC} cannot form perfect tetrahedral angles of 109.5°, which means a mixed character between the sp^2 and sp^3 hybridization. From the different parameters obtained from various super-cells, we could conclude that the H-graphene adsorption properties strongly depend upon the super-cell size.

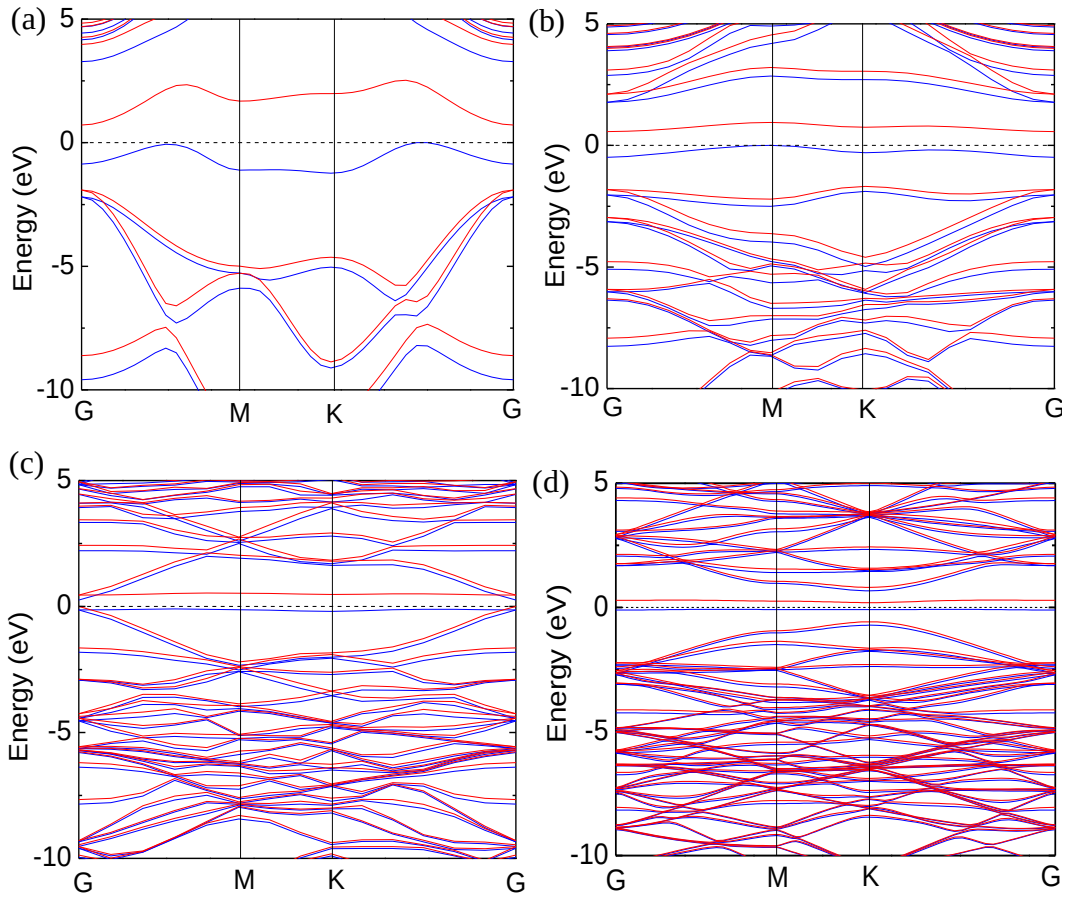

Figure 3.8 Band structures of hydrogenated graphene shown for (a) 1 × 1, (b) 2 × 2, (c) 3 × 3, and (d) 4 × 4 structures.

Such a conclusion can also be adapted to band structures for the above four systems. All the band structures calculated by using spin-polarized DFT are shown in

Figure 3.8. It was found that a band gap opened up in each band structure, and there were a pair of spin-polarized mid-gap bands in the vicinity of the Fermi level. Increasing the size of the superlattice makes the mid-gap bands become flatter, leading to a smaller band gap. From the corresponding density of states of the 4×4 supercell, we can see that the mid-gap bands mainly originate from the hydrogen states. It can be understood that with the reduced concentration of hydrogen, the distance between each pair of neighbouring hydrogen atoms becomes large enough to weaken the interactions between the two adatoms. Without the effect of the neighbouring hydrogen atoms, the energies of each hydrogen atom seem equivalent for all k points.

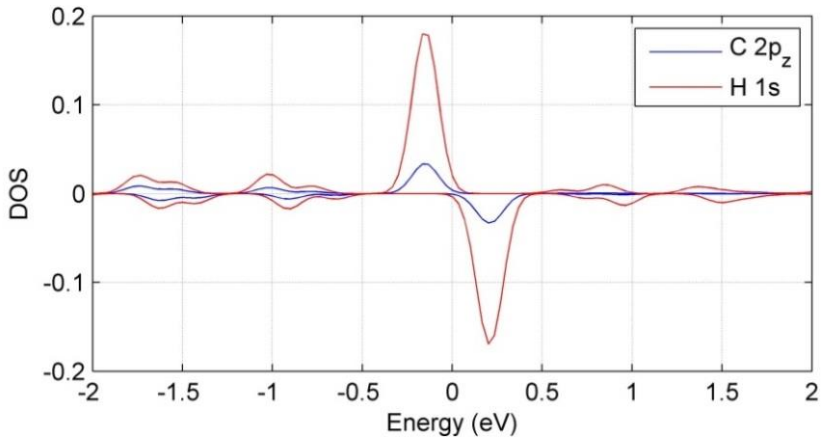

Figure 3.9 Spin-polarized projected density of states per atom for 4×4 hydrogenated graphene, with spin-up and spin-down parts shown in the upper and lower halves of the plot, respectively.

The magnetic properties of the above four structures indicate a magnetic moment of 1 μ_B per unit cell, as given in Table 3.2. The projected density of states corresponding to the band structure of 4×4 hydrogenated graphene in Figure 3.9 also

reveals a net magnetic moment. The density of states in the vicinity of the Fermi level is dominated by H-1*s* states, combined with the contribution from C-2p_z states. The H-1*s* spin up states are localized in the valence bands, whereas the spin down states are empty and situated in the conduction bands.

To understand the mechanism, it is worthwhile to recall the basic electronic structure of graphene. In graphene, each carbon atom has three σ (2*s*, 2p_x, 2p_y) orbitals situated in the graphene plane with an angle between them of 120° and one π (2p_z) orbital along the *c*-axis in the perpendicular direction. Every carbon atom is bonded with three other carbon atoms through the σ orbitals via sp^2 hybridization. Consequently, the electron in the π orbital can be treated independently from the other valence electrons, creating a magnetic moment of 1 μ_B for each carbon atom. In a primitive cell of graphene, the spins of the two π orbital electrons are antiparallel to each other, resulting in a non-magnetic primitive cell. When the H atom forms an H-C covalent bond with one of the carbon atoms, the other carbon atom will create a net magnetic moment of 1 μ_B for the primitive cell and even the entire graphene lattice.

3.2.2 Adsorption of Single Fluorine and Oxygen Atoms on Graphene

The adsorption of F and O atoms on graphene was also studied. To reduce the interaction between the adjacent adatoms and save on computational cost, the single F or O atom is adsorbed on 4 × 4 graphene. The electronic and magnetic properties are different from those revealed for H adsorption. As each C atom in graphene is able to offer one electron to form an extra chemical bond, the adsorption site of the radicals

depends roughly on the number of ‘missing’ electrons. A fluorine atom, like an H atom, lacks one electron and is able to bond to a single C on the top site (Figure 3.10), while an oxygen atom demands two more electrons, so that it bonds with two C atoms by adsorption on the bridge site (Figure 3.11).

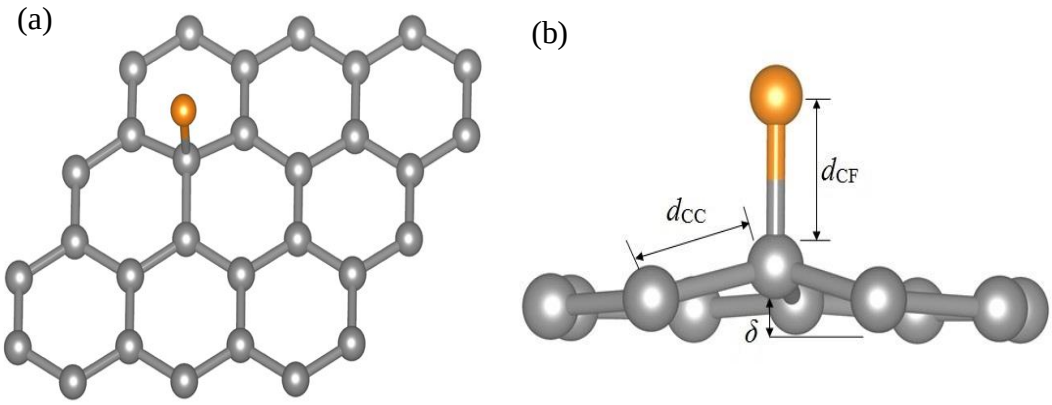

Figure 3.10 Optimized structure of F-graphene from (a) top view and (b) side view. The grey circles and the orange one represent the C atoms and the F atom, respectively.

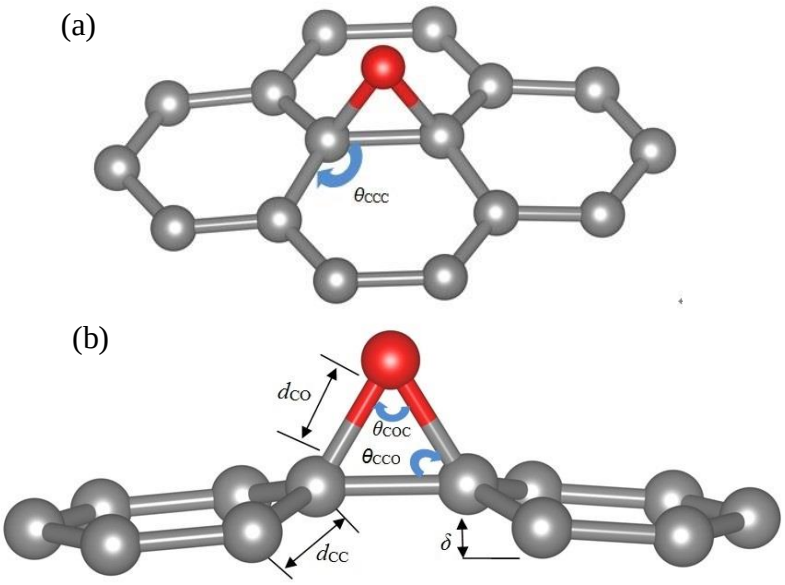

Figure 3.11 Optimized structure of O-graphene from (a) top view and (b) side view. The grey circles and the red one represent the C atoms and the O atom, respectively.

Table 3.3 Calculated parameters for H, F, and O adsorption on 4×4 graphene, including the lattice constant (a), C-C bond distance (d_{CC}), C-X bond distance (d_{CX}), bond angle (θ_{CCC}, θ_{CCX}, θ_{CXC}), buckling (δ), binding energy per unit cell (E_{bind}), band gap (E_{gap}) and total magnetic moment (M_{tot}). X stands for the adatom.

X-graphene	a (Å)	d_{CC} (Å)	d_{CX} (Å)	ϑ_{CCC} (°)	ϑ_{CCX} (°)	ϑ_{CXC} (°)	δ (Å)	E_{bind} (eV)	M_{tot} (μ_B)
H-graphene	9.88	1.41	1.13	114.8	103.5	44.7	0.35	-0.75	1.0
F-graphene	9.87	1.48	1.57	115.6	102.3	37.5	0.31	-1.89	0
O-graphene	9.88	1.47	1.47	118.2	59.0	62.0	0.27	-2.36	0

Now, we concentrate on the bond lengths between the adatoms and the carbon atom that takes part in the chemical bond formation. For F on graphene and O on graphene, both the C-F bond length (1.57 Å) and the C-O bond length (1.47 Å) are relatively larger, when compared to the C-H bond length (1.13 Å) in H on graphene. The lengths of the C-C bonds closest to the adatoms are intermediate between sp^2-bonds (1.42 Å) and sp^3-bonds (1.55 Å). The bond angles θ_{CCC} with respect to C atoms below the adatoms are also between the bond angles of the two hybridizations. This indicates a hybridization state between sp^2 and sp^3.

We define the binding energy as $E_B = E_{system} - (E_{graphene} + E_{adatom})$. For the adsorption of an F (O) atom on graphene, the bond between F (O) and the graphene lattice is stronger, with a binding energy of −1.89 eV (−2.36) eV, compared with the binding energy of H on graphene. This is because F and O atoms have higher electronegativity than H atoms. This feature also leads to different magnetic moments and electronic properties in the three systems, as shown in Table 3.3. H on graphene has a magnetic moment of 1 μ_B, whereas F or O on graphene has M_{tot}= 0 μ_B. The band

structures in Figure 3.12 demonstrate that F – graphene is metallic and O – graphene is a semiconductor with a direct gap of 0.5 eV.

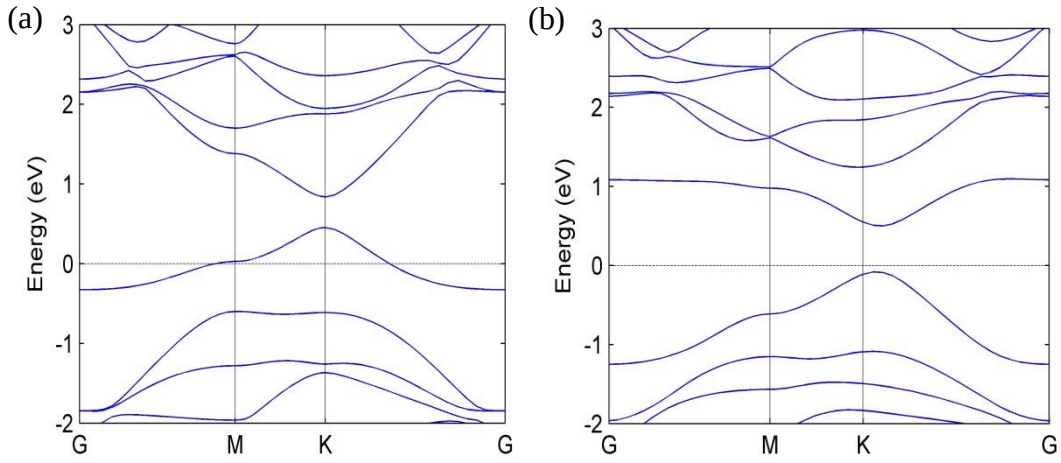

Figure 3.12 Band structures of a single fluorine atom (a) and a single oxygen atom (b) adsorbed on graphene.

3.3 Graphene Allotropes

In the natural world, there exist many graphene allotropes such as graphite, diamond, and carbon black. Continuous efforts are ongoing towards the synthesis and discovery of new carbon allotropes with highly various functionalities and a wide range of applications. The most outstanding and well known achievements are the discoveries of fullerenes,[128] nanotubes,[129] carbyne,[130] and carbolite.[131] Meanwhile, the versatile flexibility of carbon in possessing three competing hybridization states (*sp*, sp^2, and sp^3) allows one to design numerous combinations in which atoms of this element can be bonded to each other to generate many carbon allotropes. Three typical compounds representing interesting families of graphene allotropes are called octagraphene, graphyne, and graphdiyne.

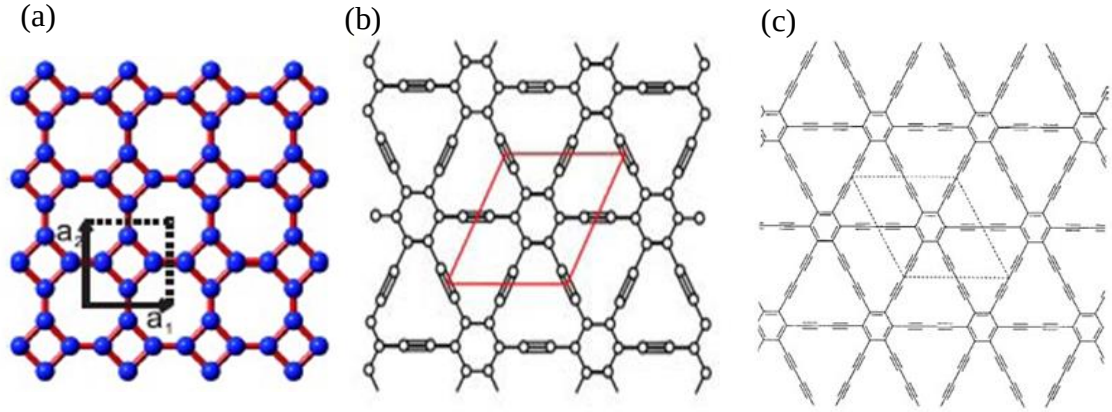

Figure 3.13 Schematic representation of the structures of (a) octagraphene,[134] where a unit cell is indicated with the unit vectors a_1 and a_2; (b) graphyne,[132] where the red quadrangle indicates the unit cell; (c) graphdiyne .[133] The parallelogram drawn with a dotted line represents a unit cell.

Octagraphene [134] is a kind of 2D periodic atomic sheet consisting of carbon octagons, which possesses intriguing properties and might be produced experimentally by methods involving acetylene scaffolding or line defects. As shown in Figure 3.13(a), octagraphene consists of carbon squares and octagons with two bond lengths, forming a square lattice with C_{4v} symmetry. Graphyne was predicted by Baughman, Eckhardt, and Kertesz.[135] This material comprises layered carbon sheets involving *sp* and sp^2 carbon atoms, as shown in Figure 3.13(b). The name ‘‘graphyne’’ originates from its structure, as the layers can be constructed by substituting one-third of the carbon-carbon bonds in graphene with acetylenic linkages $(-C \equiv C-)$. Graphdiyne is another graphene allotrope composed of *sp* and sp^2 carbon atoms, as well as containing two acetylenic (diacetylenic) linkages between carbon hexagons. The structure is shown in Figure 3.13(c). The name ‘‘graphdiyne’’ is derived from the name graphyne. In this section, the structural and electronic properties of the above

three materials will be analysed by first-principles calculations as a preparation for further study.

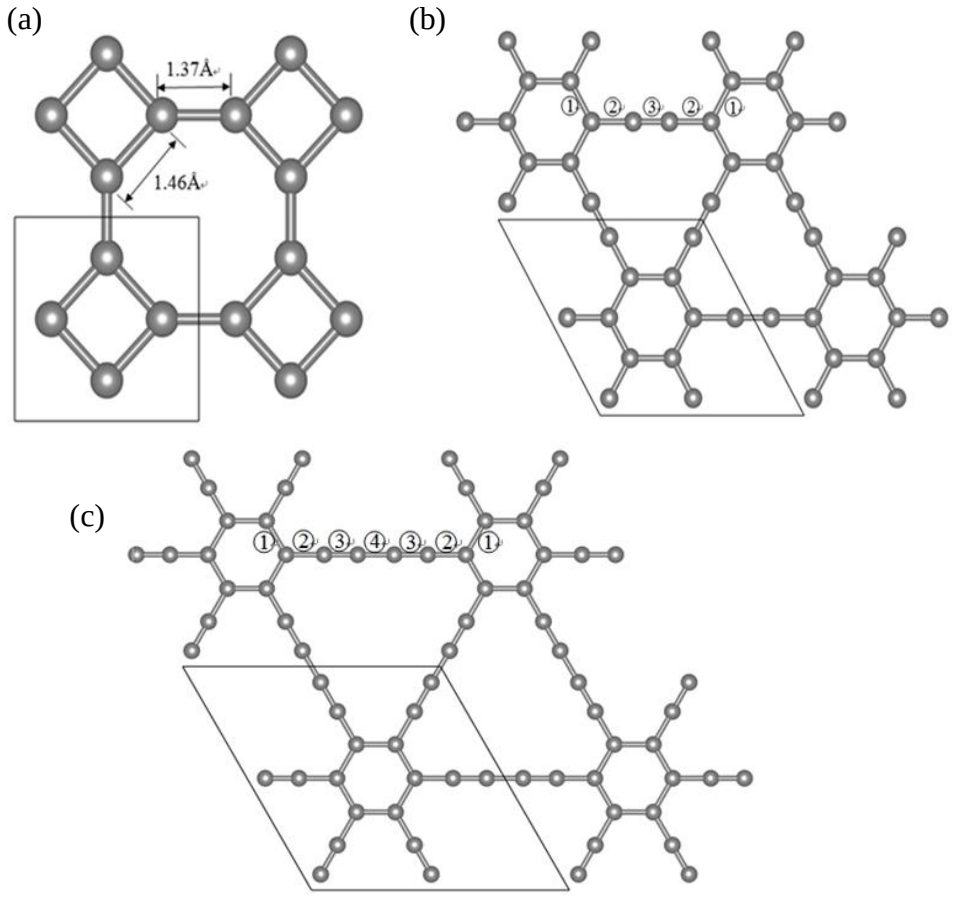

Figure 3.14 Optimized (a) octagraphene, (b) graphyne, and (c) graphdiyne structures. The parallelograms drawn with a grey line represent unit cells.

For geometrical optimization, we chose to use 17 k-points for octagraphene and 11 k- points for graphyne and graphdiyne in the Brillouin zone after k-point testing. The plane-wave cut-off energy is taken as 400 eV. For the first-principles calculation, primary calculations were performed within the Vienna *ab initio* simulation package (VASP) with the projector augmented wave (PAW) method. The generalized gradient approximation (GGA) was adopted for the exchange correlation potentials. The super-

cells are used for calculations of isolated sheet structures, and the distance between two layers is about 15 Å to avoid interactions. The geometries were optimized when the atomic forces on the ions were less than 1kbar. Thus, the band calculation was performed using the obtained self-consistent potential with the optimized geometry.

Our optimized geometric structures of octagraphene, graphyne, and graphydiyne shown in Figure 3.14 are consistent with previous studies with similar lattice parameters, as listed in Table 3.4. Carbon atoms in octagraphene are in the same plane and make up a square lattice with lattice constant a = 3.45 Å, where a unit cell contains four carbon atoms. Analogous to graphene, every carbon atom in octagraphene connects with three nearest neighbours, forming three σ bonds with sp^2 hybridization. In addition, octagraphene has two types of bond lengths. The intra-square bond length is 0.09 Å larger than that for inter-squares. The bond angles of intra-squares and inter-squares are 90˚ and 135˚, respectively.

Table 3.4 The lattice parameters of octagraphene, graphyne, and graphdiyne in the unit cell, including the lattice constant $|a|$, bond lengths (d_{CC}), cohesive energy per atom (E_c /atom), and energy gap (E_g).

	$\|a\|$ (Å)	d_{CC} (Å)	E_c (eV)/atom	E_g (eV)
Octagraphene	3.43	1.46, 1.37	-7.44	0
Graphyne	6.88	①1.42, ②1.41, ③1.22	-7.33	0.48
Graphdiyne	9.44	①1.43, ②1.39, ③1.23, ④1.34	-7.21	0.51

The optimized graphyne and graphydiyne also possess a hexagonal lattice, with lattice constant of 6.88 Å and 9.44 Å, respectively. In the unit cell of graphyne and

graphdiyne, there are 12 and 18 carbon atoms, respectively. The C-C bond length strongly depends on the hybridized carbon atoms. Graphyne has three different C-C bonds ①, ②, ③, which are 1.42 Å, 1.41 Å, and 1.22 Å. The type of the ① bonds in the hexagons are likely to be C(sp^2)-C(sp^2), as seen in graphene (=1.42 Å) and the type of the ③ bonds can be considered to be C(sp)≡C(sp), as the bond length is nearly equal to the acetylenic bond length of 1.2 Å. The ② bond is not a typical single bond due to its short length but is considered to be of the C(sp^2)-C(sp) type, considering the neighboring triple bond. Two types of bond angles, 120˚ and 180˚, are involved in graphyne, demonstrating the hybridizations of sp^2 and sp that coexist in the material. Graphdiyne has one more type of bond. The ④ bond (= 1.34 Å) is larger than the ③ bond (= 1.23 Å) and smaller than the ② bond (= 1.39 Å). The ④ bond can be viewed as a single bond between two triple bonds [$\mathrm{C}(sp) \equiv \mathrm{C}(sp) - \mathrm{C}(sp) \equiv \mathrm{C}(sp)$], which is the same type of bond as seen in diacetylene. The ④ bonds are a little shorter, however, than the typical single bonds in diacetylene. This is because the single ④ bonds are influenced by the triple bonds situated between them and hence acquire the character of a double bond. Consequently, graphyne is composed of equilateral hexagons which are connected by carbon chains composed of acetylenic linkages ($-\mathrm{C} \equiv \mathrm{C} -$). The bond length in a hexagon is almost equal to that of graphene and a little longer than the bond length that extends outside a hexagon. All bond angles are either 120 ° or 180 °. In graphdiyne, the carbon chains between hexagons are made up of two acetylenic linkages ($-\mathrm{C} \equiv \mathrm{C} - \mathrm{C} \equiv \mathrm{C} -$).

The cohesive energies and the electronic properties of the three graphene allotropes seem to be affected by the types of structures and C-C bonds. The cohesive energies for all three materials are expected to be much less than for graphene. The

cohesive energy of octagraphene is larger than those for graphyne and graphdiyne, implying that octagraphene is more energetically stable than graphyne and graphdiyne but metastable against graphene. The electronic structures in Figure 3.15(a) show that octagraphene is a semimetal, as the Fermi level passes through both the conduction and valence bands. Figure 3.15(b) and (c) show that both graphyne and graphdiyne are semiconductors from their band structures. There is a direct gap of 0.48 eV at the M point for graphyne. The direct gap for graphdiyne is at the G point with the value of 0.51 eV. All these calculated results are consistent with previous studies.[133,134]

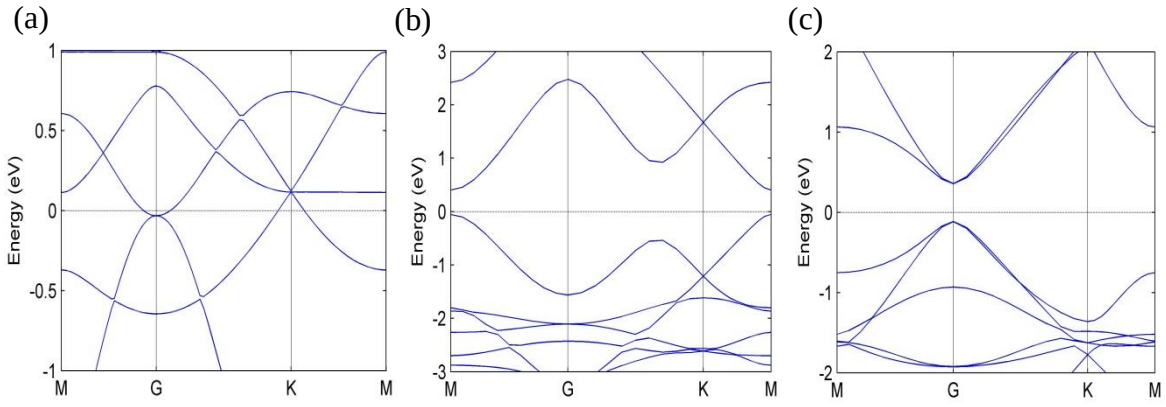

Figure 3.15 Band structures of (a) octagraphene, (b) graphyne, and (c) graphydiyne.

3.4 Conclusions

In this Chapter, for further studies on two-dimensional honeycomb structures like silicene and germanene, graphene has been taken as a test model to present the computational procedures and make comparisons with previous theoretical results to verify the feasibility of the calculation method. The functionalization of graphene was investigated to transform the metallic property of graphene. The structural and electric

properties of graphene allotropes were also discussed for later studies on silicene allotropes.

The geometry optimization and electronic structure calculations were conducted after cut-off energy and *k*-point testing. 1×1, 2×2, and 3×3 unit cells were used to investigate the structural and electronic properties of graphene. The atomic structure of graphene is a sp^2 bonded planar lattice. The covalent bond length of C-C is 1.42 Å, and the bond angle between the C atoms is 120˚. Each C atom is attached to its three nearest neighbours through σ-bonds. In addition, the C–C bonding is enhanced by a fourth π bond. The band structure indicates that graphene is a semimetal with a Dirac cone at the K-point.

The adsorption of single H, F, and O atoms on graphene was investigated. The favourable adsorption position for a hydrogen atom on graphene is on top of a carbon atom. Four scales of graphene, including 1×1, 2×2, 3×3, and 4×4 unit cells, were considered for the adsorption study of a single H atom on graphene. Different super-cells result in different structural parameters. The reduced concentration of hydrogen on the super-cell could avoid interactions between the adatoms. After full optimization, the C atom adsorbed by an H atom was pulled out of the plane and experienced a transition towards sp^3 hybridization. The H adatom created a magnetic moment of 1 μ_B for graphene, resulting in a spin-polarized electronic structure. The adsorption sites of single F and O adatoms on graphene are the top site and bridge site, respectively. The adsorption of a single F atom on graphene was found to result in a metallic and non-magnetic system. The electronic and magnetic properties demonstrated that the system with an O adatom on graphene is a semiconductor without any contribution of magnetic moment.

The electronic properties of three typical graphene allotropes, octagraphene, graphyne and graphdiyne, were investigated. Octagraphene consists of carbon squares and octagons with two bond lengths, forming a square lattice with C_{4v} symmetry. Both graphyne and graphdiyne are composed of *sp* and sp^2 bonded carbon atoms. Graphyne is constructed by substituting one-third of the carbon-carbon bonds in graphene with acetylenic linkages ($-C \equiv C-$), while graphdiyne contains two acetylenic (diacetylenic) linkages ($-C \equiv C-C \equiv C-$) between carbon hexagons. The electronic structures show that octagraphene is a semimetal. Graphyne and graphdiyne are semiconductors with a direct gap at the M point and G point, respectively.

CHAPTER 4. FUNCTIONALIZATION OF SILICENE ALLOTROPES

4.1 Introduction

Since the first reports on the successful isolation of a stabilizing single layer of graphene,[1,3] particular efforts have been devoted to prospecting for similar materials with new features attributable to their ultrathin two-dimensional nature. The monolayer honeycomb structure of silicon, silicene, has appeared as a potential one-atom-thick material that might displace graphene.

As was reported in previous theoretical studies,[30,31] silicene is a semimetal with linearly crossing bands and a zero electronic band gap analogous to that of graphene. Moreover, electrons propagating through the monolayer silicene are projected to display massless fermion behaviour in the vicinity of the Dirac point. One of the biggest challenges in silicene is to manipulate its electronic conduction by opening an energy gap at the Dirac point. Under the inspiration of the graphene allotropes, as was discussed in the last chapter, it is possible to change the electronic properties of silicene by inserting the silicon triple bonds ($-\mathrm{Si} \equiv \mathrm{Si}-$) between the two hexagons in silicene. Therefore, new types of silicene allotropes, silicyne and silicdiyne, could be constituted. The name "silicyne" is based on that of graphyne, due to its similar structure to graphyne, with the linkage ($-\mathrm{Si} \equiv \mathrm{Si}-$) between the two hexagons. The name "silicdiyne" originates from graphdiyne, as silicdiyne contains the linkage ($-\mathrm{Si} \equiv \mathrm{Si} - \mathrm{Si} \equiv \mathrm{Si}-$) between two hexagons.

In this Chapter, the structural and electronic properties of several silicene alltropes will be investigated. Besides silicyne and silicdiyne, octasilicene, which has a similar structure to octagraphene, is also included in the study. Unlike the planar configurations of graphene allotropes, buckling must be considered in the silicene alltrope structure. We can expect some novel properties due to this buckled structure.

4.2 Computational Methodology

We investigated the physical properties of silicene and its allotropes by employing density functional theory (DFT) as implemented in the VASP package.[118] We have made use of the generalized gradient approximation (GGA) with the Perdew-Burke-Ernzerhof (PBE) functional for the exchange-correlation functional.[108] The plane-wave basis is set with an energy cut-off of 500 eV, and the convergence criterion for energy is selected as 10^{-5} eV. The sampling of the Brillouin zone for the supercell used the equivalent Monkhorst-Pack $17 \times 17 \times 1$ k-point grid for the silicene unit cell (containing two silicon atoms) and the octasilicene unit cell (containing four silicon atoms). For the silicyne (with 12 silicon atoms) and silicdiyne (with 18 silicon atoms) unit cells, a $13 \times 13 \times 1$ k-point sampling was employed. For the purpose of calculating the density of states, a Gaussian smearing of the energy levels was set with standard deviation to 0.1 eV. To eliminate the interaction arising from periodic boundary conditions along the *c* axis, the height of 15 Å was used to include sufficient vacuum. The relaxation of the atomic positions was performed with forces smaller than 1 kbar.

4.3 Silicene

The lattice constants, bond lengths, bond angles, and buckling heights of silicene are summarized in Table 4.1, and are in good accordance with those found in previous calculations. In contrast to the completely flat one-atom thick surface of graphene, silicene is buckled, as can be seen in Figure 4.1(a). Because the π bonds between silicon atoms are weaker than in the case of the carbon atoms, the planarity is destabilized, and hence, silicon atoms are buckled in a silicene crystal.[136] For the sp^3 bonded honeycomb lattice, the covalent bond length of Si-Si is 2.27 Å. The cohesive energy of silicene per unit cell relative to free Si atoms is obtained from $E_{coh} = E_{silicene} - 2E_{Si}$, where E_{silicene} is the total energy of silicene in the primitive cell and E_{Si} is the total energy of a single free Si atom. The cohesive energy of silicene turns out to be -7.92 eV, indicating that silicene is thermodynamically less stable than graphene.

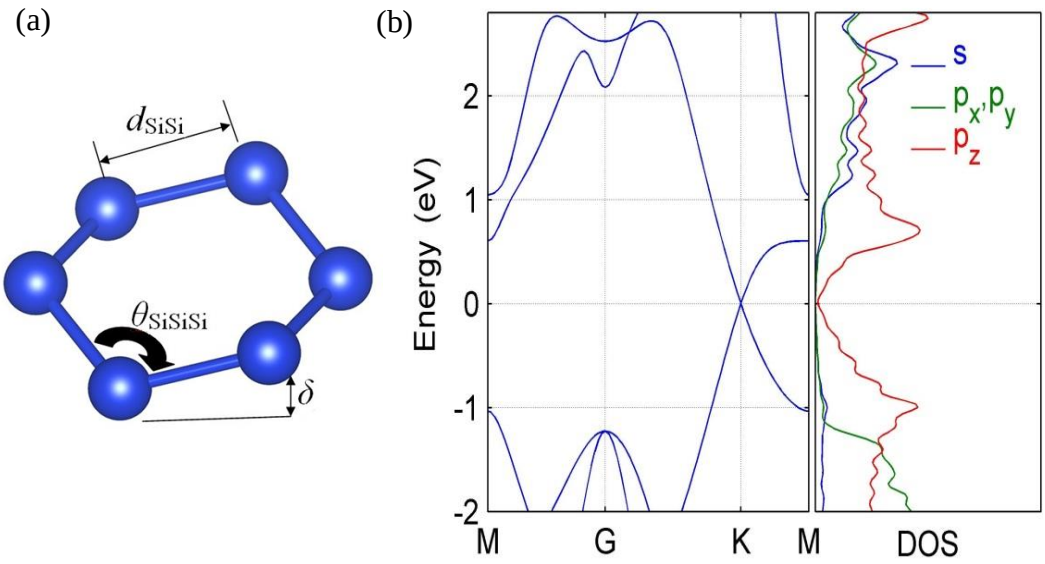

Figure 4.1 (a) Structural parameters for silicene. (b) Band structure and density of states for perfect silicene.

Table 4.1 Calculated parameters for 1×1 silicene, including the lattice constant $|a|$, Si-Si bond length ($d_{\text{Si-Si}}$), bond angle (θ_{SiSiSi}), buckling (δ), and cohesive energy per atom (E_{coh}/atom).

$\lvert a\rvert$ (Å)	$d_{\text{Si-Si}}$ (Å)	θ_{SiSiSi} (˚)	δ (Å)	E_{coh} (eV)/atom
3.87	2.27	116.2	0.45	-3.96

Similar to graphene, silicene is a semimetal with linearly crossing bands at the Fermi level and a zero electronic band gap, as can be seen in the electronic band structure of perfect silicene in Fig. 4.1(b). Since the valence band (VB) maxima and the conduction band (CB) minima degenerate at the K symmetry, the corresponding states have the same ionization potential and electron affinity. Linear π and π^* bands that cross at the K symmetry point are responsible for the existence of massless Dirac fermions in silicene. The charge carriers in silicene behave like relativistic particles, with a conical energy spectrum with Fermi velocity $V_F \cong 10^6$ m s^{-1} as in graphene.[137]

4.4 Silicene Allotropes

4.4.1 Octasilicene

To obtain the structural parameters of octasilicene, three types of possible structures are considered. In the type 1 structure, as in Figure 4.2, the four silicon atoms (*a*, *b*, *c*, *d*) in the octasilicene unit cell are in the plane. The buckling is considered for the type 2 and type 3 structures. In the type 2 structure, the *a* and *c* atoms are in the same plane and higher than the *b* and *d* atoms which are in another

plane. For the type 3 structure, the *a* and *b* atoms in the one plane are higher than the *c* and *d* atoms in another plane along the *c* axis.

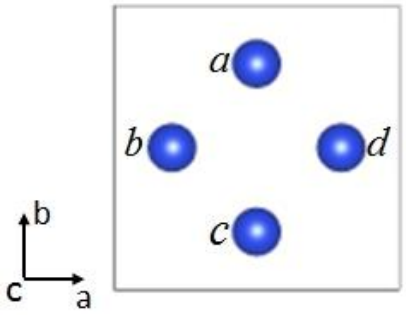

Figure 4.2 The octasilicene unit cell in the *ab* plane. The blue balls (*a*, *b*, *c*, *d*) represent the four silicon atoms in the octasilicene unit cell.

After full optimization, the type 3 structure with relatively low buckling is the most energetically favourable, compared with the type 1 and type 2 structures. As with silicene, the two-dimensional highly buckled or planar silicon materials cannot be stabilized. Therefore, our study is mainly focused on the type 3 structure. The cohesive energy is defined as $E_{coh} = E_{total} - n_{Si}E_{Si}$.

Table 4.2 Calculated parameters for 1 × 1 octasilicene, including lattice constant |*a*|, buckling (δ), total energy (E), and cohesive energy (E_{coh}).

Structure	|*a*| (Å)	δ (Å)	E (eV)	E_{coh} (eV)
Type1	5.44	0.00	-18.25	-14.94
Type2	4.60	1.83	-17.25	-13.94
Type3	5.41	0.50	-18.32	-15.01

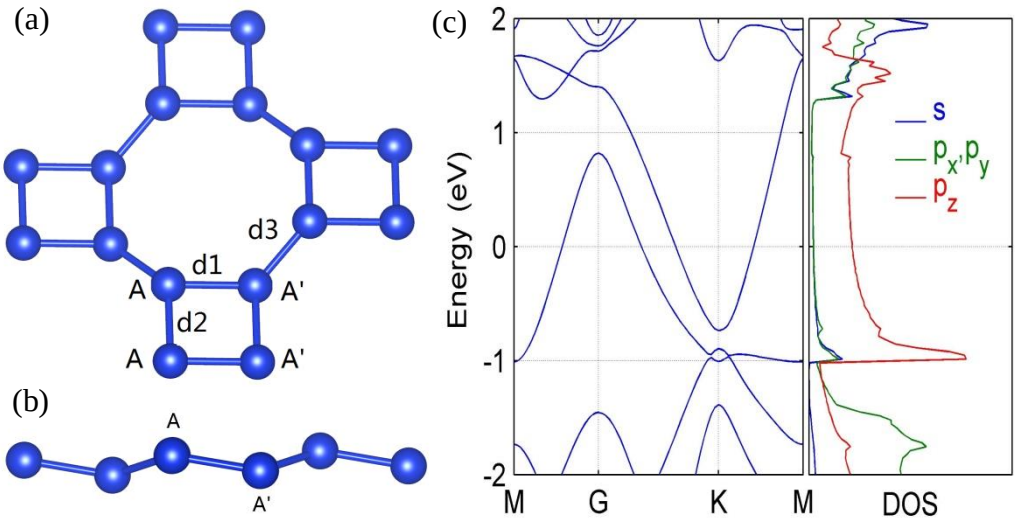

Figure 4.3 Optimized structure of octasilicene seen from (a) the top view and (b) the side view. The structure is composed of two types of silicon atoms, A and A′. (c) The band structure and PDOS of octasilicene.

The optimized type 3 octasilicene structure is presented in Figure 4.3. Similar to octagraphene, octasilicene comprises silicon octagons and squares. Silicon atoms in the octasilicene unit cell form a square lattice with the lattice constant 5.41 Å. Two types of silicon atoms, Si_A and $Si_{A'}$, can be distinguished, as they belong to different planes along the *c* axis. There are two types of bond length in the square lattice. The bond (d1) with length 2.31 Å between Si_A and $Si_{A'}$ atoms in the different planes can be considered as a single bond. For the two silicon atoms in the same plane, the bond length (d2) between them is 2.27 Å, displaying sp^2-sp^3 character. Like octagraphene, the four bond angles in the square lattice are all 90˚. However, the octagonal lattice has two types of bond angles 133.84˚ and 129.78˚, distinct from the 135˚ in octagraphene, due to the buckled structure. In addition, bond lengths between the squares (d3) are 2.25 Å. The inter-square bond length is smaller than the intra-square, which indicates a double bond character. Each silicon atom uses its three sp^3 hybrid

orbitals to form σ bonds with three atoms. The un-hybridized atomic p_z orbitals, which lie perpendicular to the plane created by the axes of the three sp^3 hybrid orbitals, combine to form the π bond.

The electronic structure of octasilicene in Figure 4.3(c) looks similar to that of octagraphene. The top of the valence band above the Fermi level and the bottom of the conduction band below the Fermi level make octasilicene a semimetal. The projected partial density of states (PDOS) of octasilicene shows that the energy bands near the Fermi surface are predominantly contributed by the p_z orbital, forming the π-bond.

4.4.1.1 Hydrogenated Octasilicene

Because octasilicene is a semimetal, an attempt was made to open the gap in the energy band structure by the adsorption of H atoms on both sides of octasilicene. As each silicon atom in silicene is able to provide one electron to form an extra chemical bond, each silicon atom in the hydrogenated octasilicene is bonded with one hydrogen atom on the top site, as shown in the optimized structure in Figure 4.4. The optimized structure parameters are summarized in Table 4.3.

The lattice constant of the 1×1 unit cell shrinks to 5.24 Å. The H atom pulls the bonded Si atom out of the plane, making the buckling between Si_A and $Si_{A'}$ even larger. The Si-H bond length is fixed at 1.50 Å. The adsorption position of the H atom, however, can greatly affect the Si-Si bond length. For example, the length of the Si_A-Si_A bond (2.4 Å) is larger than the Si_A-$Si_{A'}$ (2.36 Å) in the square lattice, although the atoms Si_A and $Si_{A'}$ are not in the same plane. This is because the two H atoms adsorbed on the neighbouring Si_A atoms are on the same side plane. They repel each

other due to the Coulomb effect, resulting in an elongated Si_A-Si_A bond. According to the bond lengths, all the Si-Si bonds are likely to be single bonds. The bond angles in the square lattice remain 90˚, while the bond angles in the octagonal lattice are reduced to 113.5˚ and 124.0˚. The formation energy, defined as $E_{formation} = E_{total} - E_{octasilicene} - n_H E_H$ for hydrogenated octasilicene is found to be -11.61 eV.

Table 4.3 Structural parameters of hydrogenated octasilicene: lattice constant $|a|$, bond lengths ($d_{Si\text{-}H}$, $d_{Si\text{-}Si}$), buckling ($\delta_{A\text{-}A'}$), and formation energy (E_f).

$\|a\|$ (Å)	$d_{Si\text{-}H}$ (Å)	$d_{Si\text{-}Si}$ (Å)	$\delta_{A\text{-}A'}$ (Å)	E_f (eV)
5.24	1.5	①2.4, ②2.36, ③2.33	1.08	-11.61

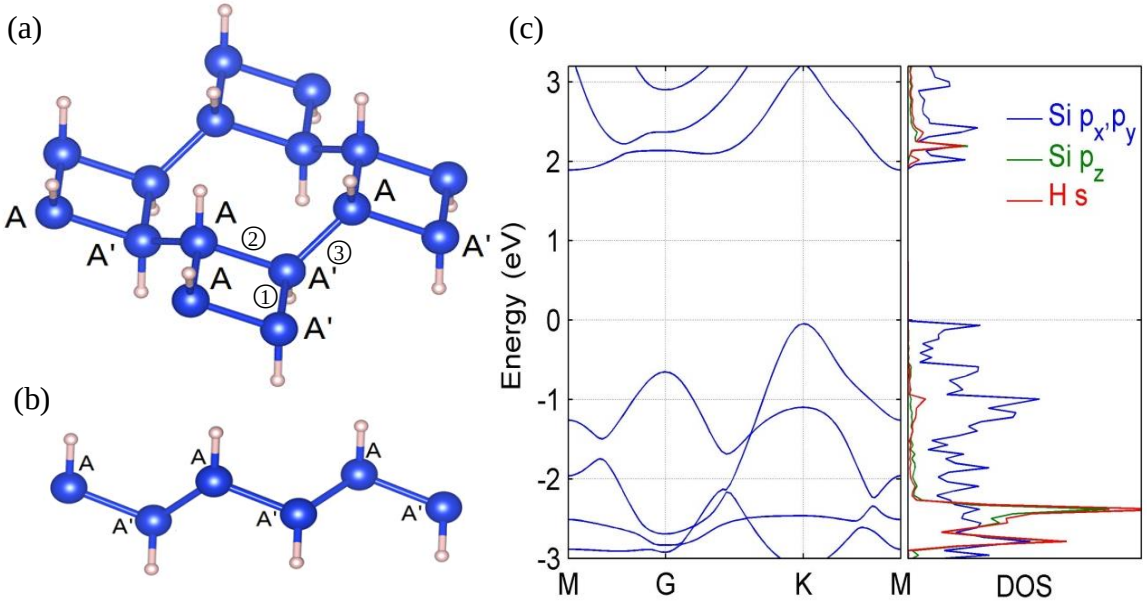

Figure 4.4 2×2 hydrogenated octasilicene seen from the (a) top and (b) side view. (c) Band structure and PDOS of hydrogenated octasilicene.

The band structure of hydrogenated octasilicene shows an indirect band gap of 1.9 eV in Figure 4.4(c). The top of the valence bands is at the K point and the bottom of conduction bands is located at the M point. The valence bands around the Fermi level are occupied by Si-p_x,p_y states, which is different from octasilicene, where the states around the Fermi level are dominated by Si-p_z states. The Si-p_z states have a lower energy level in the valence bands and hybridize well with H-1*s* states, which indicates a strong bonding between Si and H atoms. The $3p_z$ orbital is no longer a dangling bond, but forms a covalent bond with the H atom, and hence, a band gap is opened up in the band structure.

4.4.2 Silicyne

The relaxed structure of silicyne shows that the unit cell remains a hexagonal structure composed of 12 silicon atoms in spite of the inserted linkage between the hexagonal rings. The lattice constant of 10.56 Å for the 1×1 silicyne unit cell is larger than that of graphyne. Unlike graphyne, the silicon atoms are not in the same plane. According to the symmetry of the structure, four types of silicon atoms could be identified, which are Si_A, $Si_{A'}$, Si_B, $Si_{B'}$, as shown in Figure 4.5(b). The Si_A and $Si_{A'}$ are two atoms in the hexagonal ring. The Si_B and $Si_{B'}$ atoms comprise the linkage between the hexagonal rings. The Si_A and Si_B atoms are higher than their counterparts, $Si_{A'}$ and $Si_{B'}$, respectively. As seen in Figure 4.5(c), the buckling between Si_B and $Si_{B'}$ is larger than that between Si_A and $Si_{A'}$. The four Si atoms in the linkage ($-Si_A - Si_{B'} - Si_B - Si_{A'} -$) are not collinear, differing from graphyne. The bonds ① and ② connected to Si_A or $Si_{A'}$ are 2.29 Å in length, almost the same as in silicene (2.27 Å). The length of bond ③ between Si_B and $Si_{B'}$ is closer to the typical double bond length

of 2.16 Å.[138] The bond angle in the hexagonal ring is 115.6° and that between the double bond and the adjacent silicon is 127 °. Therefore, we can conclude that sp^2 and sp^3 hybridization co-exist in this system. The Si_A and $Si_{A'}$ atoms on the hexagonal ring have sp^3 hybridization, whereas Si_B and $Si_{B'}$ in the linkage have sp^2 hybridization.

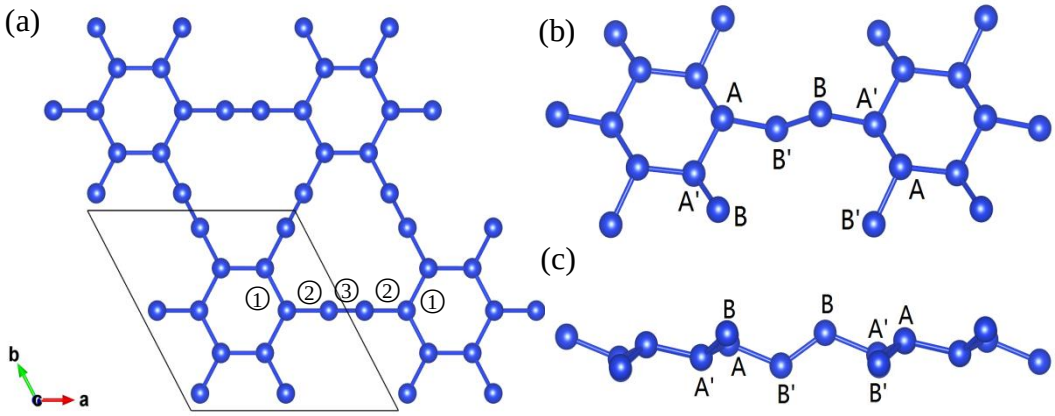

Figure 4.5 (a) 2×2 hexagonal structure of silicyne in the *ab*-plane. The parallelogram drawn with a black line represents a 1×1 unit cell. The 2×1 hexagonal structure of silicyne from (b) the top view and (c) side view.

Table 4.4 Structural parameters of 1×1 unit cell of silicyne: lattice constant $|a|$, bond lengths ($d_{Si\text{-}Si}$), bucklings ($\delta_{A\text{-}A'}$ and $\delta_{B\text{-}B'}$), bond angle ($\theta_{AB'A}$), and cohesive energy (E_{coh}).

$\|a\|$ (Å)	$d_{Si\text{-}Si}$ (Å)	$\delta_{A\text{-}A'}$ (Å)	$\delta_{B\text{-}B'}$ (Å)	$\theta_{AB'A}$ (°)	E_{coh} (eV)
10.56	①②2.29, ③2.15	0.48	1.14	127	-40.55

As for the electronic properties, silicyne turns out to be a metal from the band structure in Figure 4.6. The states at the Fermi level are mainly attributed to p_z orbital

sates from $Si_{A(A')}$ atoms and p_y and p_z orbital states from $Si_{B(B')}$ atoms. The $Si_{A(A')}$ atoms in sp^3 hybridization have three σ orbitals to form covalent bonds with neighbouring atoms, leaving a dangling bond in silicyne From the DOS, we can see that the bands crossing the Fermi level mainly come from the $3p_z$ orbital. The $Si_{B(B')}$ atoms only connect with two neighbouring atoms covalently and possess two dangling bonds, primarily contributed by $3p_y$ and $3p_z$ orbitals. We can conclude that the dangling bonds contribute to the states at the Fermi level. In order to change the electronic properties of silicyne, we will try to adsorb hydrogen atoms on silicyne to eliminate the dangling bonds in the following sections.

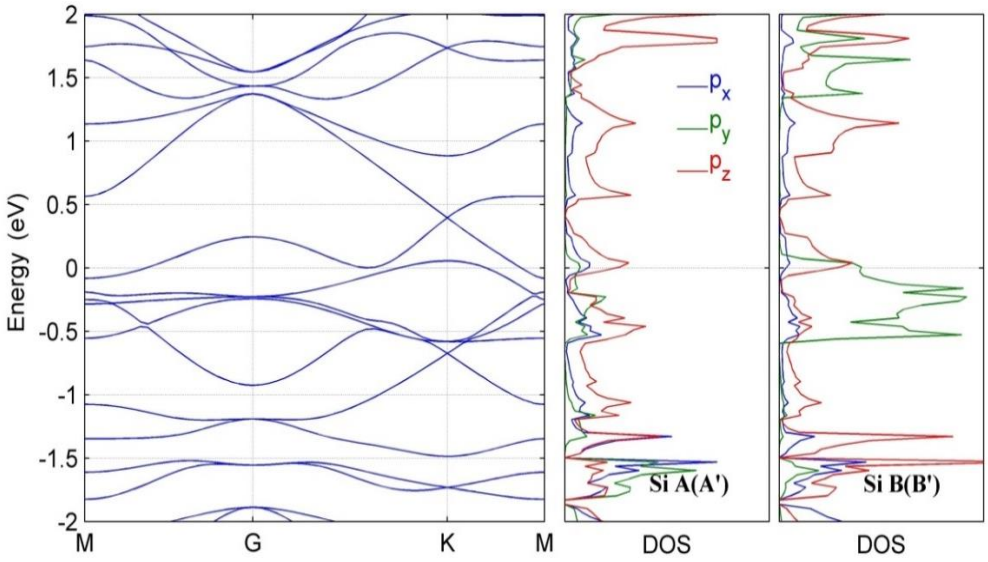

Figure 4.6 Band structure of silicyne (left) and PDOS of $Si_{A(A')}$ and $Si_{B(B')}$ atoms (right).

As each $Si_{A(A')}$ atom and $Si_{B(B')}$ atom is able to provide one and two electrons, respectively, to form extra chemical bonds, we will have two adsorption styles for silicyne. The first one is to make each $Si_{A(A')}$ or $Si_{B(B')}$ atom attract only one H atom,

which contributes to a total of 12 H atoms adsorbed on the 1×1 unit cell of silicyne, as shown in Figure 4.7. The second one is the adsorption of the amount of 18 H atoms on silicyne, where each $Si_{A(A')}$ atom attracts one H atom and each $Si_{B(B')}$ atom attracts two H atoms for adsorption. The two types of adsorption structures will be analysed in Sections 4.4.2.1 and 4.4.2.2, respectively.

4.4.2.1 Adsorption of 12 H Atoms on Silicyne

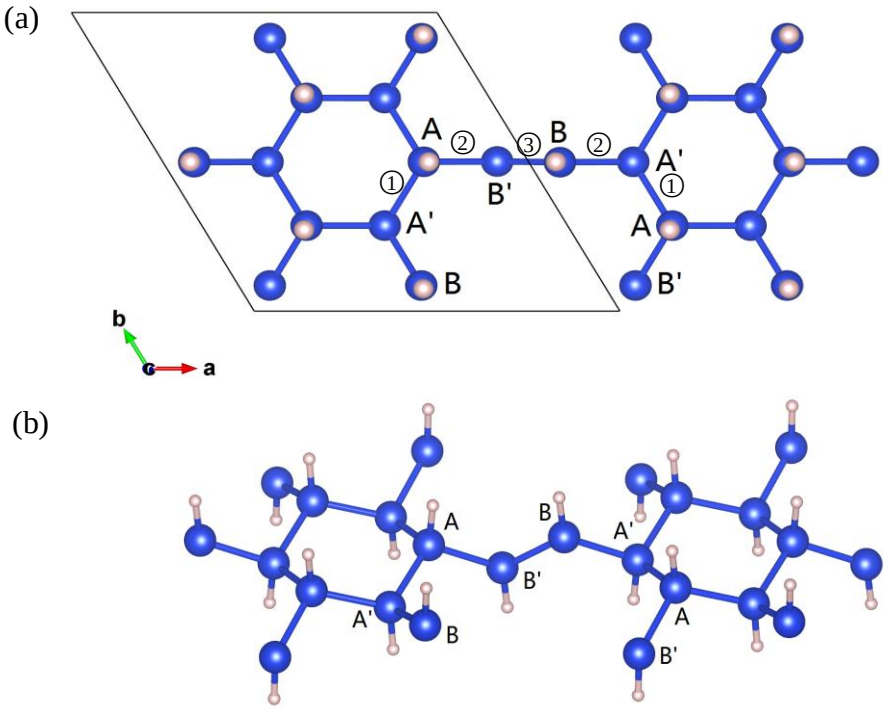

Figure 4.7 Relaxed structure of 12 H atoms on silicyne from (a) top view and (b) side view. The blue and pink spheres stand for the Si atoms and H atoms, respectively.

As shown for the relaxed structure of 12 H atoms on silicyne in Figure 4.7, the 12 H atoms are on both sides of the *ab* plane in an alternating way. The H atoms adsorbed on Si_A and Si_B atoms are above the plane, while those adsorbed on $Si_{A'}$ and

$Si_{B'}$ atoms are below the plane. The adsorbed H atoms make the lattice constant of silicyne increase to 0.4 Å. The bond lengths and the buckling are also enlarged. Bond ① in the hexagonal ring is a typical single bond Si(sp^3)–Si(sp^3) bond (2.36 Å). Bond ③ has a typical double bond length of 2.16 Å. Bond ②, located between bonds ① and ③, has the character of Si(sp^2)-Si(sp^3). The bond lengths and angles demonstrate that this type of adsorption gives $Si_{A(A')}$ and $Si_{B(B')}$ atoms perfect sp^3 and sp^2 hybridization, respectively. Although $Si_{B(B')}$ atoms still have a dangling bond, the band gap has been opened up successfully in the band structure.

Table 4.5 Structural parameters of 12 H on silicyne in 1×1 unit cell: lattice constant $|a|$, bond lengths ($d_{Si\text{-}H}$, $d_{Si\text{-}Si}$), bucklings ($\delta_{A\text{-}A'}$, $\delta_{B\text{-}B'}$), bond angle ($\theta_{AB'A}$), and formation energy (E_f).

$\|a\|$ (Å)	$d_{Si\text{-}H}$ (Å)	$d_{Si\text{-}Si}$ (Å)	$\delta_{A\text{-}A'}$ (Å)	$\delta_{B\text{-}B'}$ (Å)	$\theta_{AB'A}$ (°)	E_f (eV)
10.60	1.50	①2.36, ②2.31, ③2.16	0.65	1.17	124.2	-35.58

The adsorption of 12 H atoms on silicyne achieves an indirect band gap of 1.2 eV. The Si-H bond is almost perpendicular to the plane, indicating that the H-1*s* orbital is bonded to the Si 3p_z orbital. As revealed in Figure 4.8, for both $Si_{A(A')}$ and $Si_{B(B')}$, the Si p_z states located in the valence bands have lower energy than p_x, p_y states and hybridize well with H-*s* states. The valence bands of Si_A and $Si_{A'}$ atoms near the Fermi level are dominated by p_x and p_y states, suggesting the hybridization of p_x and p_y orbitals between the two atoms. For Si_B and $Si_{B'}$ atoms, p_y states occupy the valence

bands near the Fermi level. This implies that p_y orbitals from Si_B and $Si_{B'}$ atoms bond to each other, forming a strong double bond between Si_B and $Si_{B'}$ atoms.

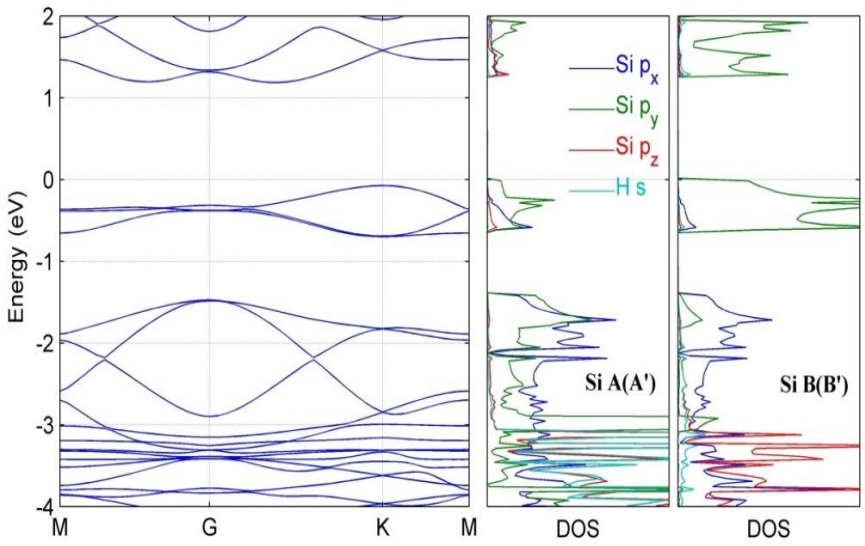

Figure 4.8 Band structure of 12 H atoms on silicyne (left) and PDOS of $Si_{A(A')}$ and $Si_{B(B')}$ atoms (right).

4.4.2.2 Adsorption of 18 H Atoms on Silicyne

As we put one more H atom on each Si_B or $Si_{B'}$ atom, based on the structure of 12 H atoms on silicyne, which results in 18 H atoms on silicyne, the structure and electronic properties are obviously distinct from those of the previous structure.

In the structure shown in Figure 4.9, each Si atom is bonded with four other atoms, and hence, the orbitals of the Si atoms are fully filled by electrons. The lattice constant is reduced to even less than in silicyne. All Si-Si bond lengths are closer to the typical single bond length. Compared with the 12 H on the silicyne structure, the buckling between Si_A and $Si_{A'}$ atoms shrinks a little, while the buckling between Si_B and $Si_{B'}$ is significantly enlarged. The bond angle of $\theta_{AB'A}$ is further reduced to 112.5˚,

indicating that the hybridization of $Si_{B(B')}$ is converted to sp^3. The formation energy of 18H on silicyne is much lower than that of 12 H on silicyne. This demonstrates that the structure of 18H on silicyne is more stable and that the Si atom prefers the sp^3 hybridization.

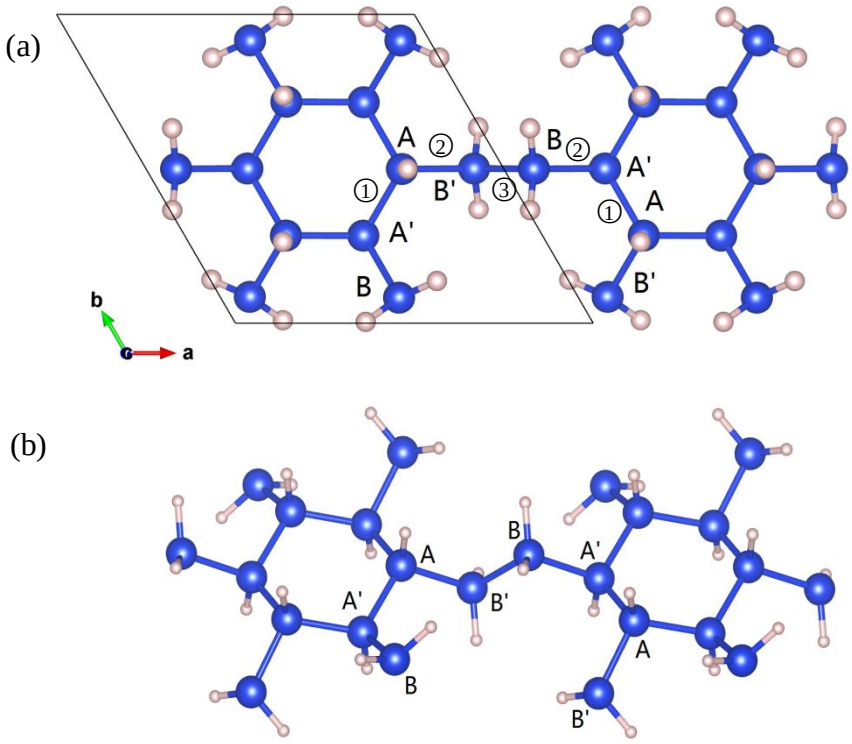

Figure 4.9 Relaxed structure of 18 H atoms on silicyne from (a) top view and (b) side view. The blue and pink spheres stand for the Si atoms and H atoms, respectively.

Table 4.6 Structural parameters of 18 H on silicyne in 1×1 unit cell: lattice constant $|a|$, bond lengths ($d_{Si\text{-}H}$, $d_{Si\text{-}Si}$), bucklings ($\delta_{A\text{-}A'}$, $\delta_{B\text{-}B'}$), bond angle ($\theta_{AB'A}$), and formation energy (E_f).

$\|a\|$ (Å)	$d_{Si\text{-}H}$ (Å)	$d_{Si\text{-}Si}$ (Å)	$\delta_{A\text{-}A'}$ (Å)	$\delta_{B\text{-}B'}$ (Å)	$\theta_{AB'A}$ (°)	E_f (eV)
10.50	1.50	①2.34, ②2.35, ③2.34	0.58	1.55	112.5	-54.41

More H atoms attracted onto silicyne also leads to a larger band gap. As presented in Figure 4.10, a direct band gap of 3.05 eV appears at the G point in the band structure. For Si_A and $Si_{A'}$ atoms, the p_z states hybridize with H-*s* states, located in the lower energy levels of the valence bands, compared with p_x, p_y states located in the valence bands near the Fermi level. The p_x, p_y states in two neighbouring atoms hybridize with each other, forming σ bonds, as shown in the PDOS for $Si_{A(A')}$ atoms. As for Si_B and $Si_{B'}$ atoms, the p_z and p_y states are hybridized with the H_1-*s* and H_2-*s* states, respectively, demonstrating the two Si-H bonds on each Si_B or $Si_{B'}$ atom. The p_x states of Si_B and $Si_{B'}$ atoms are located on higher energy valence bands, in comparison with p_y and p_z states.

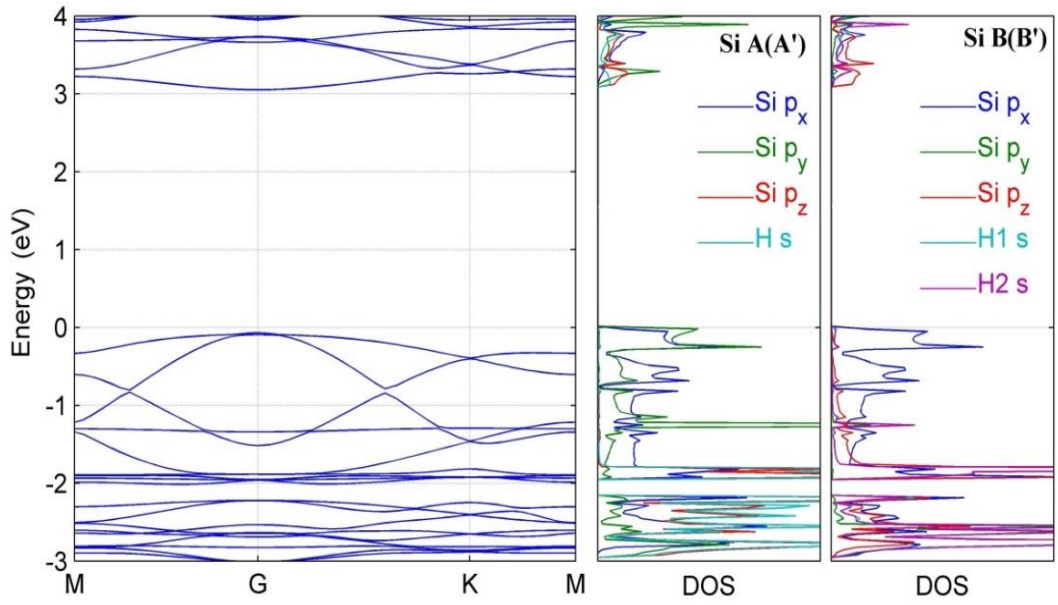

Figure 4.10 Band structure of 18 H atoms on silicyne (left) and PDOS of $Si_{A(A')}$ and $Si_{B(B')}$ atoms (right).

4.4.3 Silicdiyne

The optimized structure of silicdiyne is shown in Figure 4.11 and the structural parameters are listed in Table 4.7. Similar to graphdiyne, silicdiyne is formed by inserting the linkage ($-Si \equiv Si - Si \equiv Si-$) between the hexagonal rings in silicene. The 1×1 hexagonal unit cell of silicdiyne is composed of 18 silicon atoms.

According to the symmetry, six types of atoms could be identified, as shown in Figure 4.11(b) and (c). The six types of atoms are not in the same plane. The bucklings in the linkage are larger than those in the hexagonal ring.

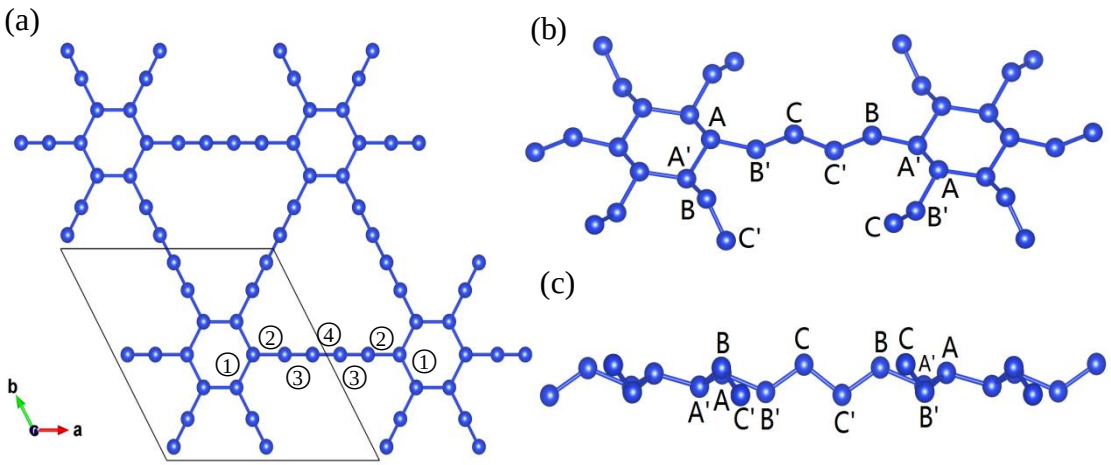

Figure 4.11 (a) 2×2 hexagonal structure of silicdiyne in the *ab*-plane. The parallelogram drawn with a black line represents the 1×1 unit cell. The 2×1 hexagonal structure of silicdiyne from (b) the top view and (c) the side view.

Bond ① between Si_A and $Si_{A'}$ in the hexagonal ring has the largest bond length (2.31 Å) and appears to be a single bond. Bond ③ has the shortest bond length (2.21 Å), which is closer to the double Si bond length. Bond ② has shorter bond length than bond ①, owing to the neighbouring double bond. Bond④ is shorter than bond ②, due

to the two double bonds located on both sides of it. Therefore, the Si_A and $Si_{A'}$ atoms have sp^3 hybridization, as in silicene. The bond angles $\theta_{AB'A}$ and $\theta_{B'CC'}$ with the values of 128.8˚ and 114.7˚ prove that $Si_{B(B')}$ and $Si_{C(C')}$ have sp^2 and sp^3 hybridization, respectively.

Table 4.7 Structural parameters of 1×1 unit cell of silicdiyne: lattice constant $|a|$, bond lengths ($d_{Si\text{-}Si}$), bucklings ($\delta_{A\text{-}A'}$, $\delta_{B\text{-}B'}$, and $\delta_{C\text{-}C'}$), bond angles ($\theta_{AB'A}$, $\theta_{B'CC'}$), and cohesive energy (E_{coh}).

$\|a\|$ (Å)	$d_{Si\text{-}Si}$ (Å)	$\delta_{A\text{-}A',\ B\text{-}B',\ C\text{-}C'}$ (Å)	$\theta_{AB'A,\ B'CC'}$ (˚)	E_{coh} (eV)
14.42	①2.31, ②2.29, ③2.21, ④2.26	0.56, 1.01, 1.27	128.8, 114.7	-58.51

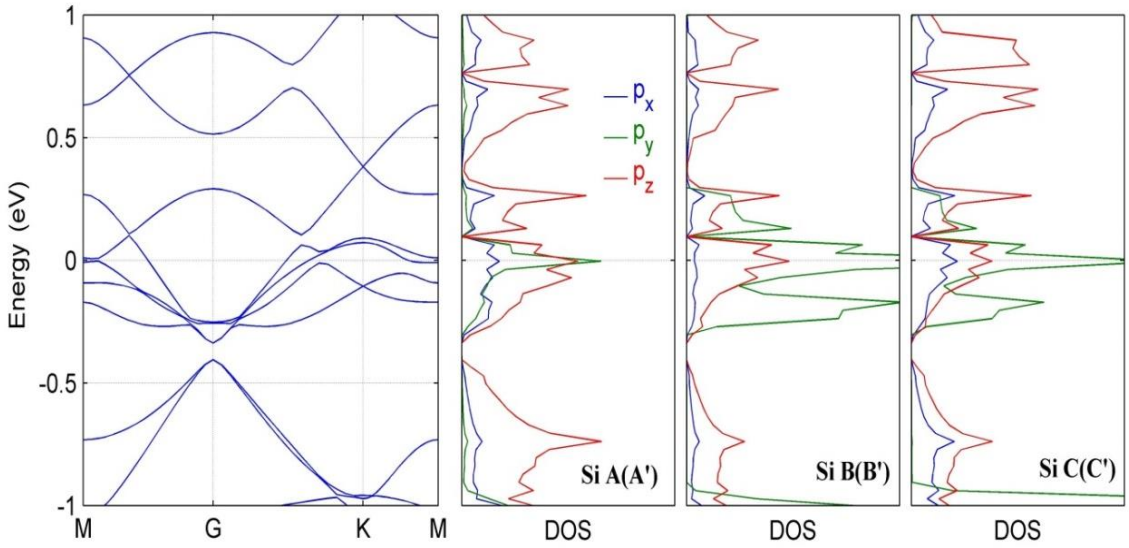

Figure 4.12 Band structure of silicdiyne (left) and PDOS of $Si_{A(A')}$, $Si_{B(B')}$ and $Si_{C(C')}$ atoms (right).

Analogous to silicyne, silicdiyne is also metallic. The density of states around the Fermi level is mainly attributed to the dangling bonds. To eliminate the dangling bonds and open up the gap in the band structure, the adsorption of H atoms on silicdiyne will be examined.

4.4.3.1 Adsorption of 18 H Atoms on Silicdiyne

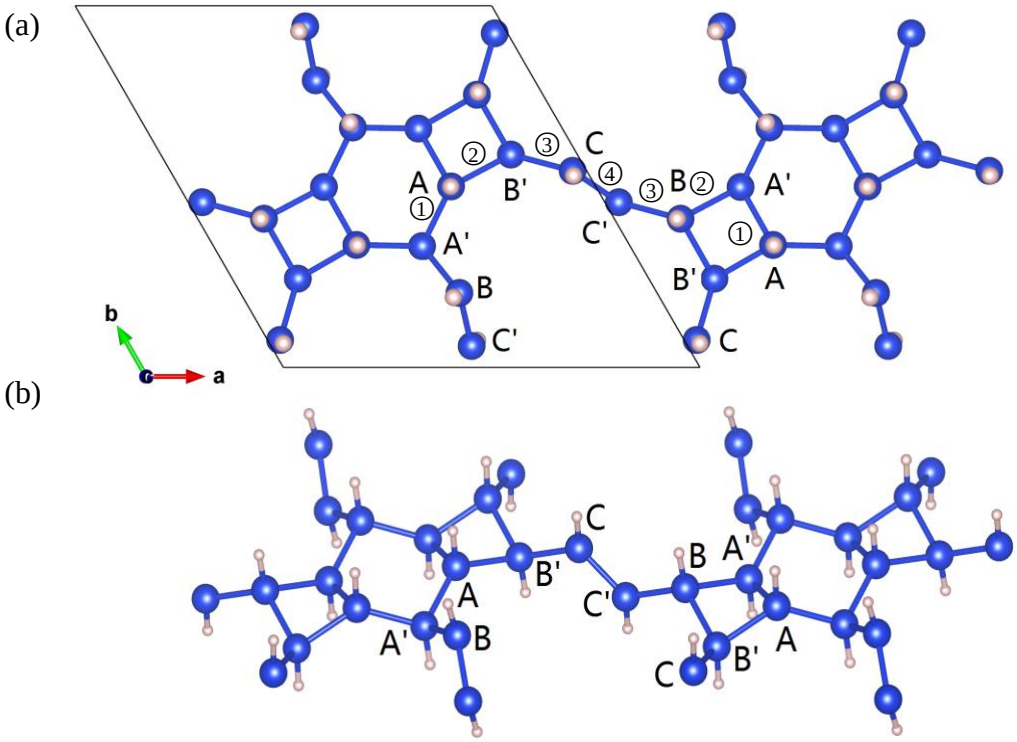

Figure 4.13 Relaxed structure of 18 H atoms on silicyne from the (a) top view and (b) side view. The blue and pink spheres stand for the Si atoms and H atoms, respectively.

First, we put one H atom on each silicon atom in an alternating way. As shown in Figure 4.13, the H atoms chemisorbed on Si_A, Si_B, and Si_C atoms are above the *ab*-plane, and those H atoms chemisorbed on $Si_{A'}$, $Si_{B'}$, and $Si_{C'}$ atoms are below the *ab*-plane. The adsorption on the hexagonal ring enlarges the buckling between Si_A and

$Si_{A'}$. The bonds ①, ②, and ③ with lengths of 2.34, 2.38, and 2.33 Å are all likely to be single bonds. Bond ④ with the length of 2.19 Å can be considered as a double bond. Si_B and $Si_{B'}$ not only connect with H atoms, but also bond with nearby Si_B or $Si_{B'}$. This behaviour pushes $Si_{B(B')}$ atoms towards sp^3 hybridization and proves that Si atoms favour sp^3 hybridization. The adsorption also makes $Si_{C(C')}$ atoms undergo a hybridization transition from sp^3 to sp^2, as the type of bond between Si_C and $Si_{C'}$ is a double one, and the bond angle increases to 124.2˚.

Table 4.8 Structural parameters of 18 H on silicdiyne in 1×1 unit cell: lattice constant $|a|$, bond lengths ($d_{Si\text{-}H}$, $d_{Si\text{-}Si}$), bucklings ($\delta_{A\text{-}A'}$, $\delta_{B\text{-}B'}$, and $\delta_{C\text{-}C'}$), bond angles ($\theta_{AB'A}$, $\theta_{B'CC'}$), and formation energy (E_f).

$\|a\|$ (Å)	$d_{Si\text{-}H}$ (Å)	$d_{Si\text{-}Si}$ (Å)	$\delta_{A\text{-}A',\ B\text{-}B',\ C\text{-}C'}$ (Å)	$\theta_{AB'A,\ B'CC'}$ (˚)	E_f (eV)
14.1	1.5	①2.34, ②2.38, ③2.33, ④2.19	0.69, 0.99, 1.11	123.8, 124.2	-59.02

This sort of adsorption also causes a band gap to appear in the band structure. The band gap appears to be an indirect one, with the top of the valence bands at the K point and the bottom of the conduction bands at the M point. The p_z states in each atom hybridize with H-*s* states, demonstrating the bonding between H and Si atoms. The DOS of $Si_{A(A')}$ and $Si_{B(B')}$ atoms are shown to be similar. From -2.6 to 0 eV, the states are mainly attributed to Si-p_x and Si-p_y hybridization. The states below -2.6 eV are occupied by Si-p_z and H-*s* hybridization. For $Si_{C(C')}$ atoms, the Si-p_z and H-*s* hybridization also appears in the lower energy area. There appear to be two peaks in the the Si-p_x and Si-p_y hybridization area from -3 to 0 eV. The first peak near the

Fermi level is mainly dominated by Si-p_y states, while the second peak located between -3 and -1.5 eV is mainly derived from Si-p_x states.

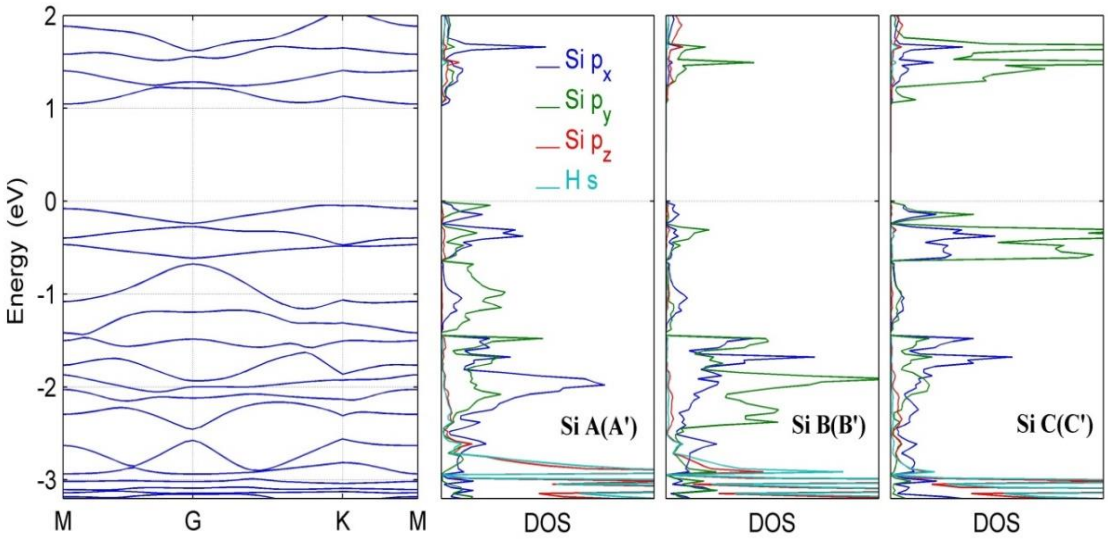

Figure 4.14 Band structure of 18 H atoms on silicdiyne (left) and PDOS of $Si_{A(A')}$, $Si_{B(B')}$, and $Si_{C(C')}$ atoms.

4.4.3.2 Adsorption of 30 H Atoms on Silicdiyne

The second kind of adsorption is the adsorption of one H atom on each Si_A or $Si_{A'}$ atom and the chemisorption of two H atoms on each $Si_{B(B')}$ or $Si_{C(C')}$ atom, which leads to a total of 30 H atoms on 1×1 silicdiyne. Every Si atom is bonded to four atoms and is in sp^3 hybridization. The Si-Si bonds are all likely to be single ones with almost equivalent bond lengths. The buckling in the linkage is larger than that in the ring. The formation energy of 30 H on silicdiyne is much lower than that of 18 H on silicdiyne, which once again demonstrates that the Si atom prefers the sp^3 hybridization.

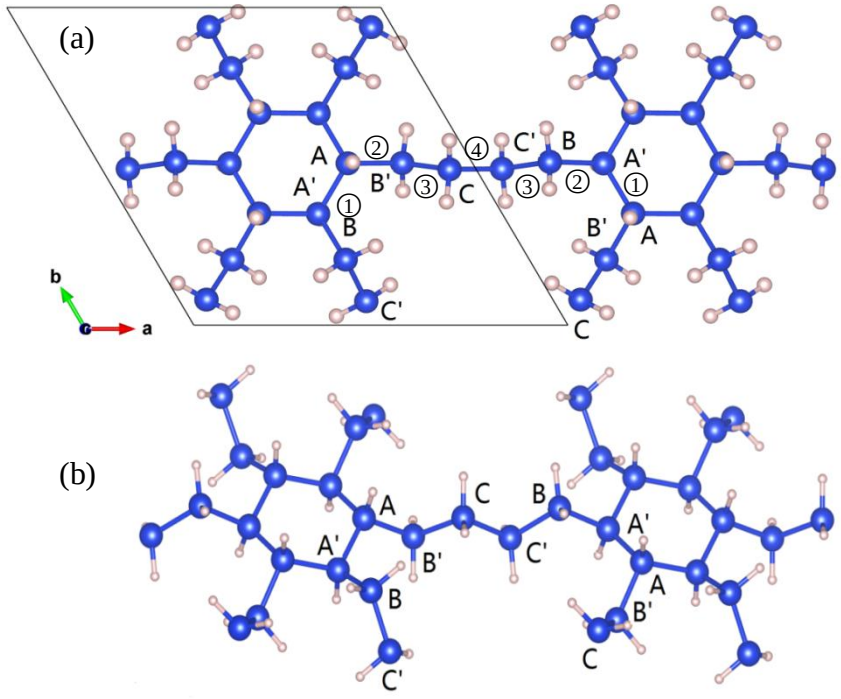

Figure 4.15 Relaxed structure of 30 H atoms on silicdiyne from the (a) top view and (b) side view. The blue and pink spheres stand for the Si atoms and H atoms, respectively.

Table 4.9 Structural parameters of 30 H on silicdiyne in 1×1 unit cell: lattice constant $|a|$, bond lengths ($d_{\text{Si-H}}$, $d_{\text{Si-Si}}$), bucklings ($\delta_{\text{A-A'}}$, $\delta_{\text{B-B'}}$, and $\delta_{\text{C-C'}}$), bond angles ($\theta_{\text{AB'A}}$, $\theta_{\text{B'CC'}}$), and formation energy (E_{f}).

$\|a\|$ (Å)	$d_{\text{Si-H}}$ (Å)	$d_{\text{Si-Si}}$ (Å)	$\delta_{\text{A-A', B-B', C-C'}}$ (Å)	$\theta_{\text{AB'A, B'CC'}}$ (˚)	E_{f} (eV)
14.4	1.5	①2.34, ②2.36, ③2.34, ④2.34	0.52, 1.68, 1.20	113.9, 110.7	-90.75

This adsorption enlarges the band gap, compared with 18 H atoms on silicdiyne. The band gap is around 3 eV at the G point. The hybridization properties are reflected in the density of states. For Si_{A} and $\text{Si}_{\text{A'}}$ atoms, the Si-p_z states hybridize with H-s states and are located in the lower energy states of valence bands, indicating that the

H-1*s* orbital bonds with the Si-3p_z orbital. The higher energy states of the valence bands are dominated by the hybridization between the Si-p_x and Si-p_y states. The densities of states of $Si_{B(B')}$ and $Si_{C(C')}$ atoms are analogous to each other. The Si-p_y and p_z states hybridize with two different H-*s* states, respectively, representing the two Si H bonds on each $Si_{B(B')}$ or $Si_{C(C')}$ atom. The Si-p_x states in the valence bands are located near the Fermi level.

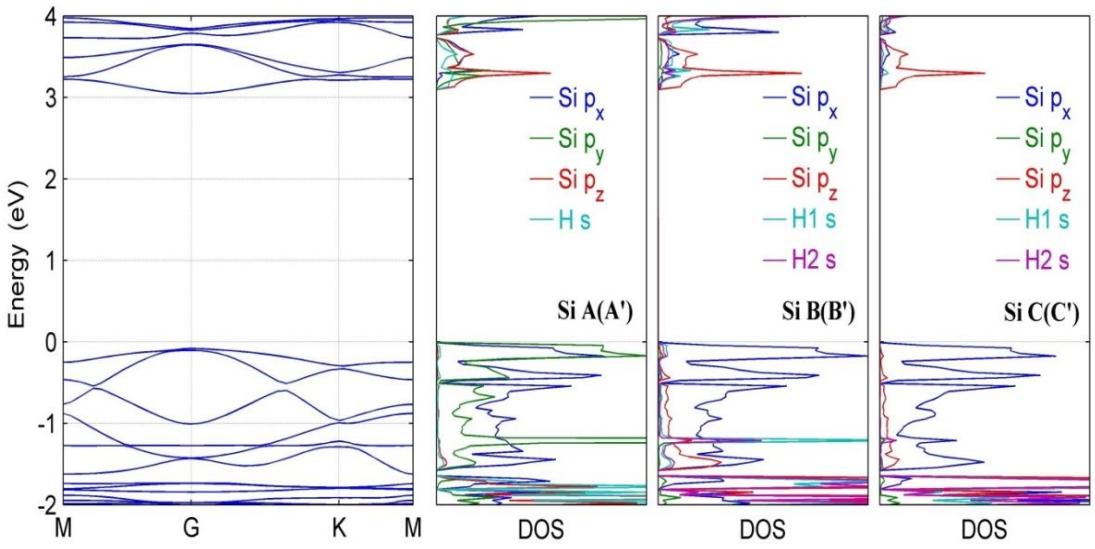

Figure 4.16 Band structure of 30 H atoms on silicdiyne (left) and PDOS of $Si_{A(A')}$, $Si_{B(B')}$, and $Si_{C(C')}$ atoms.

4.5 Conclusions

In this chapter, three types of silicene allotropes and their functionalization have been discussed. In the light of graphene allotropes, three new types of silicene allotropes, octasilicene, silicyne, and silicdiyne, were constructed and investigated. The band structures of the three silicene allotropes are all shown to be metallic, while

the hydrogenated silicene allotropes present as semiconductors. From the hydrogenated structures, it can be concluded that Si atoms favour the sp^3 hybridization.

As these allotropes of silicene display a high concentration of dangling bonds, they are highly unstable and extremely reactive. In order to gain enough electrons to fill their unsatisfied valence shells and manipulate their electronic conduction, hydrogen atoms were introduced to form valence bonds with silicon atoms. The hydrogenated octasilicene is formed by adsorbing one H atom on each silicon atom in an alternating way, resulting in an indirect gap in the band structure. Two styles of H adsorption were applied to silicyne and silicdiyne. The first one is to introduce one H atom on each alternate silicon atom. The second one is to adsorb one H atom on the silicon atom in the hexagon and two H atoms on each silicon atom in the linkage, to totally replace the dangling bonds with valence bonds. The first type of adsorption leads to an indirect gap in the band structure, while the second type contributes to a larger direct gap. According to the formation energy, the second type of adsorption is proved to be more stable. The Si atoms in the second type of adsorption are all in sp^3 hybridization, suggesting that the Si atom prefers to be in sp^3 hybridization.

CHAPTER 5. ELECTRONIC PROPERTIES OF FLUORINATED GERMANENE

5.1 Introduction

Graphene,[139, 140] a monolayer honeycomb planar sheet of sp^2-bonded carbon, has attracted considerable attention because of its remarkable properties,[3] such as the linear dispersion of the band structure near the Dirac point,[17] an outstandingly high electron mobility at room temperature,[1] massless Dirac fermions,[141] the anomalous quantum Hall effect,[15142] great breaking strength,[19] and high thermal conductivity.[143] The zero-gap spectrum limits graphene's applications. The properties of graphene can be controlled, however, by attracting other atoms and molecules, and then new two-dimensional crystals with designed electronic and other properties can be created.[121] For instance, fully hydrogenated graphene, the so-called graphane,[144] has a direct gap that has opened up at the G point. All the carbon bonds are in sp^3 configuration, and the hydrogen atoms are alternatively bonded to carbon on both sides of the plane. Fluorine is known to displace hydrogen in many hydrocarbons. The fully fluorinated analog, named fluorographene, [145] has been synthesized before, and it was demonstrated to be a wide-gap semiconductor.[146]

As the counterpart of graphene, the Si and Ge based monolayer hexagonal structures, silicene [147] and germanene, [148] possess similar electronic properties to graphene, being predicted to be gapless semiconductors. Due to their larger atomic radii, the stable structure for silicene and germanene consists of a low buckled (LB)[31,137] lattice structure, indicating that mixed sp^2-sp^3 hybridization stabilizes the

honeycomb structure. To date, silicene has been successfully synthesized on different supporting materials, such as Ag(111),[46, 149] ZrB_2,[47] and Ir(111)[150] surfaces. The flexible buckled structure gives silicene superiority over graphene. Buckled silicene grown on ZrB_2 thin films has an energy gap at the Fermi level,[151] which has originated from the larger spin-orbit coupling strength in silicene. It may induce a possible quantum-spin-Hall effect (QSHE)[35,151] and the quantum anomalous Hall effect (QAHE).[152] Silicene is a promising candidate for a topological insulator, which undergoes a topological phase transition to a band insulator under an external electric field.[153] Germanene has yet to be synthesized, however, it has higher buckling and also a much larger predicted spin-orbit gap compared to silicene.[35] In silicene, hydrogenation and fluorination could also remove the electronic states around the Dirac point and create a finite energy gap, and such an approach holds promise for applications in the future.[154,155,156] The fully hydrogenated and fluorinated silicene are named silicane and fluorosilicene, respectively. Four possible configurations were considered to determine their structures in a previous theoretical study,[157] including the chair, boat, zigzag-line, and armchair-line configurations. Silicane prefers the chair-like structure, which is analogous to graphane, while for fluorosilicene, the zigzag structure is energetically favorable.

Hydrogenated germanene, called germanane, has just been synthesized very recently.[158] This material also presents a graphane-like structure with a direct band gap of 1.53 eV and a high electron mobility, which shows its great potential for optoelectronic and sensing applications. Up to now, fluorinated germanene has not been studied deeply. In this study, we will focus on fluorinated germanene.

5.2 Computational Methodology

Our calculations were performed in the framework of density functional theory (DFT) with a plane-wave pseudopotential. The Vienna ab-initio simulation package (VASP) code was employed for the calculations.[118] The exchange-correlation effects were processed within the generalized-gradient approximation (GGA) with the Perdew- Burke-Ernzerhof (PBE) functional.[108] The plane-wave basis cut-off energy of 500 eV and the Monkhost-Pack k-point generation scheme with a grid of $17 \times 17 \times 1$ points were used for the relaxation of a hexagonal cell. Between two self-consistent iterations, the convergence criterion in total energy was set to 10^{-5} eV/atom. The systems were completely relaxed when the atomic forces were smaller than 1 kbar in any atom. To avoid interactions between neighboring layers, the distance between layers is larger than 15 Å.

5.3 Results and Discussion

5.3.1 Graphene, Silicene, and Germanene

Formation of elemental and binary graphene-like monolayer structures of Group IV elements such as silicene, germanene, SiC, and GeC was reported by Sahin *et al.*[137] It was also predicted that the monolayer hexagonal structure of tin (Sn_2) cannot be stable in freestanding form, whereas its binary compounds SnC, SnSi, and SnGe are stable even in free-standing form. Despite the graphene-like honeycomb lattice structure of germanene, the minimum energy equilibrium geometry displays a buckled structure like silicene, as shown in Figure 5.1. Considering the similar planar

structures of hexagonal BN and graphene, it appears that planarity comes with first row elements. Due to its buckled nature, the effective thickness of germanene can be expected to be measured as more than one-atom thick. As presented in Table 5.1, the GGA lattice constant of the hexagonal unit cell of germanene, silicene, and graphene is calculated to be 4.06, 3.87, and 2.47 Å, respectively, which are consistent with those previous calculations.[148,156,159] All the structures, except for graphene, were buckled. For germanene, the buckling height is found to be 0.69 Å, which is 0.24 Å larger than that of silicene. The bond angle θ between the Ge atoms in germanene is 112.4˚, distinct from bond angle of 120˚ between C atoms in graphene. This reflects the fact that due to the increasing bond length compared with that in the carbon atoms, the π bonds between germanium atoms are weakened and the overlap of p_z orbitals is decreased, leading to dehybridized sp^2 states. Thus, the honeycomb structure of germanene is stabilized by the mixed sp^2–sp^3 hybridization, rather than the complete sp^2 π-bonding as in planar graphene.

Germanene presents the dispersive band structures shown in Figure 5.1. The top of the valence band (VB) and the of bottom the conduction band (CB) are degenerate at the K point, demonstrating that zero-gap semimetallic behavior with Dirac-like electronic excitation is confirmed in germanene, as in graphene and silicene. Because of its linear dispersion of $E(\mathbf{k})$, the charge carriers near the Dirac point behave as massless Dirac fermions. From a theoretical perspective, the Fermi velocity of the Dirac fermions is estimated as $\sim 10^{-6}$ m/s for germanene.[31,137] It should be noted that germanene behaves as a semiconductor with a band gap of 24 meV at the K point, and there is also 0.19 eV spin orbit splitting at the Γ point, due to the intrinsic spin orbit coupling, as in the enlarged view in the inset in Figure 5.1(b), in good agreement with previous results.[151]

Table 5.1 Calculated parameters for germanene, silicene, and graphene: lattice constant a, interatomic distance (d), bond angle (ϑ), buckling (δ), and cohesive energy (E_{coh}) per unit cell.

	a (Å)	d (Å)	ϑ (˚)	δ (Å)	E_{coh} (eV)
Graphene	2.47	1.42	120.0	0.00	-15.93
Silicene	3.87	2.28	116.2	0.45	-7.91
Germanene	4.06	2.44	112.4	0.69	-7.65

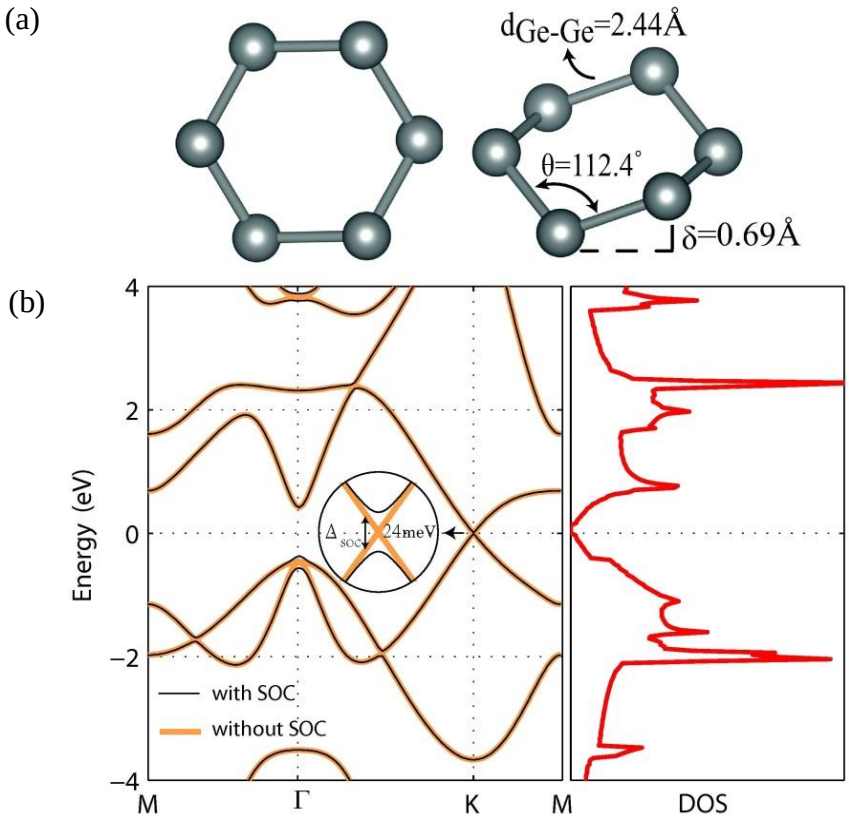

Figure 5.1 (a) Top and side views of gemanene structure. (b) Electronic band dispersion (left) and density of states (right) for perfect germanene. The energies are relative to the Fermi level (i.e., E_F = 0). The inset displays the calculated spin-orbit gap of 24 meV.

5.3.2 Adsorption of a Single Fluorine Atom on Germanene

To check at which site a single fluorine atom can adsorb on a germanene surface, four possible adsorption sites on germanene are considered due to its buckled hexagonal lattice structure, as for the adsorption study on silicene, [136, 160] which are above the center of the hexagonal germanium rings (hollow site), on top of the upper germanium atoms (hill site), on top of the lower germanium atoms (valley site), and on top of the Ge-Ge bond (bridge site) , as shown in Figure 5.2.

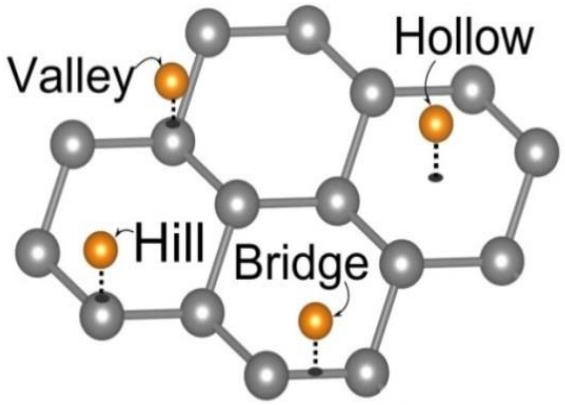

Figure 5.2 Possible adsorption sites on the germanene lattice. The gray and orange balls represent Ge and F atoms, respectively.

After full geometry optimization, the hill site is found to be the most favorable adsorption site, and the valley site on the lower germanium atoms is the next most favorable one. The adsorption of the fluorine atom on the hollow site is impossible on the germanene lattice, as the fluorine atom moves from the hollow site to the hill site automatically after relaxation. The adsorption of a fluorine atom at the bridge site leads to great distortion on the germanene lattice. The binding energy for adsorption is defined as $E_b = E_{system} - (E_{germanene} + E_{fluorine})$. The binding energy for the adsorption at the hill, valley, and bridge site is -4.05 eV, -4.02 eV, and -3.31 eV,

respectively. The case of adsorption of a fluorine atom at the hollow site is proved to be a nonmagnetic system with a metallic property, according to the band structure in Figure 5.3. The dangling Ge electron is saturated by F atoms, forming the F-Ge bond (1.82 Å). As a result of dehybridization from the mixed $sp^2 - sp^3$ structure to complete sp^3, the Ge-Ge bond length elongates from 2.44 to 2.50 Å, while the buckling δ is enlarged from 0.69 to 0.85 Å, and the bond angle between neighboring Ge atoms amounts to 109°.

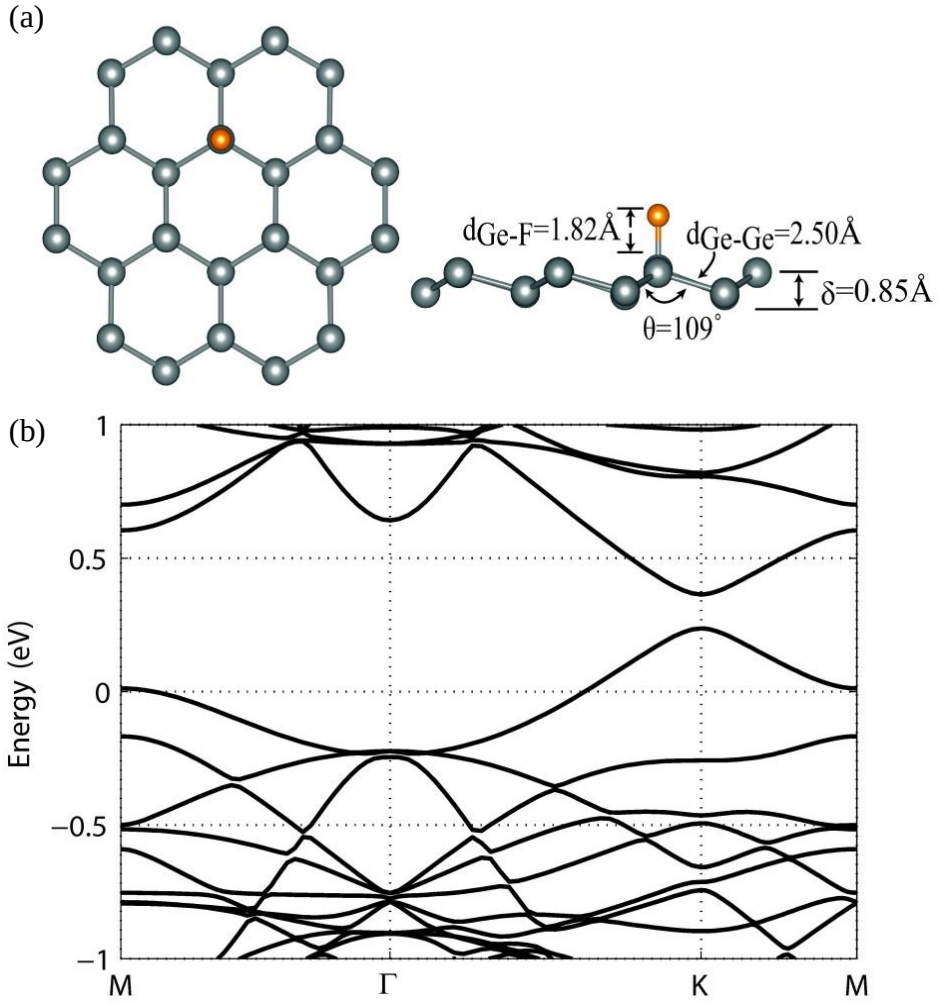

Figure 5.3 (a) Structural parameters for a single F on germanene at hill site and (b) electronic band dispersion.

5.3.3 Fully and Partially Fluorinated Germanene

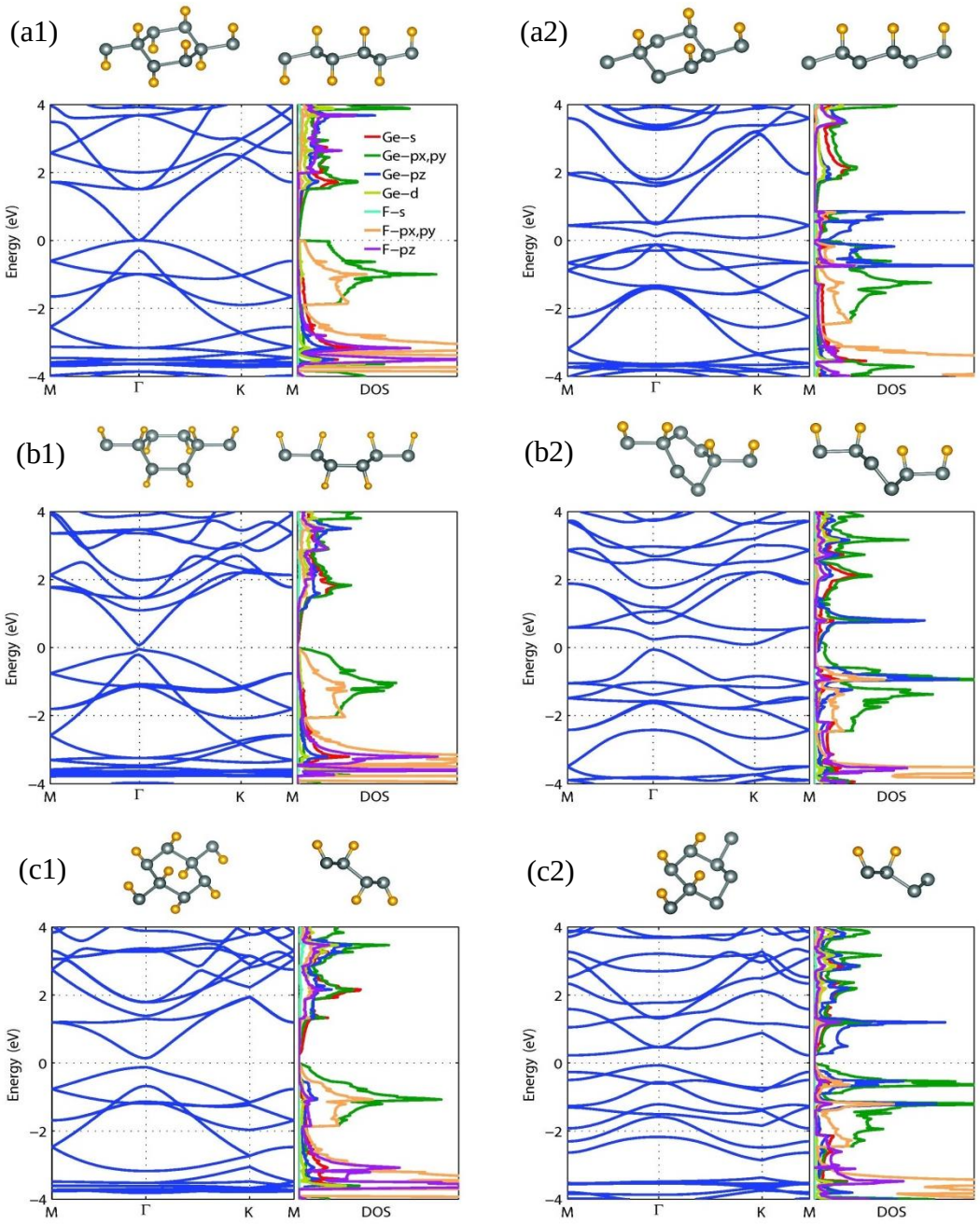

Figure 5.4 (a1), (b1), (c1) are the optimized and electronic structures of fully fluorinated gemanene in the chair-like, boat-like, and zigzag-like configurations, respectively. (a2), (b2), (c2) are the corresponding optimized and electronic structures of partially fluorinated gemanene. The optimized structures are given from the top and side view. The electronic structures include the band structures and the density of states. The gray and orange balls represent Ge and F atoms, respectively.

In graphene and silicene, fluorination could effectively alter the electronic properties. To study the effect of fluorination on germanene, three configurations are considered to study fully and partially fluorinated 2 × 2 germanene, including the chair-like, boat-like, and zigzag-like configurations. The chair-like configuration has fluorine atoms alternating on both sides of the plane containing germanium atoms. The boat configuration has buckling of alternating pairs, while the zigzag configuration has the buckling alternated by the zigzag lines, respectively. As shown in Figure 5.4(a1), (b1), and (c1), the germanene with the fluorine atoms on both sides of the plane is called fully fluorinated germanene. On the other hand, if the fluorine atoms are on one side of the plane, it is called partially fluorinated germanene, like the structures in Figure 5.4 (a2), (b2), and (c2). The optimized structural parameters of the fluorinated germanene structures and the formation energies are listed in Table 5.2. In the three fully fluorinated structures, only the chair-like structure keeps the symmetry of hexagonal structure. Compared with pure germanene, the lattice constant of the chair-like structure and the length $d_{\text{Ge-Ge}}$ of the Ge-Ge bonds are increased by about 6.1% and 2%, due to the formation of the Ge-F bond. The chair-like structure with a thickness of 4.16 Å is the thinnest one among the three structures. For the boat configuration, the lattice constant is 0.18 Å less, and the structure is 0.17 Å thicker than the chair-like configuration. The zigzag configuration has both the smallest and thickest lattice constants with $a \neq b$. The thickness increases with decreasing lattice constant. The lengths of F-Ge bonds are fixed in the three structures. The lengths of Ge-Ge bonds appear to be different for different positions in the boat-like and zigzag-like structures. It seems that, for the neighboring two Ge atoms, the Ge-Ge bonds with F atoms attracted on the same side of plane are longer than the Ge-Ge bonds with the attracted F atoms on the opposite sides of the plane. This is probably caused by the

repulsion between the neighboring fluorine atoms. The Ge atoms in fully fluorinated germanene are all saturated by F atoms, resulting in complete sp^3 hybridization.

The partially fluorinated germanene structures are thinner, compared with their corresponding fully fluorinated structures. The chair-like structure remains the thinnest one. The boat-like structure is distorted by the partially adsorbed fluorine atoms, which leads to four different Ge-Ge bond lengths and an unfixed Ge-F bond length, with this structure becoming the thickest one. The partially chemisorbed fluorine atoms are also twisted in the zigzag structure, as three different Ge-Ge bond lengths appear in the configuration. This is probably because the unsaturated Ge atoms in the partially fluorinated structure have interactions with the neighboring atoms though the dangling bonds and hence break the symmetry of the structure.

The binding energies E_b and formation energies E_f were calculated to determine their energetic stabilities. The binding energies are defined as $E_b = E_{total} - n_{Ge}E_{Geatom} - n_F E_{Fatom}$, where E_{total} is the total energy of various configurations, and E_{Geatom} and E_{Fatom} are the spin-polarized energies of the Ge and F atoms. We found that the cohesive energy was entirely negative for all of them and in the range between -36 and -15 eV, indicating a strong bond relative to the free atoms of the constituents. Nevertheless, a negative value of E_b alone is not sufficient to indicate whether a given fluorinated germanene is stable, but the formation energy, E_f, is usually taken to be a good criterion. The formation energies are defined as $E_f = E_{total} - E_{germanene} - \frac{n_F}{2}E_{F2}$, where $E_{germanene}$ is the total energy of the germanene and E_{F2} stands for the energy of a F_2 module. This justifies the view that incorporation of fluorine atoms leads to the chair-like structure for both partially and fully fluorinated germanene. For fully fluorinated germanene, the binding energies follow the order of $E_b(chair) < E_b(boat) < E_b(zigzag)$, demonstrating that the

chair-like configuration is the ground state. For partially fluorinated germanene, the energies have the order of $E_b(chair) < E_b(zigzag) < E_b(boat)$, suggesting that the chair-like configuration is energetically favorable. The formation energies also follow a similar sequence.

Table 5.2 The structural and energetic parameters for fully and partially fluorinated germanene.

	a (Å)	b (Å)	$d_{Ge\text{-}Ge}$ (Å)	$d_{\text{F-Ge}}$ (Å)	t (Å)	E_b (eV)	E_f (eV)	E_{gap} (eV)
Chair-full	8.62	8.62	2.55	1.79	4.16	-35.98	-30.44	0
Boat-full	8.44	8.44	2.57, 2.53	1.79	4.33	-35.77	-30.23	0.10
Zigzag-full	7.96	8.54	2.55, 2.53	1.79	4.71	-35.69	-30.16	0.23
Chair-partial	8.33	8.33	2.51	1.80	2.53	-15.45	-12.68	0
Boat-partial	7.65	7.65	2.57, 2.52, 5.43, 2.58	1.82, 1.78	3.88	-16.95	-14.19	0
Zigzag-partial	7.99	8.30	2.52, 2.53, 2.48	1.80	3.39	-16.96	-14.19	0.31

The different fluorinated configurations present various electronic properties. Figure 5.4 (a1, b1, c1) gives the band structures of the fully fluorinated gemanene. It is demonstrated that the chair-like structure is a semimetal. The valence band maximum (VBM) and the conduction band minimum (CBM), both of which are derived from the Ge p_x and p_y states, overlap at the Γ point. The band structure of the boat-like structure looks similar to that of chair-like structure, except for the small band gap of 0.1 eV that has opened at the Γ point. The gap is retained in the zigzag structure with an even larger value of 0.23 eV. The electronic band dispersion characteristics of the three configurations are qualitatively identical, which is caused

by the similar adsorption site and valence electron configuration. The valence bands near the Fermi level are mainly contributed by the hybridization of the Ge-p_x,p_y and F-p_x,p_y states. The conduction bands near the Fermi level primarily originate from hybridization of the Ge-p_x,p_y and Ge-*s* states. The Ge-p_z states are located in a lower energy level, due to the Ge-F bonds.

The band structures of partially fluorinated germanene behave differently, in contrast to those of fully fluorinated germanene, as shown in Figure 5.4 (a2, b2, c2) No gap appears in the band structure for the chair-like and boat-like configurations. A gap opens up for the zigzag configuration, however, with the value of 0.31 eV. It is shown that the VBM and CBM are located at the M point and Γ point, respectively. From the density of states, we can see that the valence and conduction bands near the Fermi level are dominated by Ge-p_z states for the chair-like structure, derived from the unsaturated Ge atoms. For the boat-like structure, the density of states (DOS) near the Fermi level is attributed to the hybridization between the Ge-p_x,p_y and Ge-p_z states, which is also applicable to the zigzag-like structure. It can be predicted that the unsaturated Ge atoms contribute to the DOS near the Fermi level for the partially fluorinated germanene.

5.4 Conclusions

We have studied the structural stability and electronic properties of fluorinated germanene. Due to the semimetallic property of germanene, fluorine atoms were applied on the germanene surface to open up a gap in the band structure. The chair-like structure was found to be the most stable configuration for partially and fully fluorinated germanene, however, the band gap does not exist in this structure.

The band gap only appears in the other two less stable structures. The boat-like structure is more stable than the zigzag-like structure for fully fluorinated germanene, while for partially fluorinated germanene, the energy order is reversed. The boat-like structure possesses a small direct gap, with the VBM and CBM coinciding at the Γ point for fully fluorinated germanene, but no gap exists for partially fluorinated germanene. The zigzag-like structure appears to be a semiconductor with an even larger direct band gap for fully fluorinated germanene and an indirect gap for the partially fluorinated germanene.

CHAPTER 6. ADSORPTION OF AN OXYGEN ATOM ON MONOLAYER MoS_2 STRUCTURE

6.1 Introduction

Recent research has demonstrated that dimensionality plays an important role in determining the fundamental properties of materials, in addition to the composition and arrangement of atoms. The unusual properties of graphene that are promising for a variety of novel applications have triggered significant interest in one or several-atom-thick honeycomb structures of binary compounds. The rapid progress in the methodology of preparing ultrathin layers has brought about exploration of other two-dimensional (2D) materials, especially the single layer transition metal dichalcogenides (TMDs) with similar structures to graphene.

Single layer TMDs, whose generalized formula is MX_2 (where M is a transition metal of groups IV-X and X is a chalcogen), displays versatile chemistry. Therefore, it provides great opportunities for technological and fundamental research in various fields, such as catalysis, energy storage, logic circuits, and sensing and electronic devices. The synthesis of nanosheets of MoS_2 and other transition-metal dichalcogenides, such as $MoSe_2$, WS_2, $MoTe_2$, $NbSe_2$, and $NiTe_2$, has been reported.[2,71,161] The monolayer MoS_2 is composed of hexagons with Mo and two S atoms located at alternating corners. Recently, this material in nanoribbon form has been the subject of several theoretical studies.[36,162,163]

MoS_2 has been utilized in ultra-low-friction studies. Recent theoretical

calculations [164, 165] and experiments[57, 166] on atomically thin sheets of MoS_2 have confirmed the superlubricity of the honeycomb MoS_2 structure. In addition, MoS_2 seems to be a potential material for many technological applications in other areas, such as hydrogen production, [167] photocatalysis, [168] solar cells, [169] and hydrodesulfurization catalysis for removal of sulfur compounds from oil.[170] Most recently, a transistor fabricated from single-layer MoS_2 exhibited superior features compared to graphene.[77]

Various properties have made the functionalization of single layer MoS_2 by adatoms a current issue. For instance, the adsorption of aromatic (benzothiophene, thiophene, benzene, pyridine, naphthalene, quinoline) and conjugated (butadiene) compounds on the (0001) basal plane of MoS_2 has been studied.[171] *Ab initio* calculations were carried on the adsorption of CO on the MoS_2 surface to obtain the relative energies of different reaction paths. Theoretical studies have established that adatoms can significantly modify the magnetic and electronic properties of this material[172].

In this Chapter, we present a first-principles study of the general effects of the adsorption of oxygen atoms on the electronic and magnetic properties of perfect single layer-MoS_2.

6.2 Computational Methodology

Our results are based on first-principles plane wave calculations within density functional theory (DFT), using projector augmented wave (PAW) potentials. Numerical calculations have been performed by using VASP.[118] The exchange correlation potential is approximated by the generalized gradient approximation

(GGA)[108] both for both the spin-polarized and the spin-unpolarized cases. All structures are treated within the periodic boundary conditions. All atomic positions and lattice constants are optimized by using the conjugate gradient method, where the total energy and atomic forces are minimized. Various tests regarding vacuum separation, kinetic energy cut-off energy, *k*-points, and grid points have been made. A large spacing of 20 Å between single layers of MoS_2 is taken to avoid the coupling between layers. A plane-wave basis set with kinetic energy cut-off of 600 eV is employed. In the self-consistent field potential and total energy calculations, the Brillouin zone (BZ) is sampled by special *k*-points. The numbers of these *k*-points are (15×15×1) for the unit cell and (5×5×1) for the adatom adsorption in a (3×3) supercell of monolayer MoS_2. The convergence for energy is chosen as 10^{-5} eV between two consecutive steps and the pressure in the unit cell is kept below 1 kbar.

6.3 Results and Discussion

The optimized lattice constant and other structural parameters are presented in Table 6.1. The lattice constants of MoS_2 are calculated to be $a = b = 3.18$ Å. The atomic structure of single-layer MoS_2, as shown in Figure 6.1, consists of a hexagonally packed layer of Mo atoms sandwiched between two layers of S atoms. The layered structure results in strong anisotropic properties, and thus, an intercalation process is easy to conduct. As reduced dimensionality can sometimes result in magnetic behavior in systems which are nonmagnetic in the bulk, both the spin-polarized state and spin-unpolarized states are included in our study. It was found that two-dimensional MoS_2 is in a nonmagnetic state. We calculated the cohesive energy relative to the free constituent atoms. The cohesive energy per MoS_2

cell was calculated using the expression $E_C = E_T[MoS_2] - E_T[Mo] - 2E_T[S]$, in terms of total energy of MoS_2, $E_T[MoS_2]$, and the total energies of free Mo and S atoms, $E_T[Mo]$ and $E_T[S]$, respectively. The cohesive energy is calculated to be -15.4 eV, implying a strong cohesion relative to free atoms of the constituents.

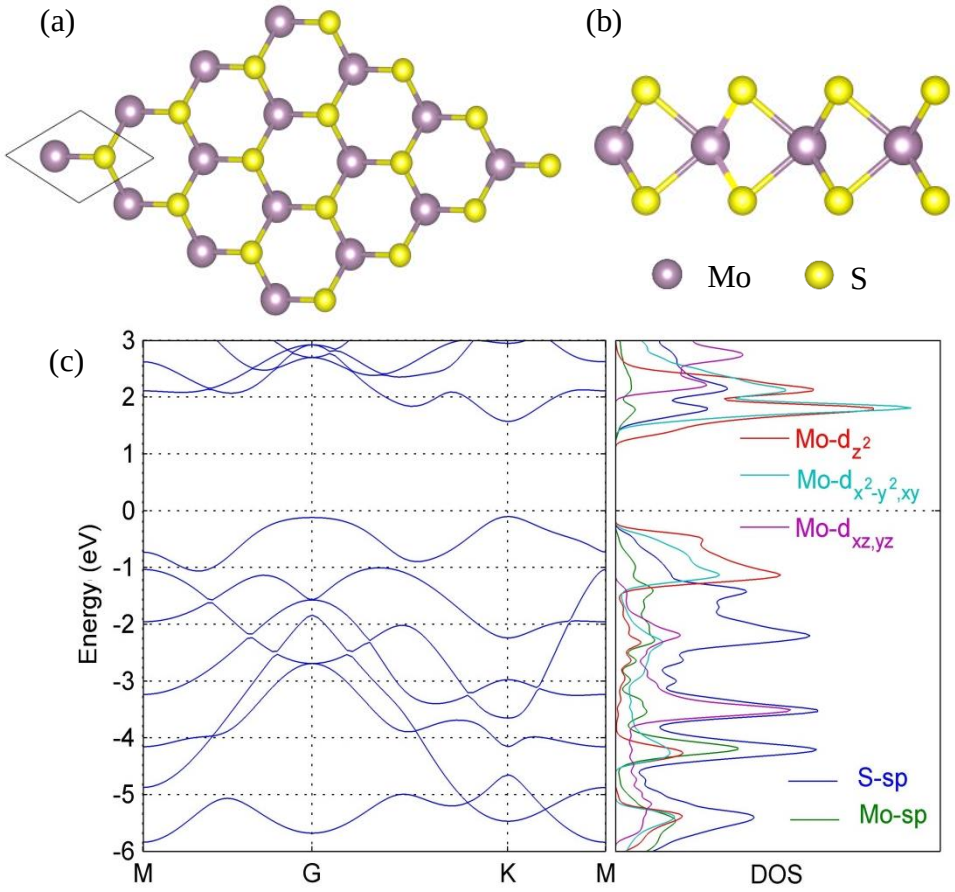

Figure 6.1 Atomic and electronic structures of 2D single-layer MoS_2. (a) Top and (b) side views of the 2D hexagonal lattice of MoS_2. The purple and yellow balls indicate Mo and S atoms, respectively. (c) The band structure (left) and density of states (right) of MoS_2.

According to the calculated density of states (DOS) in Figure 6.1, the two-dimensional variant of this compound is semiconducting: the bands on each side of

the band gap are mainly contributed by the Mo-*d* states, which the calculation of three-dimensional MoS_2 also displays.[173] As Mo in honeycomb MoS_2 has trigonal prismatic coordination, the *d* orbitals of the Mo atom split into three groups, d_{z^2}, $d_{x^2-y^2,xy}$, and $d_{xz,yz}$. The valence bands near the Fermi level are attributed mainly to d_{z^2} states, while the conduction bands are contributed by the hybridization of d_{z^2} and $d_{x^2-y^2,xy}$ states. From the band structure of two-dimensional MoS_2, we can see that the band gap, which has a value of 1.67 eV, is direct and occurs at the high-symmetry point K. The bands around the band gap are comparatively flat and are mainly derived from the "*d*" character of the electron states at these energies.

Table 6.1 Calculated values of single-layer MoS_2: lattice constants ($|a| = |b|$), bond lengths ($d_{Mo\text{-}S}$, $d_{S\text{-}S}$), bond angles ($\theta_{S\text{-}Mo\text{-}S}$, $\theta_{Mo\text{-}S\text{-}S}$), energy band gap ($E_g$) and cohesive energy per MoS_2 unit (E_{coh}).

a (Å)	$d_{Mo\text{-}S}$ (Å)	$d_{S\text{-}S}$ (Å)	$\vartheta_{S\text{-}Mo\text{-}S}$ (˚)	$\vartheta_{Mo\text{-}S\text{-}S}$ (˚)	E_g (eV)	E_{coh} (eV)
3.18	2.41	3.13	80.8	49.60	1.67	-15.4

The adsorption of adatoms is an efficient approach that can offer new functionalities to nanoscale structures. As we are interested in whether MoS_2 can be oxidized, which is an important issue for future applications, the decision was made to investigate the adsorption of oxygen atoms on 2D MoS_2, in order to know whether an O atom can form stable and strong bonds with monolayer MoS_2 or induce magnetization in nonmagnetic MoS_2.

The equilibrium adsorption site of the O atom was determined by first putting it at

one of three possible adsorption sites and afterward relaxing the entire structure. The three possible adsorption sites considered initially before the structure relaxation are (a) the hollow site slightly above the center of the hexagon on the Mo atomic plane, (b) the site on top of an S atom, and (c) the bridge site above a Mo-S bond. To guarantee that the results are related to the adsorption of an isolated adatom, a (3×3) supercell of single-layer MoS_2 was used to avoid interactions between O atoms.

Table 6.2 Calculated values for the properties of an O atom adsorbed on monolayer MoS_2, including adsorption sites of the O atom, lattice constant of the optimized structure, $|a|$, height of the O atom from the Mo layer, h_{Mo}, height of the O atom from the nearest S layer, h_s, distance from the O atom to the nearest Mo atom, d_{Mo}, distance from the O atom to the nearest S atom, d_s, adatom binding energy, E_{bind}, energy gap, E_g, and total magnetic moment per supercell, M_T.

Site	$\|a\|$ (Å)	h_{Mo} (Å)	h_s (Å)	d_{Mo} (Å)	d_s (Å)	E_{bind} (eV)	E_g (eV)	M_T (μ_B)
On top of S	9.55	2.97	1.48	3.51	1.48	-4.0	1.62	0
Hollow	9.68	0.01	1.59	1.96	2.56	-2.04	1.2	0

After full optimization, the O atom on the hollow site in the Mo plane and the site on top of an S atom can be stabilized, as shown in Figure 6.2. All the calculated data relating to an O atom adsorbed onto monolayer MoS_2 are presented in Table 6.2. The heights of the adatom from the Mo and S planes were calculated relative to the average heights of Mo and S atoms in the corresponding planes. The binding energy, E_b, was calculated as $E_b = E_{O+MoS_2} - E_O - E_{MoS_2}$, where E_{O+MoS_2} is the optimized total

energy of the system O + (3×3) supercell of monolayer MoS_2, E_O is the ground-state energy of the free O atom calculated in the same supercell with the same parameters, and E_{MoS_2} is the total energy of the (3×3) supercell of monolayer MoS_2. It was found that the adsorption site on top of the S atom is the most favorable place for an oxygen adatom, with a binding energy of -4.0 eV. The binding energy for the O atom adsorbed at the hollow site in the Mo plane is calculated to be -2.04 eV. Adsorbed O at both sites is nonmagnetic. The electronic structures for both adsorption structures are displayed in Figure 6.3 and Figure 6.4.

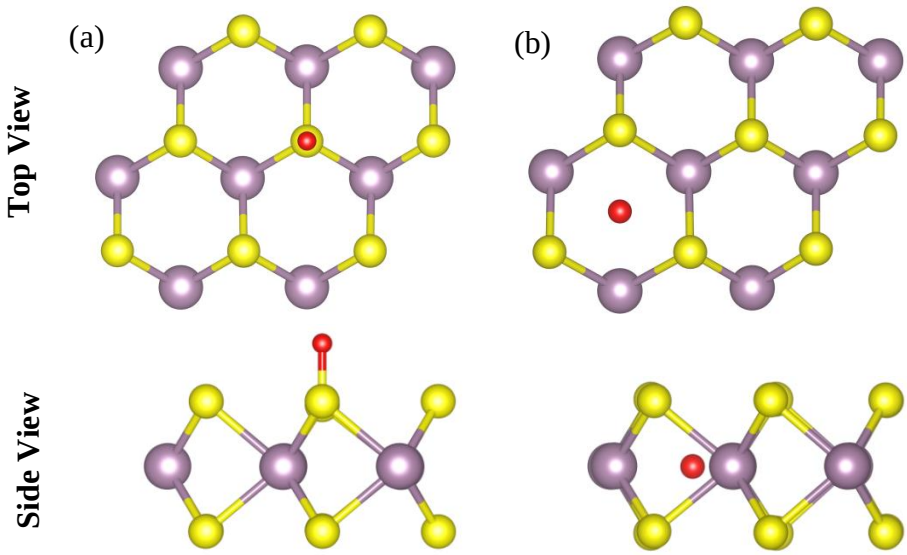

Figure 6.2 Top- and side-view schematic representations of two possible adsorption geometries for an adsorbed O atom obtained after structure optimization. O, Mo, and S atoms are represented by red, purple, and yellow balls, respectively. Side views clarify the heights of the O atom from the Mo and S atomic planes. Two adsorption sites are specified as (a) the top site above the S atom, which is consistent with the initial adsorption site before relaxation and (b) the hollow site in the Mo layer, where the O atom was placed initially (before structure optimization), slightly above the center of the hexagon on the Mo atomic plane.

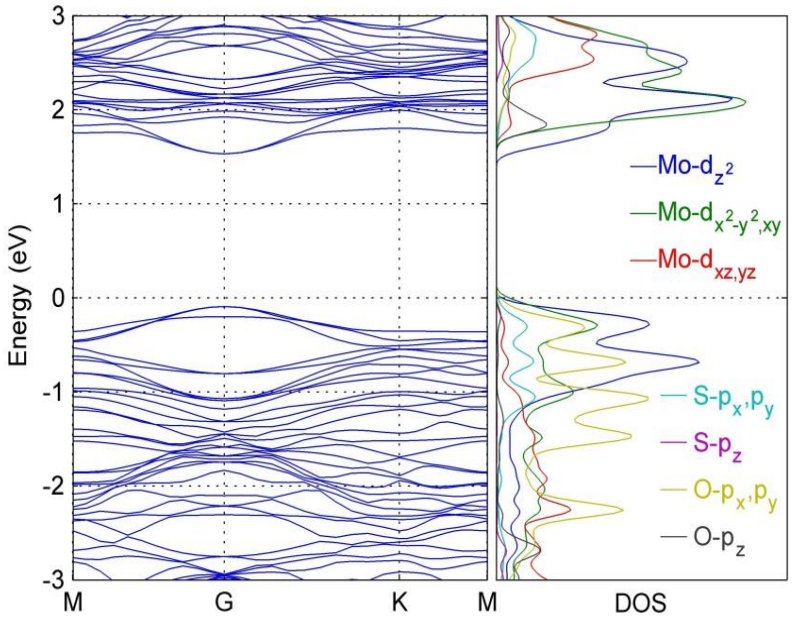

Figure 6.3 Electronic structure of a single O atom adsorbed on 3×3 monolayer MoS_2 on top of the S site: band structure (left) and density of states (right).

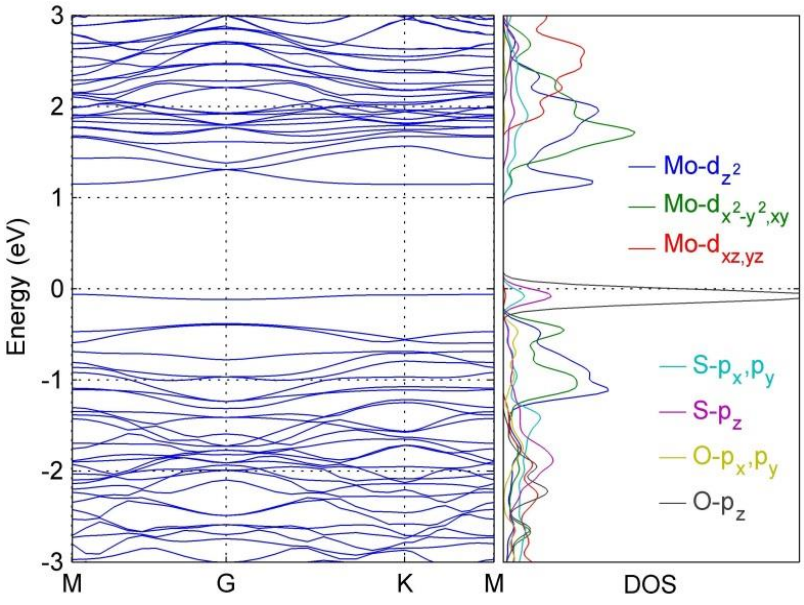

Figure 6.4 The electronic structure of a single O atom adsorbed on 3×3 monolayer MoS_2 at the hollow site in the Mo plane: band structure (left) and density of states (right).

As oxygen atom on top of an S atom does not influence the density of states of Mo. The band gap is direct at the G point with the DOS near the Fermi level dominated by states from Mo-*d* orbitals. The oxygen atom with high electronegativity has localized states near the band gap, originating from its p_x and p_y orbitals. Being in the same group as O, sulfur displays similar electronic properties and has localized states in the valence bands, which hybridize with O-p_x,p_y states, revealing the S-O bond. When the O atom is adsorbed at the hollow site in the Mo plane, the direct band gap opens at the M point. The bands on both sides of the gap are quite flat. The localized states occurring near the Fermi level are mainly derived from the O p_z orbital, combined with a small contribution from *p* orbitals of the S atoms. This reflects the fact that, although the Mo atom is closer to the O atom than the S atom, the O atom forms its bond with the nearest S atom.

6.4 Conclusions

On the basis of first-principles calculations, we have investigated the site preferences, geometric parameters, binding energy, and electronic and magnetic properties of the adsorption of an O atom on the two-dimensional single-layer MoS_2 honeycomb structure.

The O atom could be adsorbed on single-layer MoS_2 at two positions, on the hollow site in the Mo plane and at the site on the top of an S atom. According to the binding energy, the site on top of an S atom is the most energetically favorable position. Having the oxygen atom on top of an S atom results in a direct gap at the G point. Due to the S-O bond, the localized O-p_x,p_y states are hybridized with S-p_x,p_y states. The adsorption of an O atom at the hollow site in the Mo plane results in a

direct band gap that opens up at the M point. The localized states near the Fermi level are mainly attributed to the O p_z orbital, combined with a small contribution from S-*p* orbitals, reflecting the fact that the O atom prefers to couple with the nearest S atom, in spite of the closer Mo atom.

CHAPTER 7. ELECTRONIC BAND STRUCTURES OF A SERIES OF ISOSTRUCTURAL COMPOUNDS, M_2SiO_4 (M = Mn, Co, Ni)

7.1 Introduction

The olivine-type silicates with the general formula M_2SiO_4 (M = divalent cation) are among the most common and important minerals on Earth. Therefore, the properties of these materials are of fundamental importance for geologists and mineralogists. A large number of studies have been focused on olivine's crystal structure and lattice dynamics.[174-179] Typical examples of natural olivine-type silicates are forsterite (Mg_2SiO_4) and fayalite (Fe_2SiO_4). The olivine-type silicates also contain a few natural members with additional divalent cations, including Mn^{2+}, Co^{2+}, and Ni^{2+}. Owing to the presence of 3*d* transition metal cations, the M_2SiO_4 olivines exhibit a variety of interesting magnetic and electronic properties.[180-186]

M_2SiO_4 compounds crystallize in the orthorhombic space group *Pnma*, in which four chemical formula units are contained in the unit cell (Z = 4)[187]. The lattice can be described as distorted hexagonal close-packed, with Si^{4+} ions occupying one-eighth of the tetrahedral sites and the M^{2+} cations located in the octahedral sites. The olivine structure possesses a distinct magnetic lattice, in which metal ions sit at the vertices of corner-sharing triangles, forming alternating sawtooth chains. At low temperatures, olivines are antiferromagnetically ordered, with the magnetic cell equal to the crystallographic cell. Such a triangle of antiferromagnetically coupled spins often

gives rise to geometrical frustration, due to the competing exchange interactions between the three transition metals. The structure has two symmetry distinct transition metal *M* sites: *M*(1) ions are in sites of inversion symmetry, and *M*(2) ions are in the plane of mirror symmetry. The magnetic structure determined by neutron diffraction is quite complex. The magnetic moments and their temperature dependence are different for the two sites. The spins of *M*(2) have a collinear arrangement along the *b*-axis, whereas the *M*(1) spins are non-collinear and canted with respect to all the crystallographic axes.[180] These behaviours could have originated from the combination of the competing single-ion anisotropy of the different *M* sites, exchange interactions among a number of neighbouring ions, and Dzyaloshinskii-Moriya interactions.[188]

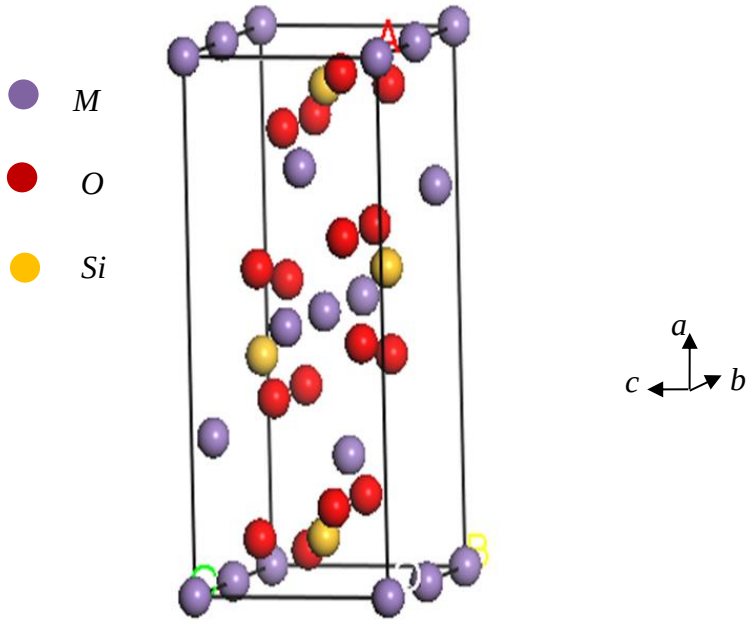

Figure 7.1 Unit cell of M_2SiO_4 (*M* = Mn, Co, and Ni). The *M* ions are indicated by blue spheres, the O ions by red spheres, and the Si ions by yellow spheres.

Recently, the olivine compound Mn_2GeO_4 was shown to exhibit directly coupled ferroelectric polarization and ferromagnetic magnetization that are both parallel to the same direction.[189] It is suggested that the direct coupling between the magnetism and ferroelectricity is mediated by Dzyaloshinskii-Moriya interactions. Motivated by this observation, we became interested in studying a series of isostructural compounds, M_2SiO_4 of the olivine family, for various transition metal cations M (Mn^{2+}, Co^{2+}, and Ni^{2+}). Our work has been focused on theoretical study of the olivine Mn_2SiO_4, Co_2SiO_4, and Ni_2SiO_4 compounds. In this paper, we present the magnetic and electronic states of Mn_2SiO_4, Co_2SiO_4, and Ni_2SiO_4, based on the first principles calculation method in the framework of density functional theory.

7.2 Computational Details

All calculations on the magnetic and electronic properties were performed in the framework of density functional theory (DFT) with a plane-wave pseudopotential. The CASTEP module of Material Studio 6.0 was employed in the calculations.[190] The exchange-correlation effects were processed within the generalized gradient approximation (GGA) with the Perdew-Burke-Ernzerhof (PBE) functional.[108] The Monkhost-Pack *k*-point generation scheme is used with a grid of $2 \times 4 \times 5$ points in the Brillouin zone for an orthorhombic cell. The plane-wave basis cut-off energy of 340 eV and the convergence criterion for energy of 10^{-5} eV have been selected in the calculation. Ultra-soft pseudopotentials were used for all chemical elements. In the DFT calculations, the GGA often fails to describe systems with strongly correlated *d* and *f* electrons. The electronic structure calculations within the GGA may predict a metallic ground state, contrary to experimental evidence that indicates insulating

behaviour at ambient pressure and temperature. In some cases, this can be remedied by introducing a strong on-site Coulomb energy (*U*) into GGA, which is known as the GGA+*U* method. These schemes, yielding quite satisfactory results for a few strongly correlated systems, are considered to be useful approaches. Therefore, our work is based on the GGA+*U* calculation. It is found that the calculated band gaps are compatible with optical measurements[191],[192] when U = 1.5 and 3.5 eV are used for Mn_2SiO_4 and Co_2SiO_4, respectively.

Table 7.1 Crystal lattice constants *a*, *b*, *c* and the unit cell volume *V* for Mn_2SiO_4, Co_2SiO_4, and Ni_2SiO_4 crystals.

	Mn_2SiO_4			Co_2SiO_4	Ni_2SiO_4		
	Exp.[193]	GGA	GGA+U	Exp. [195]	Exp.[194]	GGA	GGA+U
a (Å)	10.6002	10.7712	10.8549	10.2864	10.1232	10.3399	10.4090
b (Å)	6.2575	6.3582	6.4006	5.9872	5.9141	5.9932	6.0439
c (Å)	4.9034	4.9657	4.9852	4.7785	4.7311	4.7655	4.7954
V ($Å^3$)	325.2462	340.0987	346.3611	294.2922	283.2432	295.3134	301.6832

In terms of the magnetic structure, Mn_2SiO_4, Co_2SiO_4, and Ni_2SiO_4 are known to be antiferromagnetic compounds with a slightly non-collinear arrangement of spins on the *M*(1) ion sites.[179] This non-collinearity will not be addressed in the present calculations for simplicity. The experimental lattice parameters of Co_2SiO_4 at 2.5 K[195] were used for the calculation of Co_2SiO_4 in the ground state. For Mn_2SiO_4 and Ni_2SiO_4, only experimental lattice parameters at room temperature have been reported, which were used as an initial input for optimizing the crystal structure and

calculations of the electrical properties. The spin state of M^{2+} ions is set as high spin *s* in our calculations, which is according to experimental results.

Spin-polarized calculations in both the ferromagnetic (FM) and the antiferromagnetic (AFM) phases have been performed in this study. Through the dependence of the total energy on *U* for both AFM and FM phases within the GGA+*U* formalism, we find that the total energy of the AFM phase is lower than that of the FM phase for *U* in the range of 0 to 4 eV, indicating that AFM is the magnetic ground state, which confirms the experimental results. The lattice parameters for the compounds studied (both experimental and calculated) are shown in Table 7.1 Both FM and AFM results will be presented in the following analysis.

7.3 Results and Analysis

7.3.1 Mn_2SiO_4

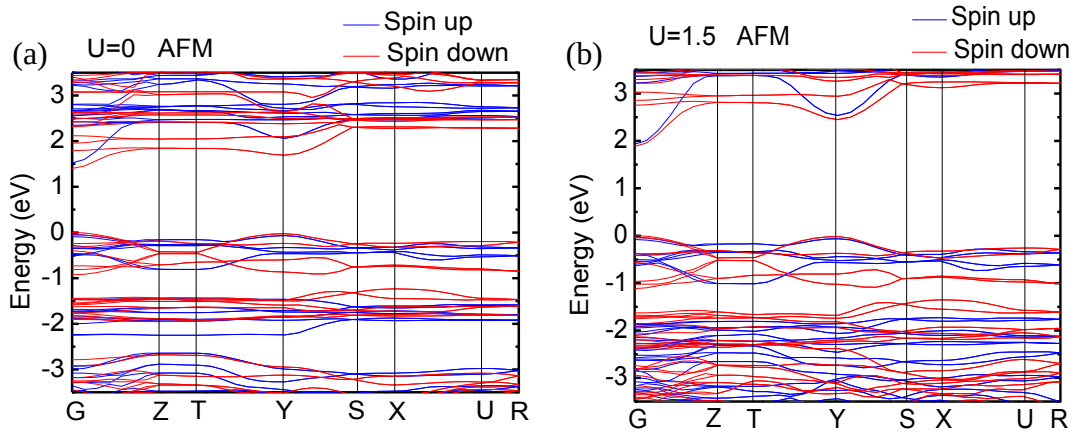

Figure 7.2 Electronic band structure of Mn_2SiO_4 in the AFM state for (a) U = 0 and (b) U = 1.5 eV. Zero energy denotes the top of the valence bands.

From the band structure of AFM Mn_2SiO_4 for (a) U = 0 and (b) U = 1.5 eV, as shown in Figure 7.2, we can observe that Mn_2SiO_4 has a band gap of about 1.0 eV for U = 0. Below the band gap we find two groups of narrow valence bands with widths of only 1.0 eV and 0.75 eV, respectively, which are separated from the broad lower valence bands by an additional gap of 0.50 eV. The conduction bands are pushed away from the valence bands, and the width of the band gap increases to 2.0 eV for U = 1.5 eV, which is compatible with the experimental results.[191]

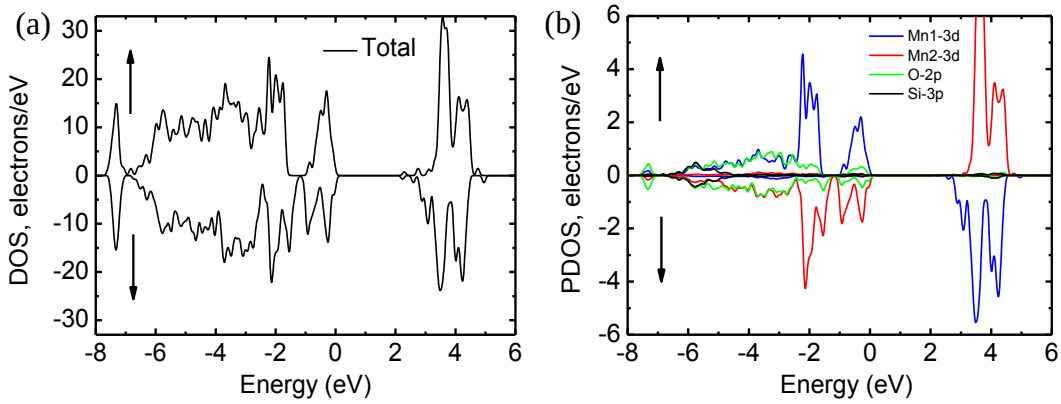

Figure 7.3 Total (a) and partial (b) densities of states of Mn_2SiO_4 for the AFM state at U = 1.5 eV.

The total and partial densities of states (DOS) of AFM Mn_2SiO_4 for U = 1.5 eV are given in Figure 7.3(a) and (b). As a result of the antiferromagnetic nature of the phase, the total DOS is nearly identical with respect to the spin-up and spin-down electrons, while the partial DOS (PDOS) of Mn1-3*d* and Mn2-3*d* are totally opposite. Due to the octahedral coordination, the Mn1-3*d* states in the crystal field are split into t_{2g} (lower) and e_g (higher) states. Both t_{2g} and e_g are only occupied by spin-up electrons, which results in the $t_{2g}^{\uparrow}$ and $e_g^{\uparrow}$ states being situated in the valence bands, while the $t_{2g}^{\downarrow}$and $e_g^{\downarrow}$ are located in conduction bands. The valence bands in spin-up

states of Mn1-3*d* clearly show two peaks, which correspond to the $t_{2g}^{\uparrow}$ (lower) and $e_g^{\uparrow}$ (higher) states, respectively. The splitting between the $t_{2g}^{\uparrow}$ and $e_g^{\uparrow}$ states is 0.5 eV. The valence bands are constituted from Mn (3*d*) – O (2*p*) hybridization. The conduction bands originate mainly from the Mn (3*d*) orbitals, where the lower energy conduction bands below about 5 eV are attributed mainly to the Mn (t_{2g}) orbitals.

The band structure of FM Mn_2SiO_4, shown in Figure 7.4(a), also shows a direct gap of about 1.0 eV at the G point for U = 0. We identify three groups of bands. Below the band gap, two narrow valence bands with widths of 1.2 eV and 0.9 eV, respectively, are separated by an additional gap of 0.5 eV. Remarkably, both of the two valence bands are occupied only by spin-up electrons. Above the band gap, there are wide conduction bands starting from 1.0 eV that are mainly occupied by spin-down electrons. This implies that when the electrons are excited from the valence bands to the conduction bands near the Fermi level, the holes will be fully polarized with spin-up orientation.

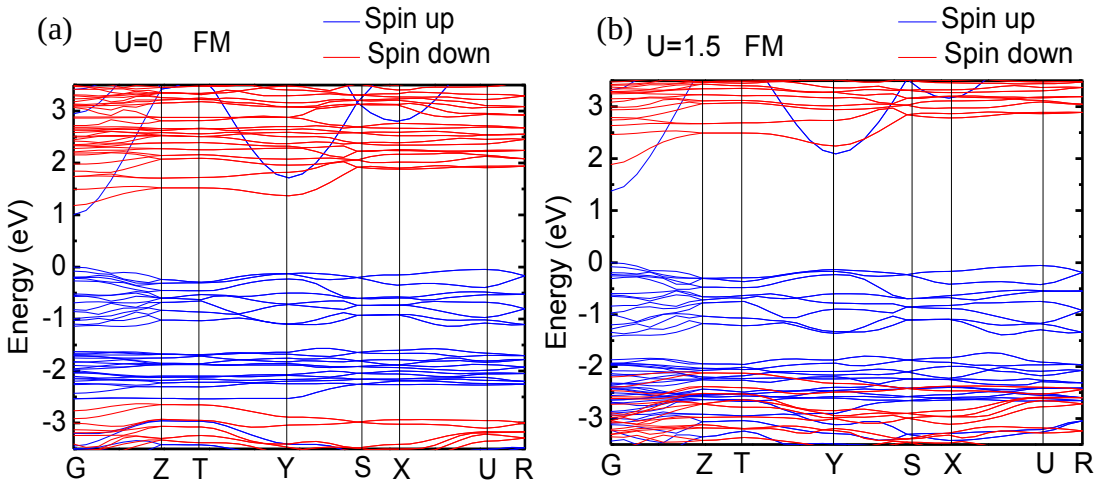

Figure 7.4 Electronic band structure of Mn_2SiO_4 in the FM state for (a) U = 0 and (b) U = 1.5 eV. Zero energy denotes the top of the valence bands.

As U = 1.5 eV is applied, as shown in Figure 7.4(b), the spin-down electrons in both the valence bands and the conduction bands near Fermi level are pushed towards higher energy states. The spin-down electrons in the valence bands move towards the Fermi level, reducing the energy range of the valence bands with unique spin-up electrons. Meanwhile, the conduction bands are pushed away from the Fermi level, making the width of the direct band gap increase to 1.4 eV. As the electrons near the Fermi level become excited, both the holes and the free electrons are fully polarized with spin-up orientation, which is valuable for optical study.

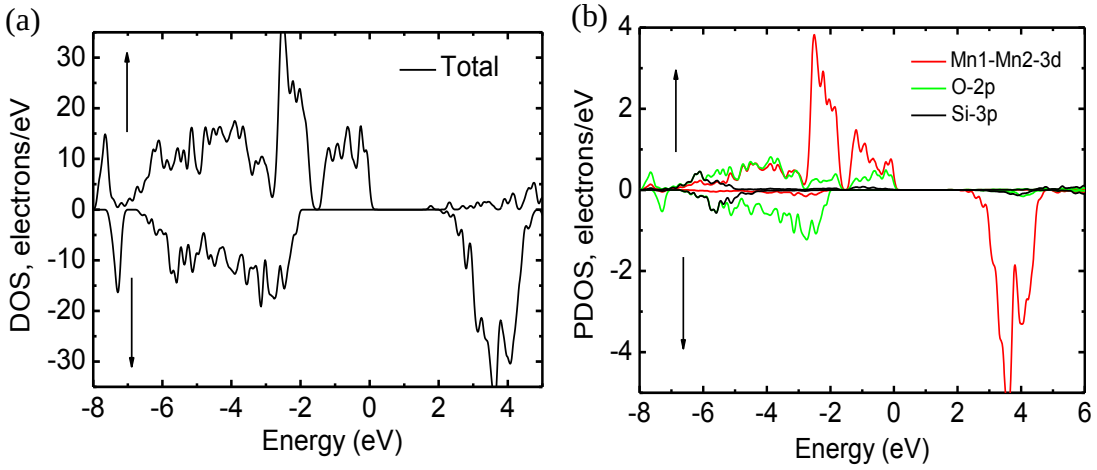

Figure 7.5 Total (a) and partial (b) densities of states of Mn_2SiO_4 for the FM state at U = 1.5 eV.

According to the DOS of FM Mn_2SiO_4, as shown in Figure 7.5, we can see that the spin-up electrons and spin-down electrons are not symmetrical near the Fermi level. The valence bands with only spin-up electrons from -2.0 − 0 eV are mainly composed of Mn-3*d* states with a certain contribution of O-2*p* states. The conduction bands having only spin-down electrons centred at around 2.6 eV are dominated by Mn-3*d* states. The Mn1-3*d* and Mn2-3*d* states have the same density of states, which

is similar to the case of of Mn1-3*d* in the AFM state, as shown in Figure 7.3(b). The valence bands are constituted by the hybridization of Mn-3*d* and O-2*p* states, and the contribution of the Si-3*p* states is still quite small.

7.3.2 Co_2SiO_4

The band structure of Co_2SiO_4 in the antiferromagnetic phase that was obtained by GGA calculations is shown in Figure 7.6(a). The calculations predict a metallic ground state, contrary to the insulating state found in experimental work. In Figure 7.6(b), the AFM band structure calculated by the GGA+*U* method gives more reasonable results. The valence band maximum and the conduction band minimum are both located at the G point, and hence, a direct gap of 2.0 eV is formed, which is consistent with the optical gap obtained from experimental work.[192]

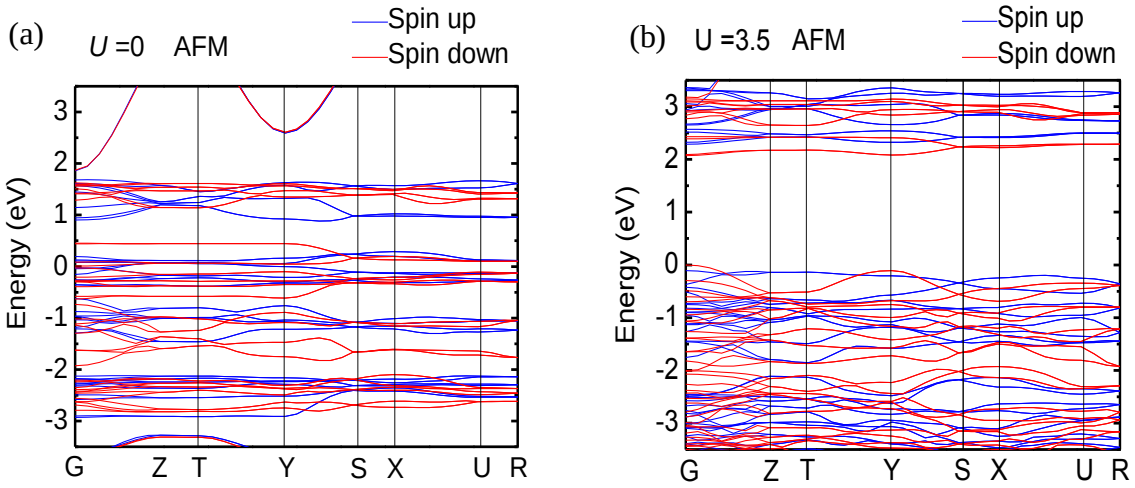

Figure 7.6 Electronic band structure of Co_2SiO_4 in the AFM state for (a) U = 0 and (b) U = 3.5 eV. Zero energy denotes the top of the valence bands

The total and partial DOS in the energy range around the gap are displayed in Figure 7.7. From the DOS of Co_2SiO_4, we can see that the valence bands (VB) and conduction bands (CB) around the Fermi energy are mainly composed of Co-3*d* states with a certain O-2*p* contribution. In the valence band, the Co-3*d* states and O-2*p* states are energetically degenerate, indicating the strong hybridization between them and the covalent characteristics of Co-O bonding. Due to the octahedral coordination, the Co1-3*d* states are divided into t_{2g} and e_g manifolds. The valence bands of Co1-3*d* are made up of the filled $t_{2g}^{\uparrow}$ and $e_g^{\uparrow}$ states and partially filled $t_{2g}^{\downarrow}$ states. The splitting between $t_{2g}^{\uparrow}$ and $e_g^{\uparrow}$ states is 0.4 eV. The conduction bands of Co1-3*d* start from 2.0 eV and show two peaks, which correspond to the partially unoccupied $t_{2g}^{\downarrow}$ and unoccupied $e_g^{\downarrow}$ states. The DOS of Co2-3*d* is opposite to that of Co1-3*d*, due to the antiferromagnetic nature of the phase.

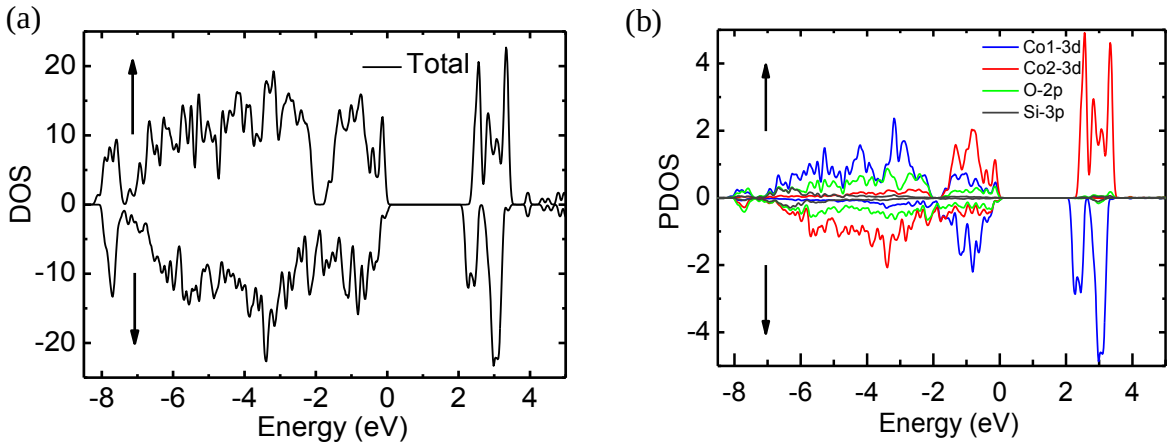

Figure 7.7 Total (a) and partial (b) densities of states for the AFM state at U = 3.5 eV.

The ferromagnetic band structure of Co_2SiO_4 calculated by GGA also shows a metallic state in Figure 7.8(a). The result is improved when the Coulomb interaction U is considered, as shown in Figure 7.8(b). When U = 3.5 eV, a band gap between the

top valence band and the bottom conduction band is formed with a direct gap at the G point. All the electrons in the conduction band have spin-down orientation, which means that any electrons excited from the valence bands to the conduction bands will be fully polarized.

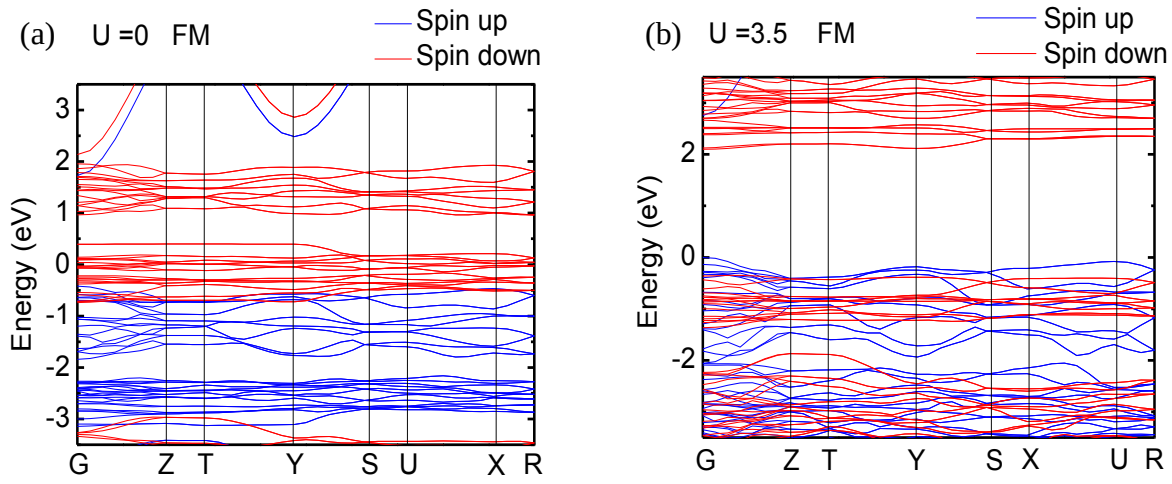

Figure 7.8 Electronic band structure of Co_2SiO_4 in the FM state for (a) U = 0 and (b) U = 3.5 eV. Zero energy denotes the top of the valence bands.

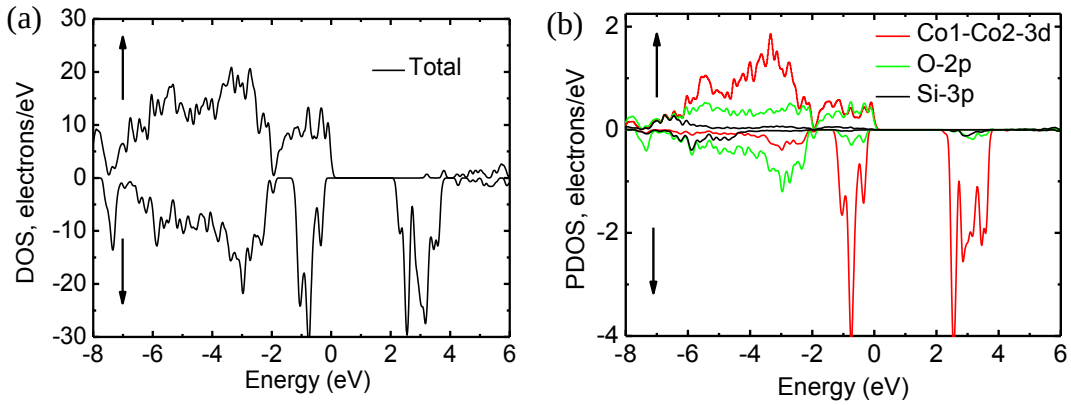

Figure 7.9 Total (a) and partial (b) densities of states for the FM state at U = 3.5 eV.

The reason can be explained by the density of states depicted in Figure 7.9 which shows that only the electrons with spin-down orientation appear in the conduction bands near the Fermi level. Because of the FM states, Co1 and Co2 have the same density of states. The five *d* orbitals, d_{xy}, d_{yz}, d_{xz}, $d_{x^2-y^2}$, and d_{z^2}, are fully occupied by electrons with spin-up orientations, which make up two peaks in the valence bands representing $t_{2g}^{\uparrow}$ and $e_g^{\uparrow}$ states, respectively. The spin-down electrons partially occupy the t_{2g} orbitals, which leaves the $e_g^{\downarrow}$ states and part of the $t_{2g}^{\uparrow}$ states in the conduction bands.

7.3.3 Ni_2SiO_4

Figure 7.10 presents the band structure of AFM Ni_2SiO_4 for (a) $U = 0$ and (b) $U = 4$ eV. Unlike Co_2SiO_4, a band gap of about 0.6 eV appears for $U = 0$. The gap then becomes bigger with increasing U.

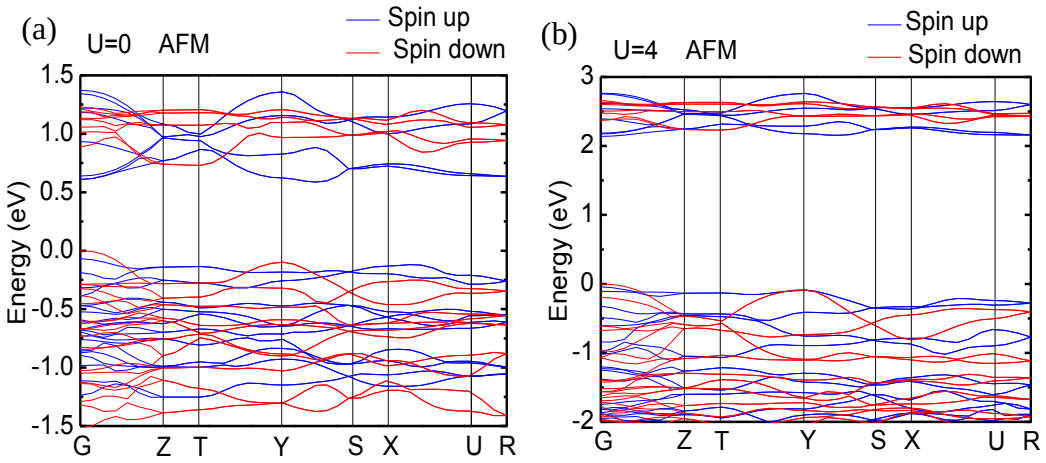

Figure 7.10 Electronic band structure of Ni_2SiO_4 in the AFM state for (a) $U = 0$ and (b) $U = 4$ eV. Zero energy denotes the top of the valence bands.

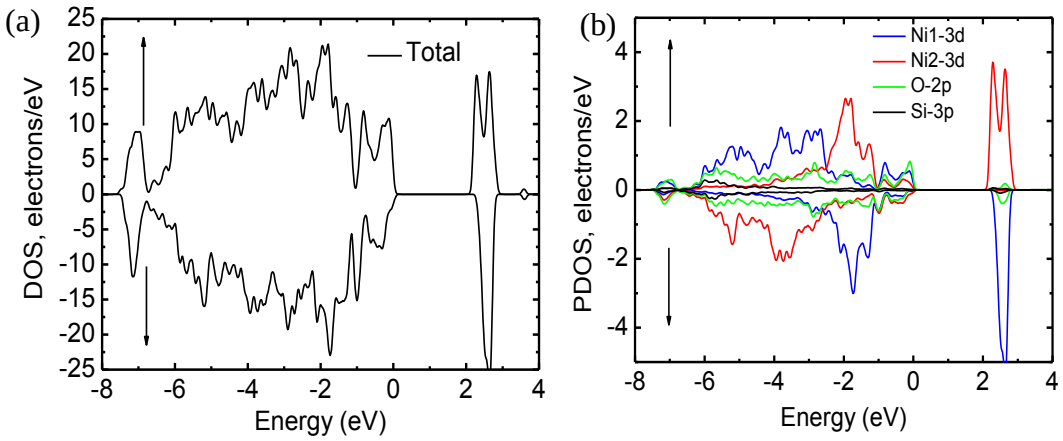

Figure 7.11 Total (a) and partial (b) densities of states of Ni_2SiO_4 for the AFM state at U = 4.0 eV.

The total and partial densities of states of AFM Ni_2SiO_4 for U = 4 eV are given in Figure 7.11(a) and (b). For the Ni1-3d states, both t_{2g} and e_g states are occupied by spin-up electrons in the valence bands, leading to $t_{2g}^{\uparrow}$ (-6.0 − -1.0 eV) and $e_g^{\uparrow}$ (-1.0 − 0 eV) states. The spin-down electrons only occupy t_{2g} states, and they contribute to the $t_{2g}^{\downarrow}$ states in the valence bands (-6.0 − 0 eV) and $e_g^{\downarrow}$ states in the conduction bands (centred at 2.7 eV). The partial DOS of Ni-3d mainly contributes to the valence bands from -6.0 – 0 eV, in which the Ni-3d states and O-2p states are hybridized, indicating the covalent characteristics of Ni-O bonding.

From Figure 7.12(a), we can see that the band structure of FM Ni_2SiO_4 has a direct gap of about 1 eV at the G point for U = 0. When U = 4 eV is applied, as shown in Figure 7.12(b), the band gap become 1 eV wider than in Figure 7.12(a). The spin-up electrons and spin-down electrons occupy the valence bands and conduction bands near the Fermi level, respectively, which implies that the holes and free electrons will be fully polarized with spin-up orientation and spin-down orientation, respectively, as the electrons are excited from valence bands to conduction bands.

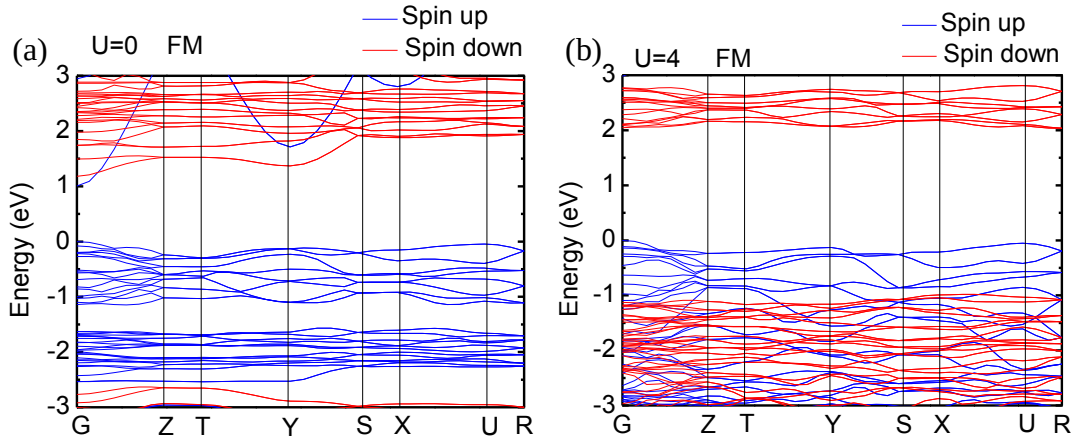

Figure 7.12 Electronic band structure of Ni_2SiO_4 in the FM state for (a) U = 0 and (b) U =4 .0 eV. Zero energy denotes the top of the valence bands.

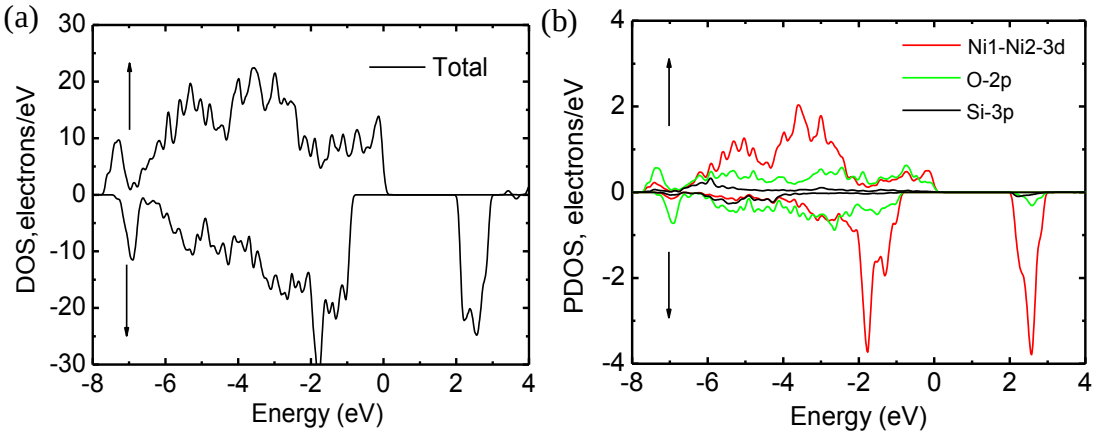

Figure 7.13 Total (a) and partial (b) densities of states of Ni_2SiO_4 for the FM state at U = 4.0 eV.

According to the DOS of FM Ni_2SiO_4, as shown in Figure 7.13, we can see that the spin-up electrons and spin-down electrons are not symmetrical near the Fermi level. The valence bands, with only spin-up electrons from -1.1 − 0 eV, are made up of Ni-3*d* and O-2*p* states. The conduction bands, having only spin-down electrons centred at around 2.6 eV, are dominated by Ni-3*d* states. The Ni1-3*d* and Ni2-3*d* states have the same density of states, which is similar to that of Ni1-3*d* in the AFM

phase, as shown in Figure 7.11(b). The valence bands are constituted by the hybridization of Ni-3*d* and O-2*p* states, and the contribution of the Si-3*p* states is still quite small.

7.4 Conclusions

First-principles calculations of the magnetic and electric properties of the olivines M_2SiO_4 (*M* = Mn, Co and Ni) have been performed using the CASTEP module of the Materials Studio package. The results of the GGA+*U* band-structure calculations for the M_2SiO_4 olivines predict antiferromagnetic insulating band characteristics. In the band structures, the conduction bands originate mainly from the *M*-3*d* orbitals of M_2SiO_4. The *M*-3*d* states and O-2*p* states are hybridized at the top of the valence bands in M_2SiO_4.

The *M*-3*d* states are split into t_{2g} and e_g states, due to octahedral coordination. The t_{2g} and e_g states are all fully occupied by spin-up electrons in the three compounds. The spin-down electrons do not take over any orbitals in Mn_2SiO_4, partially occupy the t_{2g} states in Co_2SiO_4, and fully occupy the t_{2g} states in Ni_2SiO_4.

In the FM band structure, the electrons are fully polarized with different spin orientations in both the valence bands and the conduction bands near the Fermi level. In Mn_2SiO_4, the holes and free electrons are fully polarized with spin-up orientation, as the electrons are excited, for U = 1.5 eV. In Co_2SiO_4, only the free electrons are fully polarized with spin-down orientation, as U = 3.5 eV is applied. In Ni_2SiO_4, the holes and free electrons are fully polarized with spin-up orientation and spin down orientation, respectively, for U = 4 eV.

CHAPTER 8. STUDY OF STEP-LIKE MAGNETIZATION OF A NEWLY DISCOVERED TRIANGULAR SYSTEM $Sr_3Co_2O_6$ USING MONTE CARLO SIMULATION

8.1 Introduction

Geometrically frustrated systems have attracted great attention for some time. The frustration in the system is mainly due to lattice topology and the presence of competing further–neighbour interaction. [196] Studies of frustration began with antiferromagnets, in which the lattices have triangular motifs and the nearest-neighbour interactions tend to anti-align spins. Frustration implies a conflict in minimizing the exchange interaction energies associated with different spin pairs, which produces highly degenerate ground states and enhances quantum fluctuation in a spin system, resulting in fascinating magnetic and transport properties related to the spin and structural frustration.[197] In recent years, some new magnetic materials with frustrated spin configurations have been discovered, which further aroused research interest in spin-frustrated systems.[198,199] One example, which has been studied for a long time, is $Cu_3(CO_3)_2(OH)_2$ with a one dimensional disordered diamond chain structure. The spin frustration in the system results in an abnormal response to magnetic field. Magnetization plateaus at M = 1/3 M_O (where M_O is the saturation magnetization) have been observed in magnetization curves, both theoretically and experimentally.[200,201]

Besides the $Cu_3(CO_3)_2(OH)_2$ compound, there's another family of compounds with frustrated spin configuration. These compounds have general formula A'_3ABO_6[202-205] (where A′ is Ca or Sr, while A and B are transition metal elements). As a member of this family, $Ca_3Co_2O_6$ has attracted much attention in the last decade. The crystalline electric fields lead to the presence of Co in chains with alternating high and low spin-states. Powder neutron diffraction revealed that the intrachain coupling (along the *c* axis) in $Ca_3Co_2O_6$ chains is ferromagnetic (FM), and the interchain coupling is antiferromagnetic (AFM) and much weaker than the intrachain coupling.[206] Consequently, the moments of spin chains preferentially align along the *c* axis, leading to a strong Ising-like anisotropy.[207-210] The chains form a triangular lattice in the *ab* plane that is perpendicular to the chains, causing geometrical frustration and exotic magnetism.

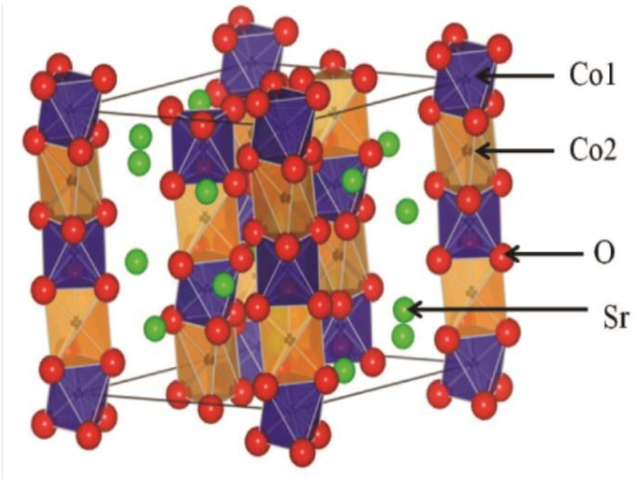

Figure 8.1 Schematic diagram of the crystal structure of $Sr_3Co_2O_6$.[211]

Another typical compound in the above-mentioned family is $Sr_3Co_2O_6$, which has been recently synthesized via a high-pressure and high-temperature method.[211] The

crystal structure of $Sr_3Co_2O_6$ determined by synchrotron X-ray powder diffraction is shown in Figure 8.1[211] $Sr_3Co_2O_6$ crystallizes in space group $\underline{R\text{-}3c}$ with Z = 6 (hexagonal), with lattice parameters a = 9.61107(4) Å and c = 10.70110(5) Å. As the structure parameters are comparable with those of $Ca_3Co_2O_6$,[212] the structure model for $Ca_3Co_2O_6$ is applicable to this compound. The crystal structure is made up of Co_2O_6 chains formed by alternating face-sharing Co_1O_6 octahedra and Co_2O_6 trigonal prisms along the c axis. Each chain is surrounded by six neighbouring chains, separated by Sr atoms, which form a triangular lattice in the *ab* plane.[213,214] The strong spin-orbital coupling implies that the Co spins have uniaxial magnetic properties.[210] The Weiss constant, Θ_W = +85(5) K, which is in accordance with the value reported for $Ca_3Co_2O_6$,[215] suggests that the major magnetic interaction is ferromagnetic (FM). Compared with the structure of $Ca_3Co_2O_6$, the unit-cell volume is expanded by 12.4%, as strontium cations rather than calcium cations are located between CoO_6 chains. The distance between intra-chain neighbouring Co_2 atoms, between the inter-chain nearest-neighbor Co_2 atoms, and between the inter-chain next-nearest-neighbour Co_2 atoms is increased by 2.2%, 0.92%, and 4.11%, respectively, compared to $Ca_3Co_2O_6$, resulting in decreased intra-chain and inter-chain interactions in the $Sr_3Co_2O_6$.

Experimental results[211] have shown that $Sr_3Co_2O_6$ has two transition temperatures, $T_{c1} \approx 22$ K and $T_{c2} \approx 9$ K, between which the magnetization curve has a magnetization plateau at one third of the full magnetization, which is likely caused by the frustrated magnetic state in this system. Below T_{c2}, the magnetization shows a multistep structure and hysteresis. A similar plateau was also observed for the analogous oxide $Ca_3Co_2O_6$,[210,215-227] and the microscopic magnetic origin of this phenomenon still needs further clarification. Comparing the magnetic properties of $Sr_3Co_2O_6$ with those of $Ca_3Co_2O_6$, small changes in the transition temperatures and

the width of the magnetization plateau were observed, which are due to the unit-cell difference. Therefore, study of the spin-chain compound $Sr_3Co_2O_6$ is important and helpful for understanding the microscopic origin of frustrated magnetic systems.

Motivated by the recent experimental observations on the compound $Sr_3Co_2O_6$, we have explored systematically the magnetic properties of two- and three-dimensional (2D and 3D) Ising models for a triangular spin-chain lattice in a magnetic field by Monte Carlo simulation and attempted to fit our results to experimental observations in a consistent manner. Our simulation presents $M(h)$ curves for different temperatures corresponding to the experiment. The spin configurations are used to explain the step-like magnetization behaviour in a quantitative sense. The effects of the interactions on the magnetic properties are used to explain the different experimental results for $Sr_3Co_2O_6$ and $Ca_3Co_2O_6$.

8.2 Monte Carlo Simulation on Ising Models

8.2.1 2D Ising Model with an AFM Interaction

According to previous investigations on the spin chain compound $Ca_3Co_2O_6$, strong Ising-like anisotropy is present, based on the structural characteristic that the intra-chain FM interaction is much stronger than the inter-chain AFM interaction. Each single spin chain can be treated as a rigid giant spin, and the structure of $Ca_3Co_2O_6$ can be regarded as a 2D triangular lattice in the *ab* plane.[222,223,227] We studied the magnetic properties of $Sr_3Co_2O_6$ using a 2D Ising model considering only inter-chain AFM interactions between each nearest-neighbour spin-chain pair, as presented in Figure 8.2. The Hamiltonian H, can be expressed as

$$H = -\sum_{[m,n]} JS_m^c S_n^c - h\mu_B g \sum_m S_m^c \tag{8.1}$$

where S^c_m is the effective spin-chain moment at the m^{th} site with the value of ±20; [*m*, *n*] denotes the summation over all the nearest-neighbouring pairs in the *ab* plane; $J = -3.542 \times 10^{-6}$ eV, representing the antiferromagnetic coupling; *h* denotes the external magnetic field. The values of the Lande factor and the Bohr magneton are $g = 2.5$ and $\mu_B = 5.788 \times 10^{-5}$(eV/T), respectively. The values of *J* and S^c_m are judged from quantitative comparison between experimental data and simulation results.

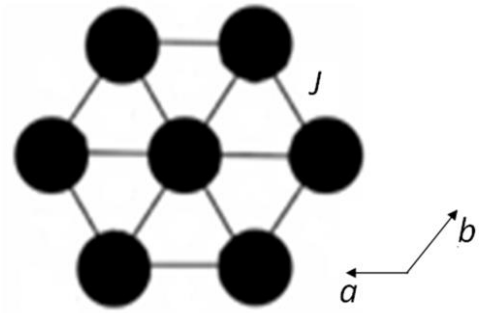

Figure 8.2 Schematic diagram of 2D triangular lattice in the *ab* plane. Black dots denote spin chains. Solid lines represent antiferromagnetic interactions between the nearest-neighbor spin chains.

The Monte Carlo simulation was performed in an L × L (L = 40) Ising triangular lattice with periodic boundary conditions. Each grid takes 50,000 Monte Carlo steps (MCS) to make the system reach equilibrium. We get the average value of each spin chain by averaging the value of the last 5,000 MCS, discarding the former 45,000 MCS. The procedure for the simulation is described as follows. At a given *T*, the simulation starts from the saturation field with a randomly chosen initial state. The standard Metropolis algorithm is employed to make the system reach equilibrium, and then the magnetization is evaluated on the basis of the balanced spin configuration.

After the magnetic field change $\triangle h$, the simulation is performed on the previous state to make the system reach a new equilibrium in the new magnetic field $h + \triangle h$. By repeating this process and averaging the data, we get the $M(h)$ curve at a given T.

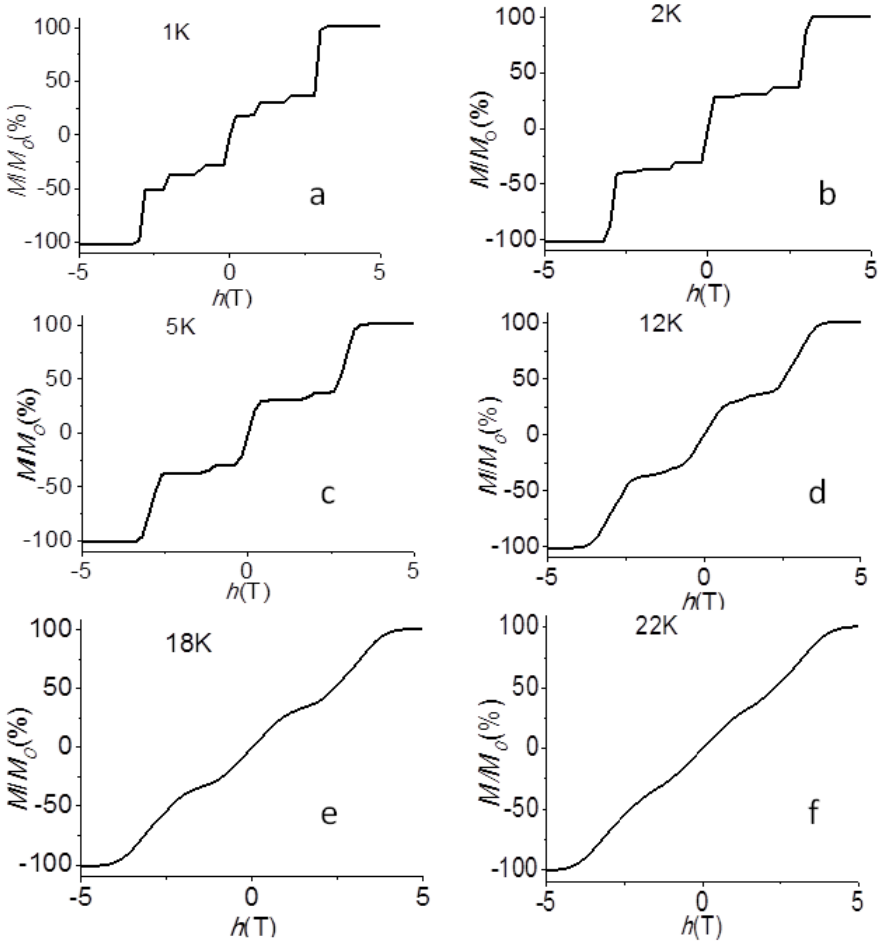

Figure 8.3 Magnetization curves of 2D Ising model for various T with J = -3.542 × 10^{-6} eV.

Figure 8.3 shows the simulated M with increasing h under various T. The magnetization curves change with different temperatures. There appears to be a multistep curve at T = 2K. Magnetization kinks at ～-3.0, -2.0,-1.0, 0, 1.0, 2.0, and 3.0 T, which are comparable to the experimental data (～0, 1.0, 2.2, and 3.8 T), show

six equidistant steps. The six steps become more obvious as T decreases down to 1 K. When T rises from 5 K to 18 K, the six steps combine into two magnetization plateaus with an approximate value of 1/3 of the saturated magnetization, M_O. By further increasing T, the magnetization plateaus become smaller and disappear finally because of the thermal activation, representing paramagnetic behaviour.

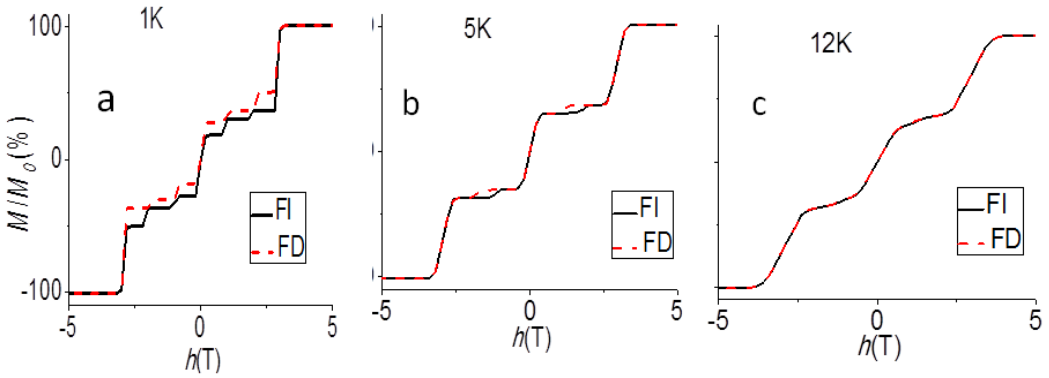

Figure 8.4 *M-h* dependence over a cycle of field increasing (FI) and then field decreasing (FD) at (a) 1 K, (b) 5 K, and (c) 12 K, respectively.

As revealed experimentally, the *M-h* loops at low temperatures are totally irreversible, while no hysteresis can be observed at high temperatures. Our simulation also presents this hysteretic feature, as shown in Figure 8.4. At 1 K, the hysteresis is at its most remarkable. As T increases, the hysteresis becomes weaker, as shown at 5 K. On further increasing T up to 12 K, no hysteresis can be found. From the hysteresis, we can judge that the steps appearing at 1 K are metastable states,[228] as their values are related to the initial states.

At 12 K, the magnetization promptly reaches the $1/3M_O$ plateau as h increases from zero, and then reaches the saturated magnetization when h rises to 3.8 T. To explain the peculiar phenomenon of the magnetization plateau, the corresponding spin configuration at 12 K is given in Figure 8.5. Red solid circles represent spin-up chains,

and the white ones denote spin-down chains. The magnetization shows a ferromagnetic structure. Two thirds of magnetic chains are spin up and one third of them are spin down. Each spin-down chain is surrounded by six spin-up chains due to the AFM interaction between the nearest-neighbour spins. The same spin chain configuration has also been reported in $Ca_3Co_2O_6$.

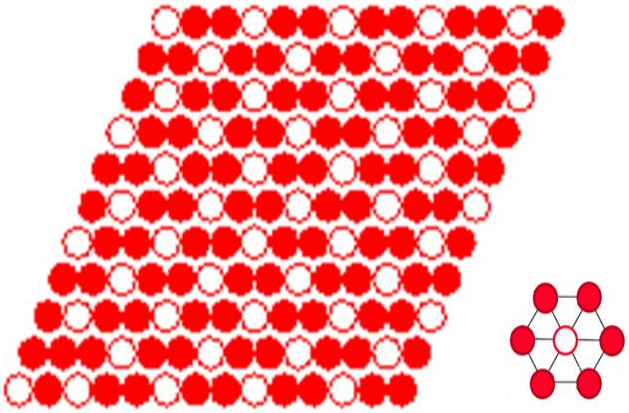

Figure 8.5 Corresponding spin configuration of 1/3M_O plateau for 2D Ising model at 12 K. Red solid circles represent spin-up chains, and the white ones denote spin-down chains.

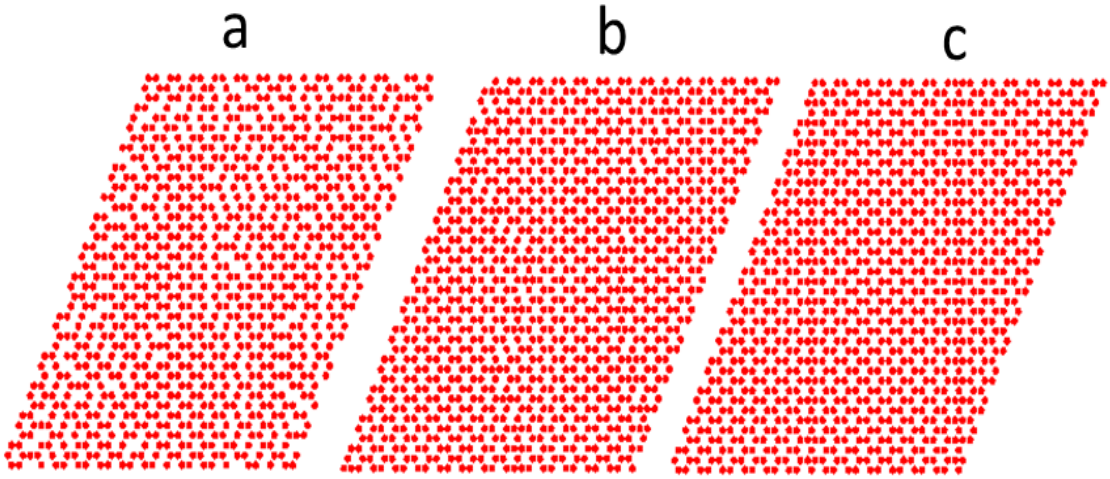

Figure 8.6 Spin configurations of 2D Ising model at 1 K, corresponding to three steps. (a) h = 0.6 T; (b) h = 1.6 T; (c) h = 2.6 T.

The magnetization presents a multistep structure between 1 and 5 K in agreement with experimental observations. At 1 K, as h increases from 0 to saturated field (3.2 T), three steps emerge at 21%M_O, 32%M_O, and 37%M_O, respectively, referred to as step (a), step (b), and step (c). These three steps have various spin configurations, as illustrated in Figure 8.6. For step(a), the spin configuration is composed of irregular spin-up or spin-down FM stripes and ferrimagnetically ordered regions. For step(b), the ferrimagnetically ordered regions aggregate at the expense of the irregular FM stripes. For step(c), the irregular FM stripes vanish completely, and the whole area of the remains ferrimagnetically ordered. It is noteworthy that new stripes appear, which are formed by two rows of ferromagnetically ordered regions with periodicity of ~20 a.

8.2.2 3D Ising Model with Three Exchange Interactions

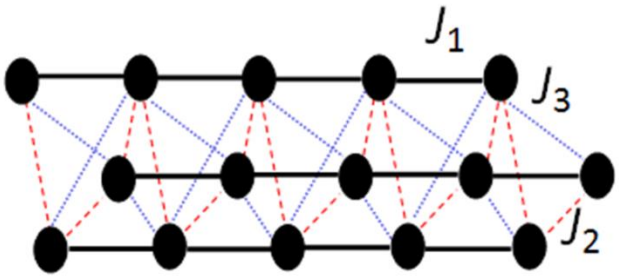

Figure 8.7 Schematic structure of trigonal prism unit of $Sr_3Co_2O_6$, Solid circles represent spin 2 coupled by exchange interactions J_1 (black solid lines) FM, J_2 (red dashed lines) AFM, and J_3 (blue dotted lines) AFM.

We also studied a model of the compound $Sr_3Co_2O_6$ for the 3D case. According to the spin states of $Ca_3Co_2O_6$, we assume that Co^{3+} ions have two kinds of spin state, the high-spin (S = 2) and the low-spin (S = 0) states, but only the ions in the high-spin

(S = 2) state contribute to the magnetic properties.[207,210,229] Consequently, S_m= ±2 is chosen in the present simulation. A schematic diagram of the three-dimensional prism unit of $Sr_3Co_2O_6$ is shown in Figure 8.7, in which three different spin interactions J_1, J_2, and J_3 ($J_1 > 0$, $J_{2,3} < 0$)are considered. Within the chains, the direct Co-Co overlap causes a strong FM intra-chain interaction, J_1; J_2 is the nearest-neighbour inter-chain AFM coupling; and the next nearest-neighbour inter-chain coupling is AFM type as well, namely, J_3, which is weaker than J_2.[219]

The Hamiltonian is given by

$$H = -\sum_{[m,k]} J_1 S_m S_k - \sum_{[m,l]} J_2 S_m S_l - \sum_{[m,n]} J_3 S_m S_n - h\mu_B g \sum_m S_m \qquad (8.2)$$

Where S_m is the spin moment at the m^{th} site; [m,k] stands for the summation over all the nearest-neighbouring pairs in the chain along the c axis; [m,l] represents the summation over all the nearest-neighbour pairs in the *ab* plane; [m,n] denotes the summation over all the next-nearest-neighbour pairs in the *ab* plane. J_i (i = 1, 2, 3) stands for the exchange interactions. The values of J_1, J_2, and J_3 are determined by a quantitative comparison between the simulated results and experimental data. The values of other parameters for the simulation resemble those for the 2D simulation The procedure for the simulation is similar to the earlier one for the 2D simulation, and a 3 × L × L × L (L = 30) lattice is employed.

Simulated M as a function of h at several temperatures is displayed in Figure 8.8, where h increases from the saturated magnetic field H = -5 T. The values of the three interactions are $J_1 = 2.635 \times 10^{-4}$ eV, $J_2 = -2.556 \times 10^{-5}$ eV, $J_3 = -2.045 \times 10^{-5}$ eV. The magnetization shows the multistep states at T = 5 K. The six steps are symmetrical from the zero point and equidistant. When T rises up to 12 K, two magnetization plateaus appear at around 1/3 of the saturated magnetization. On further increasing T

to 20 K, the magnetization increases linearly with *h*, indicating paramagnetic behaviour.

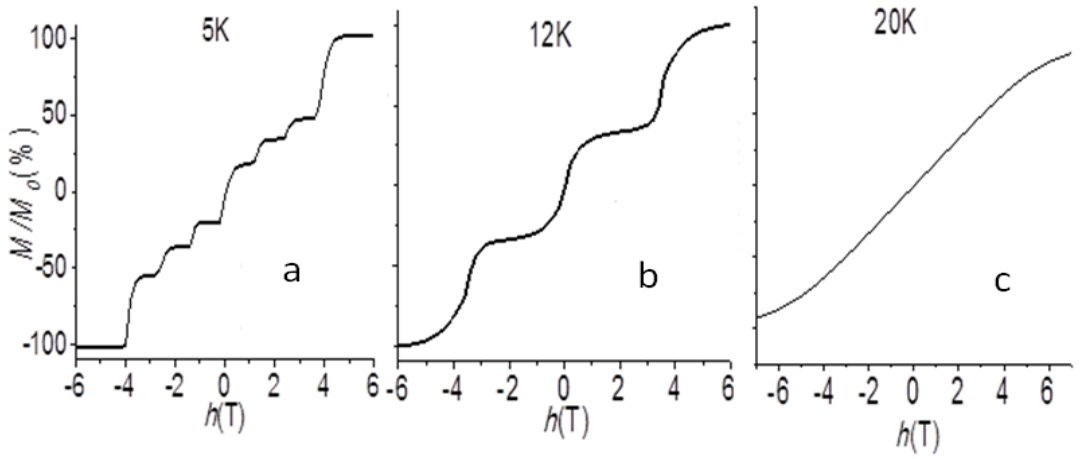

Figure 8.8 Magnetization curves of 3D spin-2 Ising model with $J_1 = 2.635 \times 10^{-4}$ eV, $J_2 = -2.556 \times 10^{-5}$ eV, $J_3 = -2.045 \times 10^{-5}$ eV, at (a) 5 K, (b) 12 K, and (c) 20 K.

To understand the appearance of the plateaus where $M = 1/3\ M_O$, the corresponding spin configurations are presented in Figure 8.9(a), showing the spin configuration of the compound $Sr_3Co_2O_6$ in the *ac* plane at $T = 12$ K for $h = 2.0$ T with $J_1 = 2.635 \times 10^{-4}$ eV, $J_2 = -2.556 \times 10^{-5}$ eV, $J_3 = -2.045 \times 10^{-5}$ eV. The red and blue solid circles represent spin up and spin down, respectively, with the spin up vectors directed along the positive direction of *h*. As the intra-chain FM interaction, J_1 is the strongest, and the spins of each chain connected by J_1 (such as Co-B1and Co-C1, or, Co-B2 and Co-C2) keep the same orientation. For the neighbouring spins (Co-B1, Co-B2, Co-C1, Co-C2) of spin Co-A, as the distance between Co-A and Co-B1 (or Co-B2) is shorter than that between Co-A and Co-C1 (or Co-C2), the inter-chain AFM interaction J_2 connecting Co-A and Co-B1 is stronger than J_3 which connects Co-A and Co-C1. As the effect of *h* is not strong enough, the Co-A spin orientation is

opposite to the orientation of its neighbouring spins due to the AFM interactions J_2 and J_3. Figure 8.9(a) also exhibits the results of spin frustration, in that the spin orientations of Co-B4 and Co-B1 (or Co-C1) are not opposite, although the exchange interaction between the two spins is antiferromagnetic. This configuration shows the ferrimagnetic structure where one of the three spin chains takes spin up, while the others take spin down, leading to the $M = 1/3M_O$ plateau.

In order to better understand the relationship between this peculiar plateau behaviour and the spin configurations, we present the spin configuration in the *ab* plane in Figure 8.9(b). The blue solid circles (such as Co-A, Co-A1, ⋯; Co-A4), which express spin down are situated in the same layer, supposed to be layer Y. Spin Co-A is surrounded by six up spins, indicated by red solid circles. Among the six up spins, the Co-B1, Co-B5, and Co-B7 spins are positioned in the same layer, denoted as layer X, which is above layer Y. The Co-B2, Co-B6, and Co-B8 spins are located in another layer, denoted as layer Z, below layer Y. All of these six spins are the nearest neighbours of spin Co-A, connected with spin Co-A by AFM J_2. Therefore, the spin orientations of these six spins are opposite to that of spin Co-A. The Co-B1 up spin belonging to layer X is surrounded by three up spins (Co-B4, Co-B6, Co-B8) belonging to layer Z and three down spins (Co-A, Co-A1, Co-A2) belonging to layer Y. As Co-A, Co-A1 and Co-A2 are nearest neighbours of Co-B1, and Co-B4, Co-B6, and Co-B8 are next-nearest neighbours of Co-B1. The J_2 interaction connecting Co-B1 with the former group is stronger than the J_3 interaction which connects Co-B1 with the latter group. Consequently, the orientations of the Co-A, Co-A1, and Co-A2 spins are opposite to the Co-B1 spin orientation due to the effect of AFM J_2, while the spin orientations of Co-B4, Co-B6, and Co-B8 remain same as the Co-B1 spin orientation in spite of AFM J_3, showing the results of spin frustration in the triangular

lattice. The plateau originates from the competition between the ferromagnetic and antiferromagnetic couplings, and the magnetic field.

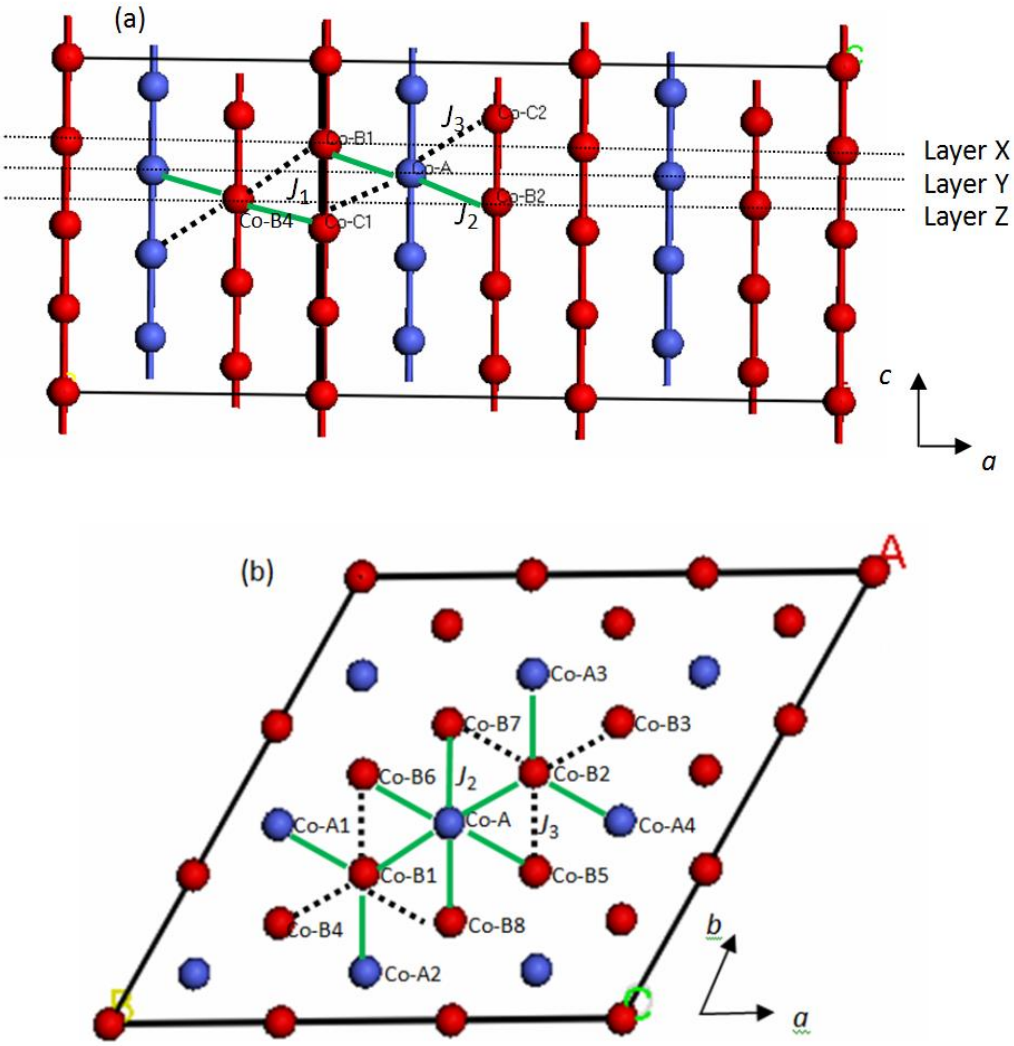

Figure 8.9 Spin configuration corresponding to 1/3 M_O plateau of 3D spin-2 Ising model with J_1 = 2.635 $\times 10^{-4}$ eV, J_2 = -2.556 $\times 10^{-5}$ eV, J_3 = -2.045 $\times 10^{-5}$ eV: (a) in the *ac* plane and (b) in the *ab* plane. The red and blue solid circles represent spin up and spin down, respectively. The black solid line represents the intrachain FM interaction J_1; the green solid line expresses the nearest-neighbouring interchain AFM interaction J_2; and the black dotted line denotes the next nearest-neighbouring interchain AFM interaction J_3.

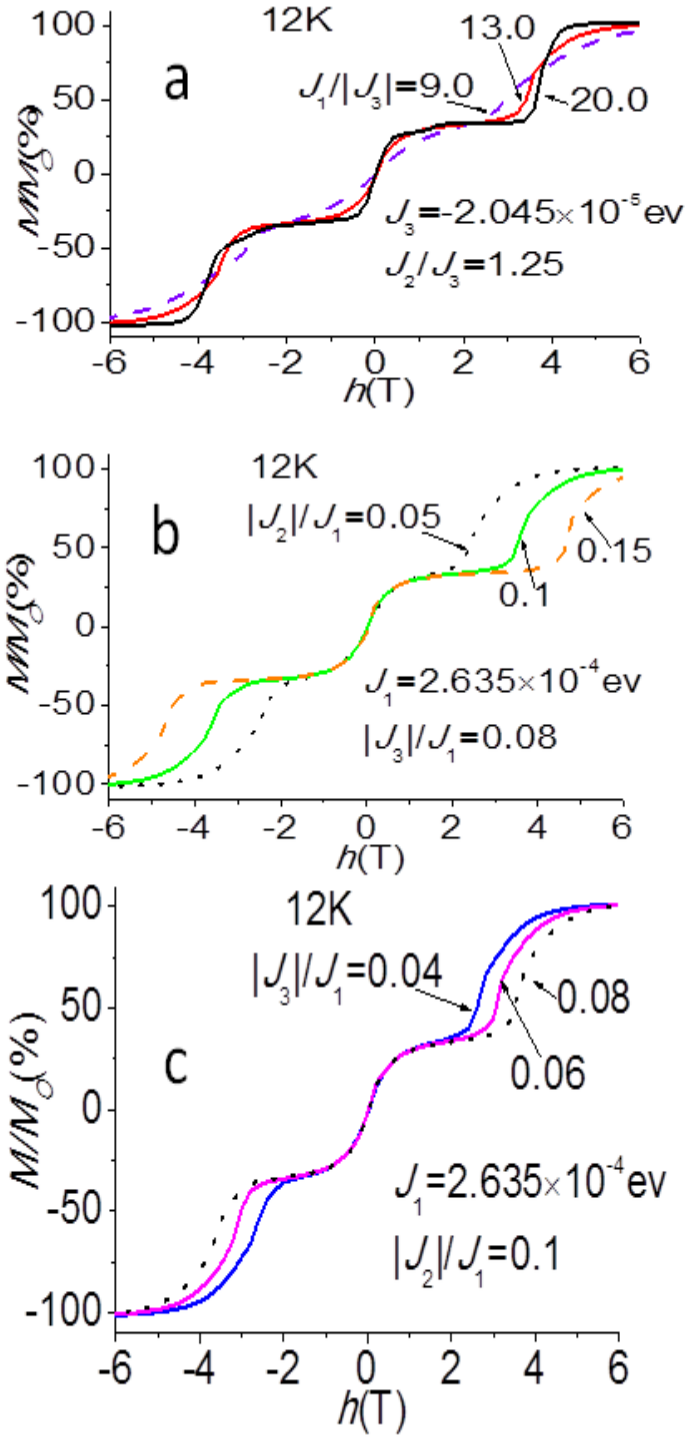

Figure 8.10 Magnetization curves of 3D spin-2 Ising model at temperature T = 12 K with (a) J_3 = -2.045 × 10^{-5} eV and J_2/J_3 = 1.25 for different J_1; (b) J_1 = -2.635 × 10^{-4} eV and $|J_3|/J_1$ = 0.08 for different J_2; and (c) J_1 = -2.635 × 10^{-4} eV and $J_2/|J_1|$ = 0.1 for different J_3.

The experimental data[211] on $Sr_3Co_2O_6$ at 12 K are compared with the results on $Ca_3Co_2O_6$. The width of the plateau in $Sr_3Co_2O_6$ is smaller than that in $Ca_3Co_2O_6$. This variation should be caused by the difference in size between Sr^{2+} (r = 1.12 Å) and Ca^{2+} (r = 0.99 Å), leading to the difference in the sizes of the unit cells for the two compounds. In $Sr_3Co_2O_6$, the distances are bigger between intra-chain neighbour Co2 atoms, between the inter-chain nearest neighbour Co2 atoms, and between the inter-chain next-nearest neighbour Co2 atoms, compared to the case in $Ca_3Co_2O_6$, resulting in the decreased J_1, J_2, and J_3 in $Sr_3Co_2O_6$.

In order to demonstrate that the width of the plateaus is somehow J dependent, we investigated the effects of the exchange interactions on the magnetic behaviour. Figure 8.10(a) shows the magnetization process at T = 12 K, with $J_3 = -2.045 \times 10^{-5}$ eV and $J_2/J_3 = 1.25$. It is clear that the magnetization exhibits different behaviour for different J_1. When $J_1/|J_3| = 9.0$, two $M = 1/3M_O$ plateaus appear in the magnetization curve. When J_1 becomes larger, the width of the two plateaus becomes wider. For Figure 8.10(b), the magnetization curves are presented at T = 12 K with different J_2, while J_1 and J_3 are fixed with $J_1 = -2.635 \times 10^{-4}$ eV and $J_3/|J_1| = 0.08$. It is observed that the larger the $|J_2|$ is, the wider is the width of the plateau. A similar situation appears in Figure 8.10(c), where J_1 and J_2 are fixed at $J_1 = -2.635 \times 10^{-5}$ eV and $J_2/|J_1| = 0.1$. The magnetization process with various J_3 at T = 12 K makes it manifest that the width of the plateau becomes larger with increasing $|J_3|$. The saturation field is obviously augmented with increasing AFM J_2 and J_3, while diminished with increasing FM J_1. Based on the above discussion, we can conclude that the width of the plateaus is J dependent. An increase in FM J_1 or AFM J_2 or J_3 can lead to greater width of the plateaus at the same temperature.

8.3 Conclusions

A two-dimensional Ising–like model for a triangular spin-chain lattice is proposed to study the magnetic properties of the spin-2 frustrated compound $Sr_3Co_2O_6$ by means of Monte Carlo simulation and make comparisons with experimental results.

The simulations show a multistep curve at T = 2 K, magnetization plateaus at M = 1/3M_O, with ferrimagnetic structure observed at T = 12 K. The plateaus become smaller and finally disappear with increasing temperature. It is observed that the multiple steps correspond to inhomogeneous spin configurations, while the M_O/3 plateau originates from a homogeneous ferrimagnetic structure. The magnetization curve for a cycle of field increasing and then decreasing is hysteretic at low T. The hysteresis becomes smaller with increasing T.

In order to investigate the differences in magnetic properties between $Sr_3Co_2O_6$ and $Ca_3Co_2O_6$, a three-dimensional Ising–like model was applied to study $Sr_3Co_2O_6$ compound. A strong intra-chain FM interaction, J_1, and two inter-chain AFM couplings, J_2 and J_3, are considered in the model. The simulation reproduces similar magnetic behaviour to that presented in the 2D Ising model, showing multistep behaviour at T = 5 K, magnetization plateaus at M = 1/3M_O with ferrimagnetic structure at T = 12 K, and paramagnetic behaviour at 20 K. The corresponding spin configurations are presented, which suggests that the plateau originates from the competition between the ferromagnetic and antiferromagnetic couplings and the magnetic field. The width of the plateau becomes larger as any one of the three interactions increases, explaining the plateau difference between $Sr_3Co_2O_6$ and $Ca_3Co_2O_6$.

CHAPTER 9. SUMMARY

This thesis is mainly focused on the functionalization of some monolayer honeycomb lattices, including graphene, silicene, germanene, and MoS_2, which have been studied on the basis of density functional theory (DFT) as implemented by the Vienna *ab-initio* simulation package (VASP) code.

The atomic structure of graphene is an sp^2 bonded planar lattice. Silicene and germanene have mixed sp^2-sp^3 buckled hexagonal structures. The electronic structure of silicene and germanene are similar to that of graphene, in that the bands cross linearly at the Fermi level with a zero band gap. Single-layer MoS_2 features a hexagonally packed layer composed of Mo atoms sandwiched between two layers of S atoms and was found to be a nonmagnetic semiconductor. The bands around the band gap are derived from the "Mo-*d*" electron states.

Under the inspiration of graphene allotropes, silicene allotropes, including octasilicene, silicyne, and silicdiyne, were constructed and investigated. They were all found to be buckled metallic materials.

In order to alter their metallic properties, various adatoms were introduced on the surface. The favorable adsorption position for a hydrogen atom on graphene is on top of a carbon atom. The H adatom pulls the bonded C atom out of the plane and creates a magnetic moment of 1 μ_B for graphene. Single F and O adatoms on graphene are adsorbed at the top site and bridge site, respectively, without any contribution of magnetic moment. The adsorption of a single H or O adatom on graphene transforms the system into a semiconductor.

Hydrogen atoms were introduced onto silicene allotropes to provide enough electrons to fill their unsatisfied valence shells and replace the dangling bonds with

valence bonds. Consequently, all the hydrogenated silicene allotropes appear to be semiconductors. The most stable type of adsorption suggests that the Si atom favors sp^3 hybridization.

For germanene, fluorine atoms were applied on the surface. Three configurations were considered for partially and fully fluorinated germanene. The chair-like structure is the most stable configuration for both cases. It fails to convert into a semiconductor, however. The band gap only appears in the boat-like and zigzag-like structures.

The O atom was used to study the functionalization of single-layer MoS_2. It has been proved that the single O atom can be stabilized on the hollow site in the Mo plane and on the site on top of an S atom. The site on top of an S atom is the most energetically favorable position, and adsorption of the oxygen atom on this site results in a direct gap. The adsorption of an O atom at the hollow site in the Mo plane results in the opening of a direct band gap at the M point. The DOS of the adsorption at this site demonstrates that the O atom forms a bond with the nearest S atom.

First-principles calculations of the olivines M_2SiO_4 (M = Mn, Co, and Ni) have been performed using the CASTEP module of the Materials Studio package. The results of the GGA+U band-structure calculations for the M_2SiO_4 olivines predict antiferromagnetic insulating band characteristics. The conduction bands originate mainly from the M-3d orbitals of M_2SiO_4. The M-3d states and O-2p states are hybridized at the top of the valence bands in M_2SiO_4. In the ferromagnetic (FM) band structure, the electrons are fully polarized with different spin orientations in the valence bands and the conduction bands near the Fermi level.

A two-dimensional Ising–like model for a triangular spin-chain lattice is proposed to study the magnetic properties of the spin-2 frustrated compound $Sr_3Co_2O_6$ by means of Monte Carlo simulation. The simulations show a multistep

curve at T = 2 K and magnetization plateaus at $M = 1/3M_O$ (where M_O is the saturated magnetization) at T = 12 K. The magnetization curve for a cycle of increasing and then decreasing field is hysteretic at low T. A three-dimensional Ising–like model is also applied to study $Sr_3Co_2O_6$ compound, which exhibits similar magnetic behaviour to that presented in the 2D Ising model. The width of the plateau becomes larger as any one of the three interactions increases, explaining the difference in the plateau between $Sr_3Co_2O_6$ and $Ca_3Co_2O_6$.

In the future, the challenges or issues for further discussion are listed as follows:

1) The adsorption of F or O atoms on silicene allotropes

2) The adsorption of an F or O atom on monolayer MoS_2 structure

3) The electronic properties of MoS_2 allotropes with structures similar to that of graphene allotropes.

REFERENCES

[1] K.S. Novoselov, A. K. Geim, S.V. Morozov, D. Jiang, Y. Zhang, S. V. Dubonos, I. V. Grigorieva, and A.A. Firsov, Science **306**, 666 (2004).

[2] K. S. Novoselov, D. Jiang, F. Schedin, T. J. Booth, V. V. Khotkevich, S. V. Morozov, and A. K. Geim, PNAS **102**, 10451 (2005).

[3] A. H. Castro Neto, F. Guinea, N. M. R. Peres, K. S. Novoselov, and A. K. Geim, Rev. Mod. Phys. **81**, 109 (2009).

[4] A. H. Castro Neto, F. Guinea, and N. M. R. Peres, Phys. World **19,** 33 (2006).

[5] W. Andreoni, The Physics of Fullerene-Based and Fullerene-Related Materials (Springer, Berlin) (2000).

[6] J.-C. Charlier, X. Blase, and S. Roche, Rev. Mod. Phys. **79**, 677 (2007).

[7] R. Saito, G. Dresselhaus, and M. S. Dresselhaus, Physical Properties of Carbon Nanotubes (Imperial College Press, London) (1998).

[8] H. Petroski, *The Pencil: A History of Design and Circumstance* (Knopf: Distributed by Random House, New York, 1990).

[9] L. A. Girifalco and R. A. Lad, J. Chem. Phys. **25,** 693 (1956).

[10] S. Viola Kusminskiy, D. K. Campbell, and A. H. Castro Neto, Phys. Rev. B **80** 035401 (2009).

[11] M. I. Katsnelson, K. S. Novoselov, and A. K. Geim, Nat. Phys. **2,** 620 (2006).

[12] V. P. Gusynin and S. G. Sharapov, Phys. Rev. Lett. **95**, 146801 (2005).

[13] N. M. R. Peres, F. Guinea, and A. H. Castro Neto, Phys. Rev. B **73**, 125411 (2006).

[14] K. S. Novoselov, A. K. Geim, S. V. Morozov, D. Jiang, M. I. Katsnelson, I. V. Grigorieva, S. V. Dubonos, and A. A. Firsov, Nature **438**, 197 (2005).

[15] Y. Zhang, Y.-W. Tan, H. L. Stormer, and P. Kim, Nature **438**, 201 (2005).

[16] K. S. Novoselov, Z. Jiang, Y. Zhang, S. V. Morozov, H. L. Stormer, U. Zeitler, J. C. Maan, G. S. Boebinger, P. Kim, and A. K. Geim, Science **315**, 1379 (2007).

[17] J.-C. Charlier, P.C. Eklund, J. Zhu, and A.C. Ferrari, in Carbon Nanotubes (Springer Berlin Heidelberg, 2008), pp. 673–709.

[18] A. Trisetyarso, Quantum Info. Comput. **12**, 989 (2012).

[19] C. Lee, X. Wei, J.W. Kysar, and J. Hone, Science **321**, 385 (2008).

[20] A. A. Balandin, S. Ghosh, W. Bao, I. Calizo, D. Teweldebrhan, F. Miao, and C. N. Lau, Nano Lett. **8**, 902 (2008).

[21] M. D. Stoller, S. Park, Y. Zhu, J. An, and R. S. Ruoff, Nano Lett. **8**, 3498 (2008).

[22] G. Eda, G. Fanchini, and M. Chhowalla, Nat. Nano. **3**, 270 (2008).

[23] N. Tombros, C. Jozsa, M. Popinciuc, H. T. Jonkman, and B. J. van Wees, Nature **448**, 571 (2007).

[24] S. Cho, Y.-F. Chen, and M. S. Fuhrer, Applied Physics Letters **91**, 123105 (2007).

[25] S. Park and R. S. Ruoff, Nat. Nano. **4**, 217 (2009).

[26] V. C. Tung, M. J. Allen, Y. Yang, and R. B. Kaner, Nat. Nano. **4**, 25 (2009).

[27] J. Hass, W. A. de Heer, and E. H. Conrad, J. Phys.: Condens. Matter **20**, 323202 (2008).

[28] K. S. Kim, Y. Zhao, H. Jang, S. Y. Lee, J. M. Kim, J. H. Ahn, P. Kim, J. Y. Choi, and B. H. Hong, Nature (London) **457**, 706 (2009).

[29] F. Schedin, A. K. Geim, S. V. Morozov, E. W. Hill, P. Blake, M. I. Katsnelson, and K. S. Novosolov, Nat. Materials **6**, 652 (2007).

[30] E. Durgun, S. Tongay, and S. Ciraci, Phys. Rev. B **72**, 075420 (2005).

[31] S. Cahangirov, M. Topsakal, E. Aktürk, H. Şahin, and S. Ciraci, Phys. Rev. Lett. **102**, 236804 (2009).

[32] L. C. L. Y. Voon, E. Sandberg, R. S. Aga, and A. A. Farajian, Applied Physics Letters **97**, 163114 (2010).

[33] G. G. Guzmán-Verri and L. C. Lew Yan Voon, Phys. Rev. B **76**, 075131 (2007).

[34] S. Q. Wang, Phys. Chem. Chem. Phys. **13**, 11929 (2011).

[35] C.-C. Liu, W. Feng, and Y. Yao, Phys. Rev. Lett. **107**, 076802 (2011).

[36] S. Lebègue and O. Eriksson, Phys. Rev. B **79**, 115409 (2009).

[37] M. Houssa, G. Pourtois, V. V. Afanas'ev, and A. Stesmans, Applied Physics Letters **96**, 082111 (2010).

[38] M. Houssa, G. Pourtois, V. V. Afanas'ev, and A. Stesmans, Applied Physics Letters **97**, 112106 (2010).

[39] P. D. Padova, C. Quaresima, B. Olivieri, P. Perfetti, and G. L. Lay, Applied Physics Letters **98**, 081909 (2011).

[40] C. Leandri, G. Le Lay, B. Aufray, C. Girardeaux, J. Avila, M. E. Dávila, M. C. Asensio, C. Ottaviani, and A. Cricenti, Surf. Sci. **574**, L9 (2005).

[41] P.D. Padova, C. Quaresima, C. Ottaviani, P. M. Sheverdyaeva, P. Moras, C. Carbone, D. Topwal, B. Olivieri, A. Kara, H. Oughaddou, B. Aufray, and G. L. Lay, Applied Physics Letters **96**, 261905 (2010).

[42] B. Lalmi, H. Oughaddou, H. Enriquez, A. Kara, S. Vizzini, B. Ealet, and B. Aufray, Applied Physics Letters **97**, 223109 (2010).

[43] H. Jamgotchian, Y. Colignon, N. Hamzaoui, B. Ealet, J. Y. Hoarau, B. Aufray, and J. P. Bibérian, J. Phys.: Condens. Matter **24**, 172001 (2012).

[44] H. Enriquez, S. Vizzini, A. Kara, B. Lalmi, and H. Oughaddou, J. Phys.: Condens. Matter **24**, 314211 (2012).

[45] P. Vogt, P. De Padova, C. Quaresima, J. Avila, E. Frantzeskakis, M.C. Asensio, A. Resta, B. Ealet, and G. Le Lay, Phys. Rev. Lett. **108**, 155501 (2012).

[46] B. Feng, Z. Ding, S. Meng, Y. Yao, X. He, P. Cheng, L. Chen, and K. Wu, Nano Lett. **12**, 3507 (2012).

[47] A. Fleurence, R. Friedlein, T. Ozaki, H. Kawai, Y. Wang, and Y. Yamada-Takamura, Phys. Rev. Lett. **108**, 245501 (2012).

[48] D. Chiappe, C. Grazianetti, G. Tallarida, M. Fanciulli, and A. Molle, Advanced Materials **24**, 5088 (2012).

[49] H. Okamoto, Y. Sugiyama, and H. Nakano, Chemistry – A European Journal **17**, 9864 (2011).

[50] H. Nakano, T. Mitsuoka, M. Harada, K. Horibuchi, H. Nozaki, N. Takahashi, T. Nonaka, Y. Seno, and H. Nakamura, Angewandte Chemie **118**, 6451 (2006).

[51] H. Okamoto, Y. Kumai, Y. Sugiyama, T. Mitsuoka, K. Nakanishi, T. Ohta, H. Nozaki, S. Yamaguchi, S. Shirai, and H. Nakano, J. Am. Chem. Soc. **132**, 2710 (2010).

[52] Y. Sugiyama, H. Okamoto, T. Mitsuoka, T. Morikawa, K. Nakanishi, T. Ohta, and H. Nakano, J. Am. Chem. Soc. **132**, 5946 (2010).

[53] K. Takada, H. Sakurai, E. Takayama-Muromachi, F. Izumi, R. A. Dilanian, and T. Sasaki, Nature **422**, 53 (2003).

[54] T. Shishidou, A. J. Freeman, and R. Asahi, Phys. Rev. B **64**, 180401 (2001).

[55] R. L. Withers and J. A. Wilson, J. Phys. C: Solid State Phys. **19**, 4809 (1986).

[56] A. B. Laursen, S. Kegnæs, S. Dahl, and I. Chorkendorff, Energy Environ. Sci. **5**, 5577 (2012).

[57] C. Lee, Q. Li, W. Kalb, X.-Z. Liu, H. Berger, R. W. Carpick, and J. Hone, Science **328**, 76 (2010).

[58] J. Feng, X. Sun, C. Wu, L. Peng, C. Lin, S. Hu, J. Yang, and Y. Xie, J. Am. Chem. Soc. **133**, 17832 (2011).

[59] J. Puthussery, S. Seefeld, N. Berry, M. Gibbs, and M. Law, J. Am. Chem. Soc. **133**, 716 (2011).

[60] S. Ding, D. Zhang, J. S. Chen, and X. W. (David) Lou, Nanoscale **4**, 95 (2011).

[61] J. A. Wilson and A. D. Yoffe, Advances in Physics **18**, 193 (1969).

[62] T. Todorova, R. Prins, and T. Weber, Journal of Catalysis **246**, 109 (2007).

[63] Y. Li, H. Wang, L. Xie, Y. Liang, G. Hong, and H. Dai, J. Am. Chem. Soc. **133**, 7296 (2011).

[64] E. Fortin and W. M. Sears, Journal of Physics and Chemistry of Solids **43**, 881 (1982).

[65] E. Gourmelon, O. Lignier, H. Hadouda, G. Couturier, J. C. Bernède, J. Tedd, J. Pouzet, and J. Salardenne, Solar Energy Materials and Solar Cells **46**, 115 (1997).

[66] M. Remskar, A. Mrzel, Z. Skraba, A. Jesih, M. Ceh, J. Demšar, P. Stadelmann, F. Lévy, and D. Mihailovic, Science **292**, 479 (2001).

[67] S. Helveg, J. V. Lauritsen, E. Lægsgaard, I. Stensgaard, J. K. Nørskov, B. S. Clausen, H. Topsøe, and F. Besenbacher, Phys. Rev. Lett. **84**, 951 (2000).

[68] K. Dolui, C. D. Pemmaraju, and S. Sanvito, ACS Nano **6**, 4823 (2012).

[69] A. Splendiani, L. Sun, Y. Zhang, T. Li, J. Kim, C.-Y. Chim, G. Galli, and F. Wang, Nano Lett. **10**, 1271 (2010).

[70] T. Korn, S. Heydrich, M. Hirmer, J. Schmutzler, and C. Schüller, Applied Physics Letters **99**, 102109 (2011).

[71] K. F. Mak, C. Lee, J. Hone, J. Shan, and T. F. Heinz, Phys. Rev. Lett. **105**, 136805 (2010).

[72] A. Kuc, N. Zibouche, and T. Heine, Phys. Rev. B **83**, 245213 (2011).

[73] Y. Ma, Y. Dai, M. Guo, C. Niu, J. Lu, and B. Huang, Phys. Chem. Chem. Phys. **13**, 15546 (2011).

[74] T. Böker, R. Severin, A. Müller, C. Janowitz, R. Manzke, D. Voß, P. Krüger, A. Mazur, and J. Pollmann, Phys. Rev. B **64**, 235305 (2001).

[75] A. Klein, S. Tiefenbacher, V. Eyert, C. Pettenkofer, and W. Jaegermann, Phys. Rev. B **64**, 205416 (2001).

[76] A. Ramasubramaniam, D. Naveh, and E. Towe, Phys. Rev. B **84**, 205325 (2011).

[77] B. Radisavljevic, A. Radenovic, J. Brivio, V. Giacometti, and A. Kis, Nat. Nano. **6**, 147 (2011).

[78] J. N. Coleman, M. Lotya, A. O'Neill, S. D. Bergin, P. J. King, U. Khan, K. Young, A. Gaucher, S. De, R. J. Smith, I. V. Shvets, S. K. Arora, G. Stanton, H.-Y. Kim, K. Lee, G. T. Kim, G. S. Duesberg, T. Hallam, J. J. Boland, J. J. Wang, J. F. Donegan, J. C. Grunlan, G. Moriarty, A. Shmeliov, R. J. Nicholls, J. M. Perkins, E. M. Grieveson, K. Theuwissen, D. W. McComb, P. D. Nellist, and V. Nicolosi, Science **331**, 568 (2011).

[79] K.-G. Zhou, N.-N. Mao, H.-X. Wang, Y. Peng, and H.-L. Zhang, Angewandte Chemie, International Edition **50**, 10839 (2011).

[80] R. J. Smith, P. J. King, M. Lotya, C. Wirtz, U. Khan, S. De, A. O'Neill, G. S. Duesberg, J. C. Grunlan, G. Moriarty, J. Chen, J. Wang, A. I. Minett, V. Nicolosi, and J. N. Coleman, Advanced Materials **23**, 3944 (2011).

[81] G. Eda, H. Yamaguchi, D. Voiry, T. Fujita, M. Chen, and M. Chhowalla, Nano Lett. **11**, 5111 (2011).

[82] Z. Zeng, Z. Yin, X. Huang, H. Li, Q. He, G. Lu, F. Boey, and H. Zhang, Angewandte Chemie, International Edition **50**, 11093 (2011).

[83] S. Tongay, J. Zhou, C. Ataca, K. Lo, T. S. Matthews, J. Li, J. C. Grossman, and J. Wu, Nano Lett. **12**, 5576 (2012).

[84] M. Regula, C. Ballif, J. H. Moser, and F. Lévy, Thin Solid Films **280**, 67 (1996).

[85] J. S. Zabinski, M. S. Donley, S. V. Prasad, and N. T. McDevitt, Journal of Materials Science **29**, 4834 (1994).

[86] S. Balendhran, J. Z. Ou, M. Bhaskaran, S. Sriram, S. Ippolito, Z. Vasic, E. Kats, S. Bhargava, S. Zhuiykov, and K. Kalantar-zadeh, Nanoscale **4**, 461 (2012).

[87] D. Kim, D. Sun, W. Lu, Z. Cheng, Y. Zhu, D. Le, T. S. Rahman, and L. Bartels, Langmuir **27**, 11650 (2011).

[88] Y. Zhan, Z. Liu, S. Najmaei, P. M. Ajayan, and J. Lou, Small **8**, 966 (2012).

[89] Y.-H. Lee, X.-Q. Zhang, W. Zhang, M.-T. Chang, C.-T. Lin, K.-D. Chang, Y.-C. Yu, J. T.-W. Wang, C.-S. Chang, L.-J. Li, and T.-W. Lin, Advanced Materials **24**, 2320 (2012).

[90] K.-K. Liu, W. Zhang, Y.-H. Lee, Y.-C. Lin, M.-T. Chang, C.-Y. Su, C.-S. Chang, H. Li, Y. Shi, H. Zhang, C.-S. Lai, and L.-J. Li, Nano Lett. **12**, 1538 (2012).

[91] J. Kibsgaard, J. V. Lauritsen, E. Laegsgaard, B. S. Clausen, H. Topsøe, and F. Besenbacher, J. Am. Chem. Soc. **128**, 13950 (2006).

[92] K. Kobayashi and J. Yamauchi, Phys. Rev. B **51**, 17085 (1995).

[93] J. Seo, Y. Jun, S. Park, H. Nah, T. Moon, B. Park, J.-G. Kim, Y. J. Kim, and J. Cheon, Angewandte Chemie, International Edition **46**, 8828 (2007).

[94] C. Ataca, H. Şahin, and S. Ciraci, J. Phys. Chem. C **116**, 8983 (2012).

[95] N. V. Podberezskaya, S. A. Magarill, N. V. Pervukhina, and S. V. Borisov, Journal of Structural Chemistry **42**, 654 (2001).

[96] S. Bae, H. Kim, Y. Lee, X. Xu, J.-S. Park, Y. Zheng, J. Balakrishnan, T. Lei, H. Ri Kim, Y. I. Song, Y.-J. Kim, K. S. Kim, B. Özyilmaz, J.-H. Ahn, B. H. Hong, and S. Iijima, Nat. Nano. **5**, 574 (2010).

[97] T. Hesjedal, Appl. Phys. Lett. **98**, 133106 (2011).

[98] L. H. Thomas, Proc. Camb. Phil. Soc. **23**, 542 (1927).

[99] E. Fermi, Rend. Accad. Lincei **6**, 602 (1927).

[100] P. Hohenberg and W. Kohn, Phys. Rev. **136**, B684 (1964).

[101] C. Møller and M. S. Plesset, Phys. Rev. **46**, 618 (1934).

[102] J. Cizek, J. Chem. Phys. **45**, 4256 (1966).

[103] R. G. Parr, W. Yang, Density-Functional Theory of Atoms and Molecules, Oxford University Press (1989).

[104] R. M. Dreizler, E. K. U. Gross, Density Functional Theory, Springer-Verlag (1990).

[105] W. Kohn and L. J. Sham, Phys. Rev. **140**, A1133 (1965).

[106] D.M. Ceperley and B.J Alder, Phys. Rev. Lett. **45**, 566 (1980).

[107] J. P. Perdew, K. Burke and Y. Wang, Phys. Rev. B **54**, 16533 (1992).

[108] J. P. Perdew, K. Burke and M. Ernzerhof, Phys. Rev. Lett. **77**, 3865-3868 (1996).

[109] H. D. Monkhorst and J. D. Pack, Phys. Rev. B **13**, 5188 (1976).

[110] N. Troullier and J. L. Martins, Phys. Rev. B **43**, 1993 (1991).

[111] G. P. Kerker, J. Phys. C **13**, L189 (1980).

[112] D. R. Hamann, M. Schlüter and C. Chiang, Phys. Rev. Lett. **43**, 1494 (1979).

[113] D. Vanderbilt, Phys. Rev. B **32**, 8412 (1985).

[114] D. Vanderbilt, Phys. Rev. B **41**, 7892 (1990).

[115] P. E. Blöchl, Phys. Rev. B **50**, 17953 (1994).

[116] C. J. Pickard and F. Mauri, Phys. Rev. B **63**, 245101 (2001).

[117] H.J. Monkhorst and J.D. Pack, Phys. Rev. B **13**, 5188 (1976).

[118] G. Kresse and J. Hafner, Phys. Rev. B **49**, 14251 (1994).

[119] S. Casolo, R. Martinazzo, and G.F. Tantardini, J. Phys. Chem. C **115**, 3250 (2011).

[120] F. Schwierz, Nat Nano **5**, 487 (2010).

[121] D.C. Elias, R.R. Nair, T.M.G. Mohiuddin, S.V. Morozov, P. Blake, M.P. Halsall, A.C. Ferrari, D.W. Boukhvalov, M.I. Katsnelson, A.K. Geim, and K.S. Novoselov, Science **323**, 610 (2009).

[122] R. Balog, B. Jørgensen, L. Nilsson, M. Andersen, E. Rienks, M. Bianchi, M. Fanetti, E. Lægsgaard, A. Baraldi, S. Lizzit, Z. Sljivancanin, F. Besenbacher, B. Hammer, T.G. Pedersen, P. Hofmann, and L. Hornekær, Nat Mater **9**, 315 (2010).

[123] O.V. Yazyev, Rep. Prog. Phys. **73**, 056501 (2010).

[124] E.J. Duplock, M. Scheffler, and P.J.D. Lindan, Phys. Rev. Lett. **92**, 225502 (2004).

[125] D.W. Boukhvalov, M.I. Katsnelson, and A.I. Lichtenstein, Phys. Rev. B **77**, 035427 (2008).

[126] S. Casolo, O.M. Lovvik, R. Martinazzo, and G.F. Tantardini, The Journal of Chemical Physics **130**, 054704 (2009).

[127] M. Mirzadeh and M. Farjam, Journal of Physics: Condensed Matter **24**, 235304 (2012).

[128] H.W. Kroto, J.R. Heath, S.C. O'Brien, R.F. Curl, and R.E. Smalley, Nature **318**, 162 (1985).

[129] S. Iijima, Nature **354**, 56 (1991).

[130] V. I. Kasatochkin, A. M. Sladkov, Yu. P. Kudryavtsev, N. M. Popov, and V. V. Korshak, Dokl. Akad, Nauk SSSR **177**, 358 (1967).

[131] S. Tanuma, A. Palnichenko, and N. Satoh, Synth. Met. **71**, 1841 (1995).

[132] B.G. Kim and H.J. Choi, Physical Review B **86**, 115435 (2012).

[133] N. Narita, S. Nagai, S. Suzuki, and K. Nakao, Phys. Rev. B **58**, 11009 (1998).

[134] X.-L. Sheng, H.-J. Cui, F. Ye, Q.-B. Yan, Q.-R. Zheng, and G. Su, Journal of Applied Physics **112**, 4315 (2012).

[135] R. H. Baughman, H. Eckhardt, and M. Kertesz, J. Chem. Phys. **87**, 6687 (1987).

[136] H. Sahin and F.M. Peeters, Phys. Rev. B **87**, 085423 (2013).

[137] H. Şahin, S. Cahangirov, M. Topsakal, E. Bekaroglu, E. Akturk, R.T. Senger, and S. Ciraci, Phys. Rev. B **80**, 155453 (2009).

[138] M.J. Fink, M.J. Michalczyk, K.J. Haller, R. West, and J. Michl, J. Chem. Soc., Chem. Commun. 1010 (1983).

[139] A.K. Geim and K.S. Novoselov, Nat. Mater. **6**, 183 (2007).

[140] A.K. Geim, Science **324**, 1530 (2009).

[141] K.S. Novoselov, A.K. Geim, S.V. Morozov, D. Jiang, M.I. Katsnelson, I.V. Grigorieva, S.V. Dubonos, and A.A. Firsov, Nature **438**, 197 (2005).

[142] V.P. Gusynin and S.G. Sharapov, Phys. Rev. Lett. **95**, 146801 (2005).

[143] S. Chen, Q. Wu, C. Mishra, J. Kang, H. Zhang, K. Cho, W. Cai, A.A. Balandin, and R.S. Ruoff, Nat. Mater. **11**, 203 (2012).

[144] J.O. Sofo, A.S. Chaudhari, and G.D. Barber, Phys. Rev. B **75**, 153401 (2007).

[145] J.T. Robinson, J.S. Burgess, C.E. Junkermeier, S.C. Badescu, T.L. Reinecke, F.K. Perkins, M.K. Zalalutdniov, J.W. Baldwin, J.C. Culbertson, P.E. Sheehan, and E.S. Snow, Nano Lett. **10**, 3001 (2010).

[146] S.-H. Cheng, K. Zou, F. Okino, H.R. Gutierrez, A. Gupta, N. Shen, P.C. Eklund, J.O. Sofo, and J. Zhu, Phys. Rev. B **81**, 205435 (2010).

[147] D. Jose and A. Datta, Acc. Chem. Res. **47**, 593 (2014).

[148] W. Wei, Y. Dai, B. Huang, and T. Jacob, Phys. Chem. Chem. Phys. **15**, 8789 (2013).

[149] L. Chen, C.-C. Liu, B. Feng, X. He, P. Cheng, Z. Ding, S. Meng, Y. Yao, and K. Wu, Phys. Rev. Lett. **109**, 056804 (2012).

[150] L. Meng, Y. Wang, L. Zhang, S. Du, R. Wu, L. Li, Y. Zhang, G. Li, H. Zhou, W.A. Hofer, and H.-J. Gao, Nano Lett. **13**, 685 (2013).

[151] C.-C. Liu, H. Jiang, and Y. Yao, Phys. Rev. B **84**, 195430 (2011).

[152] M. Ezawa, Phys. Rev. Lett. **109**, 055502 (2012).

[153] M. Ezawa, New J. Phys. **14**, 033003 (2012).

[154] M. Houssa, E. Scalise, K. Sankaran, G. Pourtois, V.V. Afanas'ev, and A. Stesmans, Applied Physics Letters **98**, 3107 (2011).

[155] L.C. Lew Yan Voon, E. Sandberg, R.S. Aga, and A.A. Farajian, Applied Physics Letters **97**, 3114 (2010).

[156] J.C. Garcia, D.B. de Lima, L.V.C. Assali, and J.F. Justo, J. Phys. Chem. C **115**, 13242 (2011).

[157] Y. Ding and Y. Wang, Applied Physics Letters **100**, 083102 (2012).

[158] E. Bianco, S. Butler, S. Jiang, O.D. Restrepo, W. Windl, and J.E. Goldberger, ACS Nano **7**, 4414 (2013).

[159] Y. Ma, Y. Dai, C. Niu, and B. Huang, J. Mater. Chem. **22**, 12587 (2012).

[160] J. Sivek, H. Sahin, B. Partoens, and F.M. Peeters, Phys. Rev. B **87**, 085444 (2013).

[161] J.N. Coleman, M. Lotya, A. O'Neill, S.D. Bergin, P.J. King, U. Khan, K. Young, A. Gaucher, S. De, R.J. Smith, I.V. Shvets, S.K. Arora, G. Stanton, H.-Y. Kim, K. Lee, G.T. Kim, G.S. Duesberg, T. Hallam, J.J. Boland, J.J. Wang, J.F. Donegan, J.C. Grunlan, G. Moriarty, A. Shmeliov, R.J. Nicholls, J.M. Perkins, E.M. Grieveson, K. Theuwissen, D.W. McComb, P.D. Nellist, and V. Nicolosi, Science **331**, 568 (2011).

[162] Y. Li, Z. Zhou, S. Zhang, and Z. Chen, J. Am. Chem. Soc. **130**, 16739 (2008).

[163] C. Ataca, H. Şahin, E. Aktürk, and S. Ciraci, The Journal of Physical Chemistry C **115**, 3934 (2011).

[164] T. Liang, W.G. Sawyer, S.S. Perry, S.B. Sinnott, and S.R. Phillpot, Phys. Rev. B **77**, 104105 (2008).

[165] T. Onodera, Y. Morita, R. Nagumo, R. Miura, A. Suzuki, H. Tsuboi, N. Hatakeyama, A. Endou, H. Takaba, F. Dassenoy, C. Minfray, L. Joly-Pottuz, M. Kubo, J.-M. Martin, and A. Miyamoto, J. Phys. Chem. B **114**, 15832 (2010).

[166] H. Hölscher, D. Ebeling, and U.D. Schwarz, Phys. Rev. Lett. **101**, 246105 (2008).

[167] T.F. Jaramillo, K.P. Jørgensen, J. Bonde, J.H. Nielsen, S. Horch, and I. Chorkendorff, Science **317**, 100 (2007).

[168] J.P. Wilcoxon, T.R. Thurston, and J.E. Martin, Nanostructured Materials **12**, 993 (1999).

[169] G. Kline, K.K. Kam, R. Ziegler, and B.A. Parkinson, Solar Energy Materials **6**, 337 (1982).

[170] M. Sun, A.E. Nelson, and J. Adjaye, Journal of Catalysis **226**, 32 (2004).

[171] P.G. Moses, J.J. Mortensen, B.I. Lundqvist, and J.K. Norskov, The Journal of Chemical Physics **130**, 104709 (2009).

[172] J. He, K. Wu, R. Sa, Q. Li, and Y. Wei, Applied Physics Letters **96**, 082504 (2010).

[173] L.F. Mattheiss, Phys. Rev. Lett. **30**, 784 (1973).

[174] J. Brodholt, AM MINERAL **82**, 1049 (1997).

[175] R.L. Withers and J.A. Wilson, J. Phys. C: Solid State Phys. **19**, 4809 (1986).

[176] R. Rinaldi, G.D. Gatta, G. Artioli, K.S. Knight, and C.A. Geiger, Phys Chem Minerals **32**, 655 (2005).

[177] M. Wilke, F. Farges, P.-E. Petit, G.E. Brown, and F. Martin, American Mineralogist **86**, 714 (2001).

[178] A. Sazonov, V. Hutanu, M. Meven, G. Heger, T. Hansen, J. Appl. Cryst. **43**, 720-728 (2010).

[179] A. Sazonov, M. Meven, V. Hutanu, G. Heger, T. Hansen, A. Gukasov Acta Crystallographica. Section B, Structural Science **65**, 664 (2009).

[180] H. Kato, E. Untersteller, S. Hosoya, G. Kido, and W. Treutmann, Journal of Magnetism and Magnetic Materials **140–144, Part 3**, 1535 (1995).

[181] I.S. Hagemann, P.G. Khalifah, A.P. Ramirez, and R.J. Cava, Phys. Rev. B **62**, R771 (2000).

[182] M. Cococcioni, A. Dal Corso, and S. de Gironcoli, Phys. Rev. B **67**, 094106 (2003).

[183] X. Jiang and G.Y. Guo, Phys. Rev. B **69**, 155108 (2004).

[184] R.H. Colman, T. Fennell, C. Ritter, G. Lau, R.J. Cava, and A.S. Wills, J. Phys.: Conf. Ser. **145**, 012037 (2009).

[185] O. Ballet, H. Fuess, K. Wacker, E. Untersteller, W. Treutmann, E. Hellner, and S. Hosoya, J. Phys.: Condens. Matter **1**, 4955 (1989).

[186] M. Zbiri, T. Fennell, J.W. Taylor, M. Enderle, G.C. Lau, R.J. Cava, and M.R. Johnson, J. Phys.: Condens. Matter **20**, 285203 (2008).

[187] T. Hahn and International Union of Crystallography, *International Tables for Crystallography. Vol. A, Vol. A*, (Published for the International Union of Crystallography by Kluwer Academic Publishers, Dordrecht; London, 2002).

[188] M. Mochizuki and N. Furukawa, Phys. Rev. Lett. **105**, 187601 (2010).

[189] J.S. White, T. Honda, K. Kimura, T. Kimura, C. Niedermayer, O. Zaharko, A. Poole, B. Roessli, and M. Kenzelmann, Phys. Rev. Lett. **108**, 077204 (2012).

[190] M.D. Segall, P.J.D. Lindan, M.J. Probert, C.J. Pickard, P.J. Hasnip, S.J. Clark, and M.C. Payne, J. Phys.: Condens. Matter **14**, 2717 (2002).

[191] R.C. Powell, B. Elouadi, L. Xi, G.M. Loiacono, and R.S. Feigelson, Journal of Chemical Physics **84**, 657 (1986).

[192] M. Llusar, A. Forés, J.A. Badenes, J. Calbo, M.A. Tena, and G. Monrós, Journal of the European Ceramic Society **21**, 1121 (2001).

[193] S. Yamazaki, H. Toraya, J. Appl. Cryst. **32**, 51-59 (1999).

[194] A. Sazonov, M. Meven, V. Hutanu, V. Kaiser, G. Heger, D. Trots, and M. Merz, Acta Crystallographica Section B Structural Science **64**, 661 (2008).

[195] A. Sazonov, M. Meven, V. Hutanu, V. Kaiser, G. Heger, D. Trots, and M. Merz, Acta Crystallographica Section B Structural Science **64**, 661 (2008).

[196] L. Balents, Nature **464**,199 (2010).

[197] S. T. Bramwell and M. P. Gingras, Science **294**, 1495 (2001).

[198] K. Ueda and S. Miyahara, J. Phys.: Condens. Matter **11**, L175 (1999).

[199] M. Hase, I. Terasaki, and K. Uchinokura, Phys. Rev. Lett. **70**, 365 (1993).

[200] G. Bo and S. Gang. Phys. Rev. B **75**, 174437 (2007).

[201] H. Kikuchi, Y. Fujii, M. Chiba, S. Mitsudo, T. Idehara, T. Tonegawa, K. Okamoto, T. Sakai, T. Kuwai, and H. Ohta, Phys . Rev. Lett. **94**, 227201 (2005).

[202] S. Rayaprol, K. Sengupta, and E. V. Sampathkumaran, Solid State Commun. **128**, 79 (2003).

[203] R. Vidya, P. Ravindran, H. Fjellvag, A. Kjekshus, and O. Eriksson, Phys. Rev. Lett. **91**, 186404 (2003).

[204] E. V. Sampathkumaran and A. Niazi, Phys. Rev. B **65**, 180401(R) (2002).

[205] V. Hardy, M. R. Lees, A. Maignan, S. Hébert, D. Flahaut, C. Martin, and D. M. Paul, J. Phys.: Condens. Matter **15**, 5737 (2003).

[206] S. Abasland, H. Fjellvag, and B. Hauback, Solid State Commun. **101**, 187 (1997).

[207] H. Kageyama, K. Yoshimura, K. Kosuge, M. Azuma, M. Takano, H. Mitamura, and T. Goto, J. Phys. Soc. Jpn. **66**, 3996 (1997).

[208] H. Kageyama, K. Yoshimura, K. Kosuge, H. Mitamura, and T. Goto, J. Phys. Soc. Jpn. **66**, 1607 (1997).

[209] A. Maignan, V. Hardy, S. Hebert, M. Drillon, M. R. Lees, O. Petrenko, D. M. K. Paul, and D. Khomskii, J. Mater. Chem. **14**, 1231 (2004).

[210] H. Wu, M. W. Haverkort, Z. Hu, D. I. Khomskii, and L. H. Tjeng, Phys. Rev. Lett. **95**, 186401 (2005).

[211] X. X. Wang, J. J. Li, Y. G. Shi, Y. Tsujimoto, Y. F. Guo, S. B. Zhang, Y. Matsushita, M. Tanaka, Y. Katsuya, K. Kobayashi, K. Yamaura, and E. Takayama-Muromachi, Phys. Rev. B **83**, 100410 (2011).

[212] V. Hardy, S. Lambert, M. R. Lees, and D. M. Paul, Phys. Rev. B **68**, 014424 (2003).

[213] H. Fjellvag, E. Gulbrandsen, S. Aasland, A. Olsen, and B. C. Hauback, J. Solid State Chem. **124**, 190 (1996).

[214] K. E. Stitzer, J. Darriet, and H.-C. zur Loye, Curr. Opin. Solid State Mater. Sci. **5**, 535 (2001).

[215] A. Maignan, C. Michel, A. C. Masset, C. Martin, and B. Raveau, Eur. Phys. J. B **15**, 657 (2000).

[216] V. Hardy, M. R. Lees, O. A. Petrenko, D. McK. Paul, D. Flahaut, S. Hébert, and A. Maignan, Phys. Rev. B **70**, 064424 (2004).

[217] C. L. Fleck, M. R. Lees, S. Agrestini, G. J. McIntyre, and O. A. Petrenko, Europhys. Lett. **90**, 67006 (2010).

[218] J. G. Cheng, J. S. Zhou, and J. B. Goodenough, Phys. Rev. B **79**, 184414 (2009).

[219] Y. Zhao, S. S. Gong,W. Li, and G. Su, Appl. Phys. Lett. **96**, 162503 (2010).

[220] Y. B. Kudasov, A. S. Korshunov, V. N. Pavlov, and D. A. Maslov, Phys. Rev. B **78**, 132407 (2008)

[221] S. Agrestini, L. C. Chapon, A. Daoud-Aladine, J. Schefer, A. Gukasov, C. Mazzoli, M. R. Lees, and O. A. Petrenko, Phys. Rev. Lett. **101**, 097207 (2008).

[222] X. Y. Yao, S. Dong, H. Yu, and J. M. Liu, Phys. Rev. B **74**, 134421 (2006).

[223] Y. B. Kudasov, Phys. Rev. Lett. **96**, 027212 (2006).

[224] T. Burnus, Z. Hu, M. W. Haverkort, J. C. Cezar, D. Flahaut, V. Hardy, A. Maignan, N. B. Brookes, A. Tanaka, H. H. Hsieh, H. J. Lin, C. T. Chen, and L. H. Tjeng, Phys. Rev. B **74**, 245111 (2006).

[225] V. Hardy, D. Flahaut, M. R. Lees, and O. A. Petrenko, Phys. Rev. B **70**, 214439 (2004).

[226] V. Hardy, C. Martin, G. Martinet, and G. Andr é, Phys. Rev. B **74**, 064413 (2006).

[227] X. Y. Yao, S. Dong, and J. M. Liu, Phys. Rev. B **73**, 212415 (2006).

[228] R. Soto, G. Mart ínez, M. N. Baibich, J. M. Florez, and P. Vargas, Phys. Rev. B **79**, 184422 (2009).

[229] E. V. Sampathkumaran, N. Fujiwara, S. Rayaprol, P. K. Madhu, and Y. Uwatoko, Phys. Rev. B **70**, 014437 (2004).